CRANFIELD UNIVERSITY

School of Aerospace, Transport and Manufacturing
MSc in Computational Fluid Dynamics

Academic Year: 2017–2018

Overset Approach in a CFD study of a Solid and Deformed Isolated Rotating Wheel in Contact with the Ground

Jesús Vilar Cánovas

Supervisor: Dr Antonios Antoniadis
September 2018

This thesis is submitted in partial fulfilment of the requirements for the degree of MSc in CFD.

Abstract

A computational study of an isolated rotating wheel is performed with both steady and unsteady Reynolds Averaged Navier-Stokes solver in STAR-CCM+. Fackrell A2 wheel geometry is reproduced and flow conditions are replicated in order to validate obtained results. Contact modelling and rotating motion is overcome with an innovative Zero Gap overset interface and solution is compared to similar studies with a more conventional approach. Good overall agreement is found with steady RANS, followed by a time dependent simulation that better captures expected flow features. Great drag prediction is obtained while lift is underpredicted compared to experimental data due to successful suction peak prediction after the contact patch and later flow separation on the top of the wheel. Promising unexpected transversal vortex after the contact patch is identified probably due to overset rotating boundary condition. In parallel, tyre deformation under vertical load and inflation pressure is solved for linear elastic and multilayer hyperelastic material in ABAQUS. Eventually, fluid dynamics and structural deformation are merged and CFD simulations are reproduced over obtained deformed geometry. Higher lift is predicted with deformed wheel in addition to wider jetting phenomena coming from the contact patch. Satisfying set up and obtained solutions result in a complete basis for further coupled Fluid-Structure interaction.

Keywords

CFD; FEA; RANS; transient; automotive; wheel; rim; tyre; deformation;contact; rotating; overset; mesh; fluid mechanics; aerodynamics.

Aknowledgements

In first place, I would like to say thank you to my supervisor, who has always encouraged me during these months of hard work and given me a great support to overcome all the difficulties found on the way. At the same time, I am pleased to Cranfield University and Polythecnic University of Valencia for offering me the opportunity of being enrolled in this Double Degree Erasmus program.

This year in Cranfield University and finally the thesis project has been a success thanks to all the people I have met here. Flat mates, course colleagues, handball team and the rest of friends have been essential to enjoy this experience. A big 'thank you' goes for Albert, who has always given me a critical opinion and useful tips that have helped me to develop a better quality work.

Last but not least, my family and friends from home that encouraged me to come to Cranfield and have given me the strength to reach my aims.

Contents

List of Figures

List of Tables

List of Symbols and Abbreviations

ε	Turbulent dissipation rate, elastic strain
μ	Dynamic viscosity
ω	Angular velocity
ρ	Density
θ	Wheel rotation coordinate
ν	Kinematic viscosity, Poisson's ratio
$_\infty$	Freestream
$\boldsymbol{\sigma}$	Stress tensor
$\boldsymbol{f}_b$	Body forces
$\boldsymbol{r}$	Position vecotr
$\boldsymbol{v}$	Velocity vector
$\boldsymbol{D}$	Rate of deformation tensor
$\boldsymbol{L}$	Lamb vector
$\boldsymbol{S}$	Mean Strain rate tensor
$\boldsymbol{T}$	Viscous stress tensor

k	Turbulent kinetic energy
n	Turbulent charge
p	pressure
u, v, w	Velocity in x, y and z
y^+	Dimensionless wall distance
CD	Drag Coefficient
CL	Lift Coefficient
Cp	Pressure coefficient
D	Wheel diameter
E	Young Modulus
G	Shear modulus
$\bar{I}$	Strain invariant
J	Total volume change
U	Strain energy
CFD	Computational Fluid Dynamics
CFL	Courant-Friedrichs-Levy
CMM	Coordinate Measuring Machine
COPEN	Contact Opening
CPRESS	Contact Pressure

DES	Dettached Eddy Simulation
DNS	Direct NAvier Stokes
FEA	Finite Element Analysis
FSI	Fluid Structure Interaction
LDA	Laser Doppler Anemometry
LES	Large Eddy Simulation
RANS	Reynolds-Averaged Navier-Stokes
RNG	Re-Normalization Group
SAE	Society of Automotive Engineers
SATM	School of Aerospace, Technology and Manufacturing
SEA	School of Energy, Environment and Agrifoods
URANS	Unsteady Reynolds-Averaged Navier-Stokes

Chapter 1

Introduction

Wheels design is a demanding and challenging problem in industry nowadays. Many different fields are involved and pushed to the edge in order to obtain a successful overall product. Although this thesis project is focused on Computational Fluid Dynamics (CFD), other engineering fields such as material design and structural behaviour are also treated through Finite Element Analysis (FEA) tool. A brief overview of wheel mechanical properties is presented along with the flow physics and vortex structures expected in a rotating wheel in contact with the ground. Furthermore, a literature review regarding experimental data and similar models applied within FEA and CFD is shown. Finally, thesis scope and main objectives are exposed based on today's motivation in automotive and motorsport sector.

1.1 Wheel physics

1.1.1 Aerodynamics

Special attention is brought to wheels aerodynamic behaviour in automotive sector since it is demonstrated that it is responsible for one third of the total drag of a standard vehicle [6]. Apart from the drag generated by the wheel itself, it is highly important the interaction of the vortex structures generated with the rest of the vehicle [7]. Hence, drag force is an essential parameter to be studied when designing a car due to its direct influence in car efficiency and fuel consumption [8]. Moreover, lift force plays an important role in race cars, where higher aerodynamic forces are expected. For instance, experiencing an extra downforce when turning at high speed may have a great effect in flow behaviour and performance.

Contribution to overall drag is strongly dependent on geometry and driving conditions. In Formula 1 and open-wheel cars in general, wheels are bluff bodies completely exposed to

freestream flow. Thus, it becomes an even greater source of drag that needs to be avoided with a careful design of the rest of the car configuration [9]. Several studies have been carried out regarding to wheel covering [7, 10]. Drag produced by rear wheels is significantly decreased when they are covered, although it is increased when front wheels are covered as well [7]. Therefore, drag generation is reduced when covering an isolated wheel but it can lead to undesired performance when the whole car is considered due to the interaction between the components.

Flow features

Understanding fluid flow behaviour around a rotating wheel is crucial to validate the results obtained from simulations and identify expected flow features. Main vortices generated after an isolated rotating wheel are already known thanks to previous experimental and numerical research found in literature, as seen in figure 1.1. A highly turbulent wake is generated downstream the wheel with strong trailing vortices that lead to high aerodynamic drag in the rear zone. The horseshoe vortex appreciated in the schematic representation is the dominating structure, being extended downstream further than any other structure.

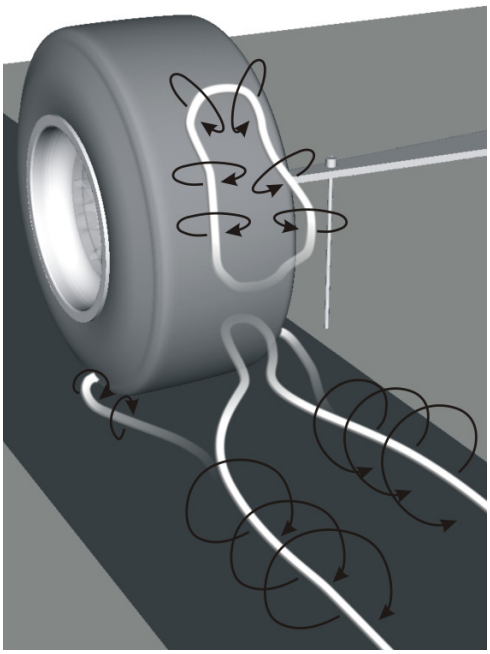

Figure 1.1: Representation of flow vortices in the near wake behind an isolated rotating wheel [1].

Separation point at the top of the wheel is a critical aspect to be predicted. A ring vortex is generated in the dettached region due to early separation [1]. It was found by Fackrell [2] that separation takes place around 10^{o} upstream the top part of the wheel, although some discrepancies are found in literature where separation point is usually predicted closer to the top part both in numerical and experimental studies [11, 12]. Fackrell also discovered that the flow was

not separated directly from the surface of the rotating wheel but from a thin boundary layer following the rotating motion induced by the wheel (see figure 1.2). Therefore, separation takes place above the tyre surface at the point where fluid tangential velocity is zero.

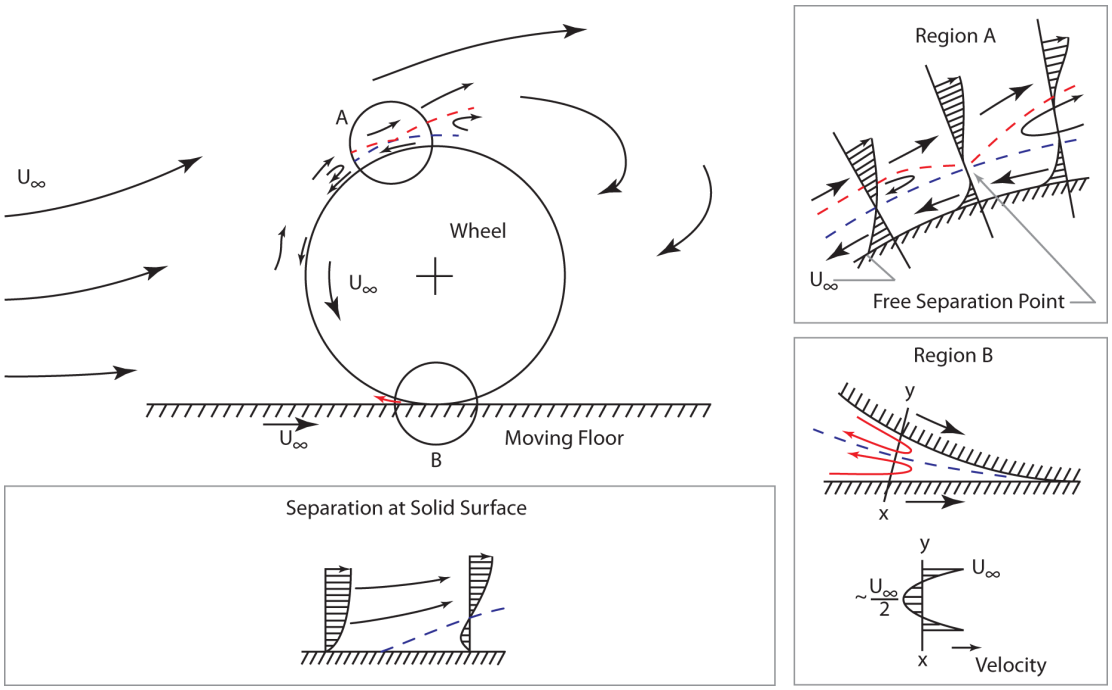

Figure 1.2: Flow behaviour near the separation point and contact patch described by [2]. Free separation point in A is located above a thin layer induced by wheel rotation. Flow near contact patch in B is pushed outwards the wheel and the ground. Figure modified by Sprot [3].

Finally, the front contact part between the ground and the wheel is the source of a squash vortex that is developed towards the back of the wheel. Squash vortices are joint to the horshoe vortex downstream, enlarging the vortices strength. These vortices generated in the contact path are known as jetting phenomena [2].

Experimental study conducted by Saddington et al. [13] in an open-jet wind tunnel with a Reynolds number based on wheel diameter of $6.8 \cdot 10^5$ identifies the main structures in the near wake of an isolated Formula 1 wheel rotating in ground contact (see figure 1.3):

- Inverted-T low velocity region.
- Large region of reversed flow and a pair of strong counter-rotating vortices extended over the ground.
- Counter-rotating vortex pair on the upper half of the near wake that merge with the ground vortices before one wheel diameter downstream.
- Vortices are aligned at least until one wheel diameter downstream.

Some important differences are found regarding to aerodynamic behaviour when considering a stationary wheel instead of a rotating wheel [11]. The separation point is found downstream

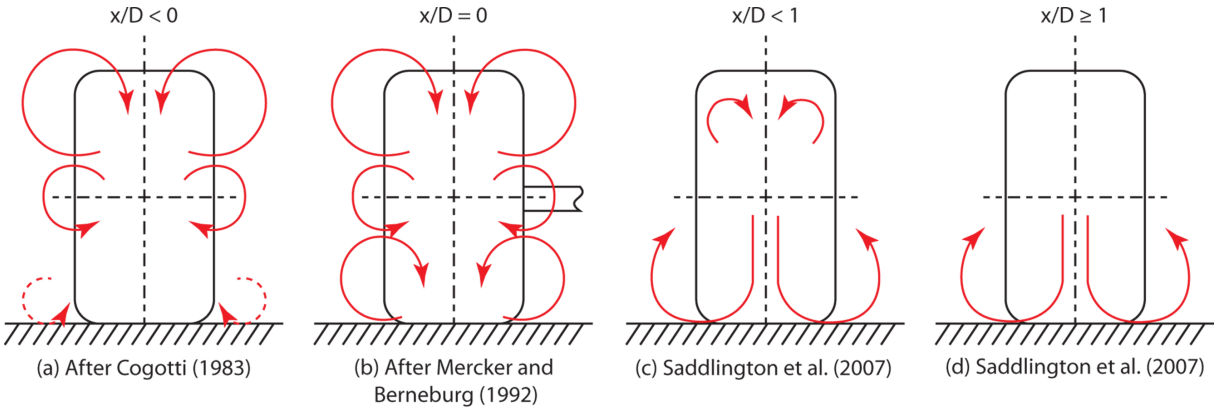

Figure 1.3: Suggested flow structure in the wake of an isolated wheel by Saddington et al. [13]. The counter-rotating vortex pairs are found right after the wheel that are vanished and merged to the main vortex pair above the ground.

the top part of the wheel, at the rear part, thus the arch shaped vortex is not formed. The flow coming from the top of the wheel and the main flow coming from the sides of the wheel are met in an interaction region in the upper near wake. Thus, the resulting flow is energised and follows the rear part of the wheel attached to the surface with a higher speed. In agreement with experimental data [2], vortices in the near wake are stronger for the stationary case compared to a transient rotating wheel case in the same region.

Geometry effect

It is a common strategy to assume, both in experimental and numerical studies, simplifications in the geometry and set up of the case in order to reduce the complexity of the model and the computational cost [14]. However, the effect of simplifications and different variables on obtained results can play an important role and should be quantified [9].

In terms of experimental set up, it has been tested in previous work that the only configuration possible to accurately represent the flow patterns around a real wheel is having a rotating wheel on a moving ground [9]. Unfortunately, it implies a great time and economic effort for car manufacturers. Hence, improving the accuracy of simulations with numerical methods would eventually provide reliable results at a lower cost.

The influence of freestream velocity on the drag generated in an isolated wheel is analysed by Leśniewicz et al. [15]. It is demonstrated that drag coefficient is decreased when airspeed is increased. The same trend is observed with both slick and grooved tyres, but it is found a slightly lower drag coefficient for grooved tyres. Including threads in the tyre surface is significant for obtaining more realistic results. When grooves are considered, a greater roughness is emulated on the surface of the tyre due to rotating motion. Boundary layer thickness over the tyre is

affected by this effect, provoking further uncertainties in obtained results [16]. A valid simplification would involve defining a given roughness into the boundary condition as proposed by Schnepf et al. [17]. A surface roughness of 0.5 mm on the tyre surface was imposed, leading to a better prediction of separation point location at the top of the wheel compared to the experimental results.

Most studies use a symmetrical configuration, disregarding the different angles of the wheel or the deformation experienced in real conditions. These considerations have an influence on the wake pattern experienced downstream the wheel, with a direct inpact in the drag estimation [8].

Sprot [18] concluded after a wide research the impact of different variables when modelling a wheel. From the most relevant to the most negligible issue, the studied variables are arranged as follows: axle height, yaw angle, camber angle, internal details, tyre inflation pressure, flow rate through the hub and finally the rotating internal brake rotor.

Taking into account tyre deformation for aerodynamic studies brings many additional complications, thus it has only been overcome for Formula 1 investigations [3]. Effects such as sidewall bulge and contact patch shape can be included to analyse a more realistic scenario. While contact patch is defined as a singular line for rigid wheels, a more progressive contact patch can be model with and elliptical shape as seen in real tyres. The jetting phenomena can be clearly affected depending on how the contact patch is modelled.

Wäschle et al. [19] performed pressure and velocity measurements around an isolated and deformable tread wheel in a rotating and steady configuration to validate two CFD simulations. A realistic contact patch was able to be modelled, although sidewall deformation was not correctly defined. Axerio et al. [20] performed a study of a 60% scale stationary Formula 1 tyre. RANS and LES simulations with stationary walls are compared to experimental data. Near wake is demonstrated to be dominated by two large counter-rotating vortices, while the inboard vortex is larger than the outboard one due to the camber angle and deformation experienced. A periodic oscillation of the vortex center is observed, although it is not ensured whether it is because of interrogation methods or deformation of the tyre.

Wickern [21] stated that a realistic tyre contact patch is not crucial and differences in drag between a tyre with full or reduced load is negligible for a single rotating wheel within a wheel housing [22]. However it has been demonstrated by later studies [23, 24] that the size of the wake (directly related to drag generation) is increased with the contact patch width. This effect is even more prominent downstream.

1.1.2 Mechanical properties

Forces and moments

The most characteristic mechanical features in wheel tyres under standard conditions are outlined in Yang's thesis [5]. It is important to understand the behaviour of operating wheels to reproduce a realistic model. Main forces and moments experienced in wheel dynamics are found in figure 1.4, enclosed in the well-known coordinate system given by the Society of Automotive Engineers (SAE) and widely applied in vehicle dynamics [25]. Forces along the three axis correspond to tyre longitudinal force (F_x), lateral force (F_y) and vertical force (F_z) respectively; while moments are defined as overturning (M_x), rolling resistance (M_y) and aligning moment (M_z). Two different angles are defined from the 'wheel plane' in figure 1.4. The slip angle α is defined by velocity vector and x-z plane while camber angle γ is defined by vertical vector and x-z plane.

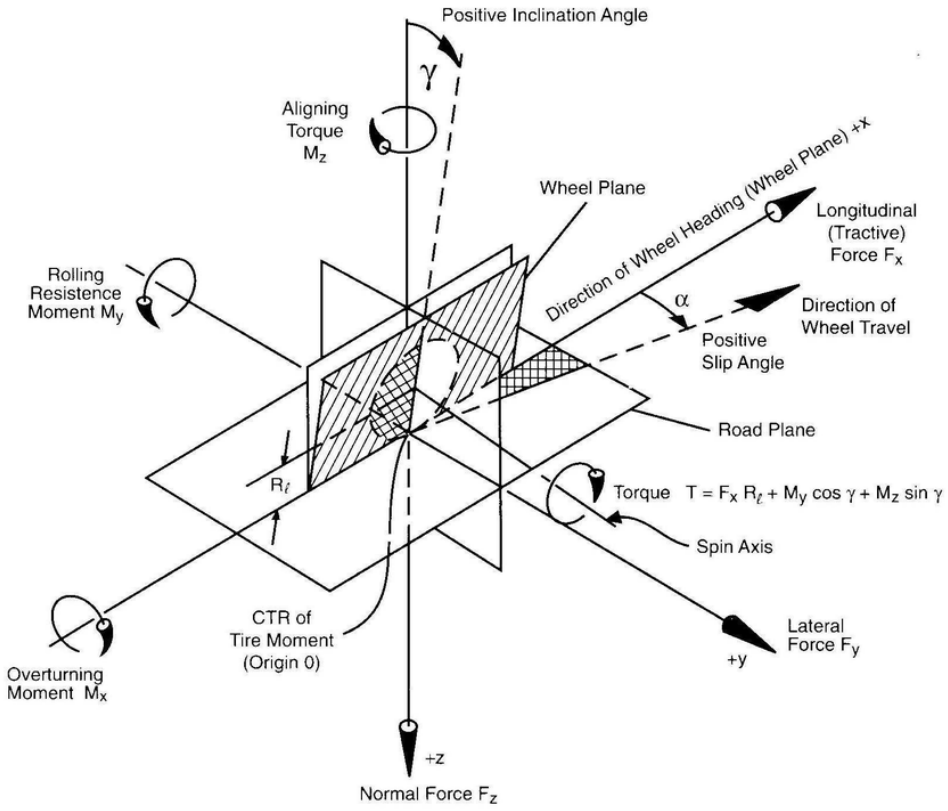

Figure 1.4: Nomenclature and system of reference of wheel dynamics regarding SAE [26]. Forces, moments and angles are defined in the three axis.

Tyre forces are provoked by normal and shear stresses distributed along the contact patch with the ground. Longitudinal and lateral forces are generated by shear stress due to the friction coupling effect between tyre tread and road. This friction coupling effect is itself caused by two primary mechanisms: surface adhesion and hysteresis [27].

Loads

Main loads experienced by a tyre are grouped within inflation pressure, external and thermal loads [25]. These loads in addition to the contact with the ground provoke wheel deformation. Wheel resistance to be deformed under given loads is known as stiffness, being classified as follows:

- Vertical stiffness. It is defined as the vertical force-deflection ratio and it is related to the vertical vibration and ride behaviour. It is mainly affected by tyre topology, preload, inflation pressure and rim width.

- Longitudinal stiffness. It is defined as the longitudinal force-deflection ratio and it is relevant for longitudinal cushioning of road irregularities that lead to tyre shimmy. For rotational case, the longitudinal stiffness is the force due to rim rotation angle.

- Lateral stiffness. It is defined as the lateral force-deflection ratio and it is linked to tyre oscillation in lateral and yaw directions.

As it can be seen in figure 1.5, a greater stiffness is normally found in the longitudinal direction, followed by vertical and lateral direction ($K_x > K_z > K_y$).

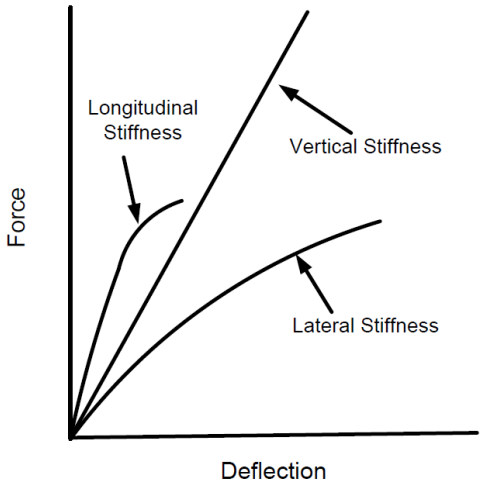

Figure 1.5: Force-deflection representation of longitudinal, vertical and lateral stiffness of a wheel tyre [28].

1.2 Literature review

1.2.1 Computational Fluid Dynamics (CFD)

Experimental Data

It must be outlined the importance of the work carried out by Fackrell [2], who performed experimental measurements on both stationary and rotating wheels in the 70's. It established a solid base of experimental reference data that has been extensively used afterwards. Most of the numerical simulations found in literature about rotating wheels are referred to Fackrell's work, being a trustworthy source for CFD validation. Besides, it was the first work completed with a moving ground and without any gap between the ground and the wheel.

Fackrell tested six different wheels combining three diffrent rim widths and two tyre profiles. For present study, wheel geometry A2 is simulated as it is the most referred one in similar CFD studies and presents the most complete set of reference data.

The experiment was performed in a wind tunnel with a moving ground and a Reynolds number of $5.3 \cdot 10^5$, which corresponds to a freestream velocity of 18.6 m/s. Pressure probes were located at different points on the surface of the tyre so the perimeter distribution of the pressure coefficient could be analysed. As rapid fluctuations were provoked by turbulent effects, powerful equipment was needed to achieve enough resolution to identify these phenomena.

Based on the results obtained by Fackrell [2], lift and drag are increased with wider wheels. Nevertheless, when using wider wheels the contribution from the rim decreases and the drag generated by the tyre becomes more dominant.

For all cases, the separation point was found to be between $\theta = 280^\circ - 290^\circ$, what corresponds to $10^\circ - 20^\circ$ upstream the top of the wheel. Early separation provokes lift decreasing since a smaller low pressure region is developed over the wheel.

Both stationary and rotating wheels were measured and it was concluded, in agreement to other studies, that aerodynamic coefficients are reduced with wheel rotation. Grooved tyres were also tested in order to assess their aerodynamic effect. In this case, an increase in the drag coefficient could be seen, whereas the lift coefficient kept fized around a similar value.

Rotating wheel models

One of the main challenges that comes up with rotating wheel problem is modelling the rotation of the wheel in contact with the ground. There are several ways to implement it in a numerical calculation using CFD.

- Rotating Boundary Condition. It is the simplest approach that can be applied both in steady and unsteady simulations, based on a specified tangential velocity applied on the surface of the wheel. The reference frame and motion specification can be defined as it is in fact a moving wall condition. Although it can provide accurate results for axisymmetric bodies, this method is unable to be implemented in non-symmetric domains with more detailed geometries [29].
- Moving Reference Frame. This method can be considered as an upgrade with respect to the previous one. Axisymmetry is no longer a limitation but steady simulations and turbulence cannot be fully capture as it has an inherently unsteady nature. Therefore, this method can be useful to obtain good approximations in non-axisymmetric bodies but should not be used if accurate results are required [29].
- Sliding Mesh Approach. This method allows the interaction between two regions with a moving interface between them performing time-dependent calculations. The regions are meshed independently, but they are both bounded by at least one interface, which is the common face between the regions. Therefore the relative motion between the regions happens in this interface. The cells located next to the interface in each region slide on each other in discrete steps [29].
- Overset Mesh Approach. Also known as *Chimera* grid, this method supports overlapping grids while the data is interpolated at the interface. There exists a background mesh covering the whole domain, while the overlapping mesh is created around the body of interest with the required motion defined. An advantage of this method is that independent grids can be made for different bodies providing more flexibility to the grid generation step, as remeshing is simplified as well. Nevertheless, some requirements are needed for the mesh to be valid, such as having at least 4 or 5 overlapping elements between the regions, and defining similar cell sizings in the overlaps both of the background and overset grids [29].

Contact patch models

Despite rotatin wheel boundary conditions, the most challenging aspect in wheel modelling is the contact between the wheel and the moving ground. Ideally, this contact would be represented by two tangent surfaces [9], however it would lead to extremely fine mesh near the contact with bad quality elements [30]. Several solutions can be found in literature to overcome this problem.

The main goal for improving the accuracy around the contact patch is coorectly modelling the jetting phenomena [2]. Axon et al. [6] define a wall velocity on the contact patch so that the discontinuities between the tangential velocity of the tyre and the moving ground are minimised.

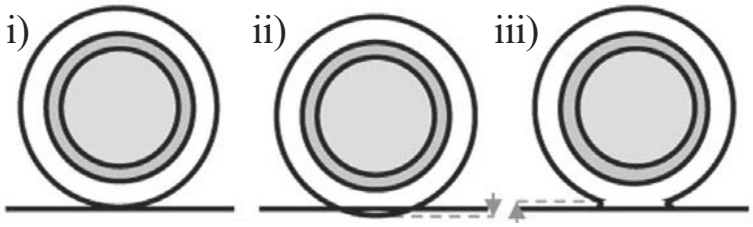

Figure 1.6: Step generation for contact patch modelling described by Diasinos [9]. The wheel is introduced into the ground and then extruded until desired height.

A more sophisticated approach is the use of a step as a transition between the wheel and the ground [9]. A better meshing strategy can be followed and better quality elements are achieved near the contact [31]. The height of the step needs to be analysed as the flow structures developed after the wheel are directly affected by this variable. When a higher step is considered, the size of the wake is narrower and higher as the separation point is moving backwards. A lower drag coefficient is obtained due to the lower dettachment [9].

Another tested approach consists on trimming the wheel to simulate the contact with the ground as a flat face of the wheel [8]. The front and rear jetting phenomenon is correctly predicted although the strength of the front one is underrated if compared to experimental data. It is an approach easy to be applied with reasonably good results, but the main drawback is that it is unable to be rotated, so it could not be applied with an overset approach.

Turbulence models

A wide range of turbulence models implemented in wheel modelling simulations is found in literature depending on the aims of the study and the previous literature considered.

A complex and unsteady turbulent wake is experienced due to the interaction with counter rotating vortex found in experimental measurements [32]. RANS approach is not suitable for such detached flows as different scales must be resolved or modelled for this case. However, it is the most employed approach among studies found in literature.

Diasinos and Barber [9] justify the use of steady RANS based on its extensive application range in the automotive industry. The effect of simplifications in the geometry are quantified both with steady and unsteady RANS simulations to analyse its impact on the flow field. While geometry simplifications are related to remarkable variations in aerodynamic coefficients, the difference between steady and unsteady simulations is low in terms of general flow field. The most relevant difference is found in the separation point with a 2^o variation.

Most of previous studies agree on applying different versions of $\kappa-\varepsilon$ turbulence model. *RNG* $\kappa-$

ε is used by Mears and Axon et al. [8, 6]. It is expected to perform better than *Standard* $\kappa-\varepsilon$ when the streamlines are very curved and there is important flow separation. Conversely, it is stated that two equation models generally fail to correctly predict complex separation bubbles and reattachments. Other sources propose $Spalart-Allmaras$ as the most accurate one at locating the separation point in the wheel [18].

Some studies can also be found where $\kappa-\varepsilon$ is combined with another turbulence model, forming a two-layer boundary method. One equation model is used by Wäschle [1] in the region close to the wall, while $\kappa-\varepsilon$ model is used in the far field. In [19] a comparison is carried out between *RNG* $\kappa-\varepsilon$ model with wall functions, and a two-layer model combining a Norris & Reynolds one-equation model in the near wall regions, while $\kappa-\varepsilon$ equations are applied at the far field with a boundary layer resolution of $y^+ = 3$. Both approaches provide similar results and averaged velocity error (6-8%) in different cross planes of the wheel with respect to LDA measurements. Nevertheless, the two-layer approach gives the same error both for stationary and rotating wheels, so it is concluded to be preferred for the rotating wheel case, since it better represents the flow structures behind the wheel. In terms of aerodynamic coefficients, the two-layer provides more accurate results for the drag coefficient, but it is the *RNG* $\kappa-\varepsilon$ model the one that better approaches the lift coefficient calculated experimentally.

Regarding the mesh in the boundary layer, most of the sources in literature use the enhanced wall treatment and a boundary resolution $y^+ = 1$ so that the flow in the inner boundary layer is meshed with good resolution [9].

There exist few literature about LES and DNS for rotating wheel flows due to their high computational cost. However, these methods have the advantage of providing time dependent results and it is shown to provide more accurate results in the separated regions [33, 34]. There are also few cases in literature using Lattice-Boltzmann Method [16, 17], in some cases with different grid approaches [35].

1.2.2 Finite Element Analysis (FEA)

Experimental Data

Model validation is a very important and necessary step before the FE model is applied for prediction of tyre static and dynamic behaviour. Any uncertainty or poor prediction in the model have a significant influence in obtained results. Tyre wheels are a multi-input and multi-output system. Any variation in the value of tyre material properties or structural parameters will affect the tyre response such as force or resonant frequency.

Yang [5] validated both 2D and 3D tyre models with experimental data. An axisymmetric cross-section 2D model was used to simulate tyre geometry change under different inflation

pressures. The average displacement of tyre tread and sidewall region was correlated using a trial-axial coordinate measuring apparatus known as Coordinate Measuring Machine (CMM). The 3D tyre model was used for the validation of tyre vertical static stiffness, footprint area and sidewall strain. Although some factors such as the operational error lead to some inaccuracies, the level of correlation between the experiment and FEA was considered satisfactory.

Geometry

Although many papers have been published in the past decades on the investigation of tyre FEA using 3D tyre model, the geometry information of tyre cross-section is usually hard to be obtained. Structural details of tyres is confidential for most manufacturers and detailed information is not available.

Nevertheless, several methods have been developed for acquiring tyre geometry information. Bolarinwa [36] used CMM and created a 3D model based on obtained profile revolving the cross-section in Abaqus. Uncertainties can be an important drawback for this manual procedure, being unable to measure the tyre bead region.

Danielson et al [37] unfolded a simple and effective semi-automated procedure for distinguishing tyre geometric characteristics for tyre modelling. Based on the study of Danielson, Yang [5] introduces an alternative method for FE tyre modelling by extracting accurate tyre cross-section data from a Formula Student tyre using image processing technology.

Materials

Tyres are manufactured based on a complex multi-layer design with different composite materials and fibre orientation. It supposes a great challenge to replicate the exact layout and characteristics of every single part. Normally, it is made up of high modulus cords of twisting threads of cotton, nylon, polyester and steel wire within low modulus rubber. Then, several layers of oriented cords distributed along the rubber act as a reinforcement as seen in figure 1.7. The number of reinforcement layers is specially dependent on each tyre type, size and tyre inflation pressure (i.e. aircraft tyres present more layers than passenger car tyres).

The dominant component at every tyre is rubber, caracterised by a highly nonlinear stress-strain behaviour. Tyre reinforcement includes belts, carcass, bead, cap ply, and bead reinforcement. The rubber material properties for different components, such as tread and sidewall, vary and present different mixed proportions of rubber and carbon black [38]. The function of tread rubber is to keep the balance of tyre performance and durability, while the sidewall rubber is designed mainly for fatigue resistance. To meet the challenge, extensive researches have been carried out on the investigation of rubber and reinforcement material properties [39, 40].

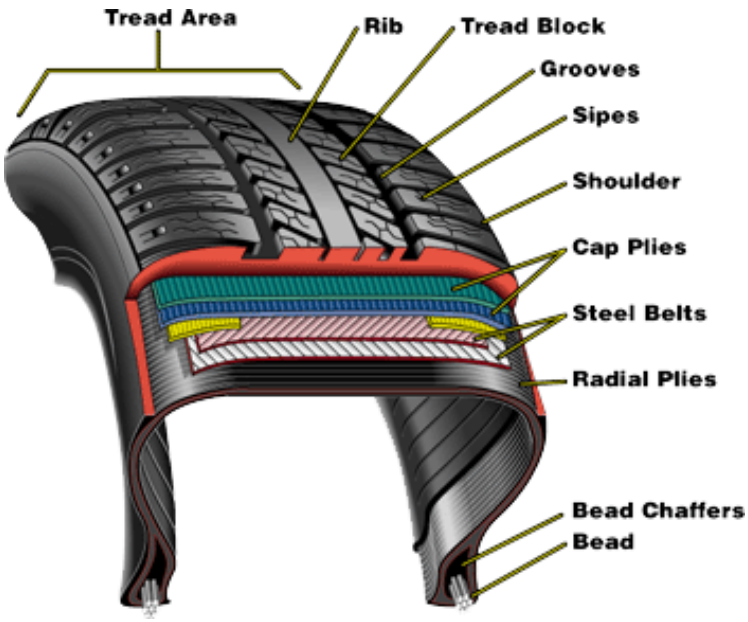

Figure 1.7: Section of a realist wheel tyre model showing the multi-layer material composition.

In the University of Birmingham, Andrew Burke [41] presented good prediction of tyre dynamic overall response using FE tyre model developed in MSC.Nastran. The 2D tyre profile was split into several zones with different composite properties obtained experimentally. It included two Young modulus and one major Poisson's ratio, while the minor Poisson's ratio and the shear modulus were calculated analitically. It is effective and accurate for macroscopic investigation of tyre behaviour, although the increased number of divided sections for accurate material property representation is time-consuming. Using a different approach, E. O. Bolarinwa [36] investigated the rubber hyperelasticity properties and considered the cord as a linear elastic material for FE tyre model in ABAQUS. Tyre material properties approach supposed a deep insight into the response of individual tyre reinforcement layers during tyre service, achieving an accurate prediction of tyre cornering behaviour. However, only one rubber material type is considered and local behaviour could not be properly analysed in a microscopic approach. Then, Yang [5] obtained the material properties of different components of the tyre in order to reproduce tyre behaviour accurately from a local point of view, especially strain and stress.

1.3 Aims and Objectives

Previous year work performed by Nianioura [42] and specially Olmedo [24] was focused on rotating and sliding boundary conditions. Overset approach was unable to be implemented in STAR-CCM+ due to the complexity of modelling the contact patch and was proposed as future work. It is found in literature that the contact patch is still far from being properly modelled and there exist no relevant studies where overset approach is implemented. A successful contact modelling with overset mesh would mean a great advantage for this field as the wheel could actually be rotating and no unrealistic gadgets would be needed to model the wheel-ground interaction. Moreover, it could be applied to other fields where contact interactions and moving bodies are studied.

Furthermore, aerodynamic study over deformable wheels is of great interest especially for motorsport sector and is currently being developed. Wheel deformation offers a more realistic wheel-ground interaction (flat surface intersection instead of a line) and the possibility of analysing critical racing conditions where aerodynamics drastically change. Some experimental studies have been carried despite durability and cost limitations. Few CFD studies are found and they are all static cases where a predefined deformed wheel is imported and rotating/sliding boundary conditions are applied. A gap in literature is found regarding to fluid-structure interaction (FSI), where dynamic wheel deformation could be studied.

Based on this scenario, the objectives of the thesis are:

- Set up a robust overset approach with a realistic contact patch model in STAR-CCM+ and study the aerodynamics of the isolated rotating wheel. Run steady RANS and URANS simulations and validate the results with experimental data and similar studies found in literature.
- Design a wheel rim tyre structural model and obtain the deformation due to external loads and inflation pressure. Solid stress module in STAR-CCM+ is aimed to be employed as a preliminary step and ideally Abaqus as a last step.
- Run a CFD simulation over the deformed wheel and analyse the differences with the solid wheel.
- Explore the capabilities of STAR-CCM+ to carry a FSI simulation with Abaqus.

Chapter 2

Theoretical framework

All relevant governing equations related to the numerical simulations performed in this study are introduced bellow. All vectors are defined as bold lowercase letters, while tensors are identified as bold uppercase letters.

2.1 Governing equations

2.1.1 Fluid flow

As rotating motion is being considered, it is important to highlight the difference between absolute and relative velocity and different coordinate systems. Considered a rotating reference frame around an imaginary axis with constant angular velocity ω and translating at a linear velocity $\boldsymbol{v}_t$ relative to a fixed reference frame (known in STAR-CCM+ as laboratory). Relative velocity $\boldsymbol{v}_r$ is defined in equation 2.1 from the velocity in the laboratory reference frame $\boldsymbol{v}$ and the velocity relative to the moving reference frame $\boldsymbol{v}_g$.

$$\boldsymbol{v}_r = \boldsymbol{v} - \boldsymbol{v}_g = \boldsymbol{v} - (\boldsymbol{v}_t + \boldsymbol{\omega} \times \boldsymbol{r}), \tag{2.1}$$

where the position vector from the origin of the moving reference frame to any point in the computational domain is defined as $\boldsymbol{r}$. If moving reference frame is just rotating, as it is the current case, translational velocity would be zero.

Continuity and momentum equations are the governing equations for the fluid flow, being the energy equation neglected as no temperature change is taken into account in this case. Continuity equation 2.2 is based on the *Principle of Mass Conservation* in the control volume defined in the system [43].

$$\frac{\partial \rho}{\partial t} + \nabla \cdot (\rho \boldsymbol{v}) = 0 \tag{2.2}$$

where density is ρ, time is t and $\boldsymbol{v}$ is the velocity vector in the continuum. After expanding the multiplication in the divergence term, continuity turns into a scalar function in equation 2.3. First term represents temporal density variation, second one is the scalar product of velocity vector and density gradient and the last one is the velocity divergence.

$$\frac{\partial \rho}{\partial t} + \boldsymbol{v} \cdot \nabla \rho + \rho \, (\nabla \cdot \boldsymbol{v}) = 0 \tag{2.3}$$

Air can be often considered as an incompressible fluid at low velocities, generally with Mach numbers lower than 0.2-0.3. It is estimated a density variation lower than 5-10% regarding to NASA demonstration [44], so incompressibility is a valid hypothesis if that small change is not considered relevant. Compressible effects are not expected in this case where Mach number is around 0.05, although local density changes might be experienced in the contact patch region as stated by Keogh et al. [45].

Density is considered as a constant value, leading to continuity equation for incompressible fluids 2.4.

$$\nabla \cdot \boldsymbol{v} = \frac{\partial u}{\partial x} + \frac{\partial v}{\partial y} + \frac{\partial w}{\partial z} = 0 \tag{2.4}$$

Several steps are needed to reach a simplified differential equation for the conservation of linear momentum (equation 2.5) from *Newton's II Law* and *Momentum Conservation* as described in [43].

$$\frac{\partial \rho \boldsymbol{v}}{\partial t} + \nabla \cdot (\rho \boldsymbol{v} \otimes \boldsymbol{v}) = \nabla \cdot \boldsymbol{\sigma} + \boldsymbol{f}_b, \tag{2.5}$$

where $\otimes$ is the Kronecker product, $\boldsymbol{\sigma}$ is the stress tensor and $\boldsymbol{f}_b$ term represent body forces acting on the continuum. Stress tensor can be split by normal and shear stress contribution in a fluid continuum as equation 2.6, defined by pressure p and viscous stress tensor $\boldsymbol{T}$ respectively.

$$\boldsymbol{\sigma} = -p\boldsymbol{I} + \boldsymbol{T}, \tag{2.6}$$

where $\boldsymbol{I}$ is the identity tensor. For Newtonian fluids, the viscous stress tensor is given by:

$$\boldsymbol{T} = 2\mu \boldsymbol{D} - \frac{2}{3} (\nabla \cdot \boldsymbol{v}) \boldsymbol{I}, \tag{2.7}$$

where μ is the constant dynamic viscosity of the fluid and $\boldsymbol{D}$ is the rate of deformation tensor known as strain. The second term in equation 2.13 is neglected for incompressible flows as seen in equation 2.4. Strain tensor is defined in equation 2.8.

$$\boldsymbol{D} = \frac{1}{2}\left(\nabla \boldsymbol{v} + (\nabla \boldsymbol{v})^T\right). \tag{2.8}$$

Momentum equation for Newtonian incompressible flows 2.12 is then formed by a transient and convective term on the left side and pressure, diffusive and external force term on the right side.

$$\frac{\partial \rho \boldsymbol{v}}{\partial t} + \nabla \cdot (\rho \boldsymbol{v} \otimes \boldsymbol{v}) = -\nabla \cdot p\boldsymbol{I} + \mu \nabla \cdot \left(\nabla \boldsymbol{v} + (\nabla \boldsymbol{v})^T\right) + \boldsymbol{f}_b, \tag{2.9}$$

RANS

Most flows are characterised in reality by random fluctuations with a wide range of length scales and frequencies, known as turbulence. Dimensionless Reynolds number (Re) quantifies the importance of convective and viscous terms. This concept was introduced by Stokes [46] in 1851. Turbulent flows, where convective terms are dominant upon viscous terms, present high Reynolds numbers while laminar flows are related to low Reynolds numbers. The limit between both definitions is not clearly defined, although it is widely assumed that an external flow around an obstacle is turbulent when $Re_d \geq 20{,}000$ [47]. However, it is dependent on many factors such as free-stream, surface or disturbance conditions.

With DNS (Direct Navier Stokes) method, the exact governing equations of turbulent flows are resolved, involving a huge computational cost unaffordable for any industrial applications. Thus, turbulence models are essential for engineering applications. Reynolds-Averaged Navier-Stokes (RANS) is a basic and popular approach widely used in industry due to its low computational cost and acceptable accuracy. RANS is based on variable decomposition into mean and fluctuating components:

$$\phi = \bar{\phi} + \phi', \tag{2.10}$$

where ϕ represents state variables such as pressure and velocity. Since fluctuating term is negligible compared to mean term, Reynolds-averaged continuity and momentum equations can be defined from 2.4 and 2.12 as:

$$\nabla \cdot (\bar{\boldsymbol{v}} - \boldsymbol{v}_g) = 0 \tag{2.11}$$

$$\frac{\partial \rho \bar{\boldsymbol{v}}}{\partial t} + \nabla \cdot [\rho \bar{\boldsymbol{v}} (\bar{\boldsymbol{v}} - \boldsymbol{v}_g)] = -\nabla \cdot \bar{p} \boldsymbol{I} + \nabla \cdot (\boldsymbol{T} + \boldsymbol{T}_t) + \boldsymbol{f}_b, \tag{2.12}$$

where the added term introduced by the averaging procedure $\boldsymbol{T}_t$ is known as Reynolds stress tensor defined in equation 2.13.

$$\boldsymbol{T}_t = -\rho \begin{pmatrix} \overline{u'u'} & \overline{u'v'} & \overline{u'w'} \\ \overline{u'v'} & \overline{v'v'} & \overline{v'w'} \\ \overline{u'w'} & \overline{v'w'} & \overline{w'w'} \end{pmatrix}. \tag{2.13}$$

Reynolds stress needs to be modelled to close the system of governing equations. One of the most popular methods along with Reynolds-Stress Models is known as Eddy Viscosity Models, where momentum transfer due to turbulent eddies is modeled with a turbulent viscosity μ_t. It is based on Boussinesq hypothesis [48], which states that the Reynolds stress tensor $\boldsymbol{T}_t$ is proportional to the mean strain rate tensor $\boldsymbol{S}$ as seen in 2.14.

$$\boldsymbol{T_t} = 2\mu_t \boldsymbol{S} - \frac{2}{3} (\mu_t \nabla \cdot \bar{\boldsymbol{v}}) \boldsymbol{I}. \tag{2.14}$$

Realizable $\kappa - \varepsilon$

Depending on the strategy to calculate the turbulent viscosity, several turbulence models are found. Turbulent viscosity is solved based on turbulent kinetic energy k and turbulent dissipation rate ε for well-known k-ε turbulence model, originally developed by Jones and Launder [49]. Realizable k-ε Two-Layer model in STAR-CCM+ [50] is used for simulations in current study. Turbulent viscosity μ_t is defined as:

$$\mu_t = \rho C_\mu f_\mu k T = \rho C_\mu f_\mu \frac{k^2}{\varepsilon}, \tag{2.15}$$

where C_μ is a model coefficient, f_μ is a damping equation and T is the turbulent time scale. For realizable models, T is defined as the large-eddy time scale as k/ε.

The transport equations for the turbulent kinetic energy k and turbulent dissipation rate ε are defined as follows

$$\frac{\partial (\rho k)}{\partial t} + \nabla \cdot (\rho k \bar{\boldsymbol{v}}) = \nabla \cdot \left[\left(\mu + \frac{\mu_t}{\sigma_k} \right) \nabla k \right] + P_k - \rho (\varepsilon - \varepsilon_0) + S_k, \tag{2.16}$$

$$\frac{\partial(\rho\varepsilon)}{\partial t}+\nabla\cdot(\rho\varepsilon\bar{\boldsymbol{v}})=\nabla\cdot\left[\left(\mu+\frac{\mu_t}{\sigma_\varepsilon}\right)\nabla\varepsilon\right]+\frac{1}{T_e}C_{\varepsilon1}P_\varepsilon-C_{\varepsilon2}f_2\rho\left(\frac{\varepsilon}{T_e}-\frac{\varepsilon_0}{T_0}\right)+S_\varepsilon. \tag{2.17}$$

where σ and C parameters are model coefficients, P are production terms, f a damping function and S user-defined source terms. The ambient turbulence value ε_0 in the source term counteracts the turbulence decay [51]. As an ambient source term can be defined, a specific time-scale T_0 can be implemented as:

$$T_0=max\left(\frac{k_0}{\varepsilon_0},C_t\sqrt{\frac{\nu}{\varepsilon_0}}\right) \tag{2.18}$$

A two-layer approach available in STAR-CCM+ is applied as it offers the added value of an all y^+ wall treatment. While k is solved, ε is prescribed algebraically in the near-wall region as

$$\varepsilon=\frac{k^{3/2}}{l_\varepsilon}, \tag{2.19}$$

where l_ε is a length scale function dependent on the three different model variants specified in STAR-CCM+. The two-layer formulation and the full two-equation model are linked by the wall-proximity indicator 2.20 suggested by Jongen [52]

$$\lambda=\frac{1}{2}\left[1+tanh\left(\frac{Re_d-Re_y^*}{A}\right)\right], \tag{2.20}$$

where Re_y^* is a model coefficient that limits the applicability of the two-layer formulation and A is the width of the wall-proximity indicator defined to enclose λ within 1% of its far-field value. Turbulent viscosity can then be blended with the two-layer value as

$$\mu_t=\lambda\mu_t|_{k-\varepsilon}+(1-\lambda)\,\mu\left(\frac{\mu_t}{\mu}\right)_{2layer}, \tag{2.21}$$

where the two-layer viscosity ratio is also defined depending on the model variant. More detailed information about the default coefficients and functions from mentioned model can be found in STAR-CCM+ theory guide [29].

Realizable k-ε is recommended against Standard k-ε for many applications. Besides a new transport equation for ε, C_μ is not constant and is defined in function of mean flow and turbulence properties. The spreading rate of planar and round jets is predicted more accurately as it offers a higher performance for rotating flows, boundary layers facing adverse pressure gradients, separation and recirculation bubbles [47].

2.1.2 Solid mechanics

Several elastic models are available in ABAQUS to perform FEA simulations, from linear elasticity to viscoelastic, foam or fabric materials. Linear elasticity is valid for small elastic strains (less that 5%) and it is obvious that there are more appropriate models to simulate rubber deformation.

Linear elastic model

The total stress $\boldsymbol{\sigma}$ for linear elastic material model is defined from the total elastic strain $\boldsymbol{\varepsilon}^{el}$ as

$$\boldsymbol{\sigma} = \boldsymbol{D}^{el}\boldsymbol{\varepsilon}^{el}, \tag{2.22}$$

where $\boldsymbol{D}^{el}$ is the fourth-order elasticity tensor. The number of independent components in the elasticity tensor is dependent on the number of symmetry planes through every point for the elastic properties. Isotropic (infinite symmetry planes), orthotropic (two orthogonal symmetry planes) and anisotropic (no symmetry planes) materials can be found. For isotropic materials, stress-strain constitutive equation is defined as

$$\begin{Bmatrix} \varepsilon_{11} \\ \varepsilon_{22} \\ \varepsilon_{33} \\ \gamma_{12} \\ \gamma_{13} \\ \gamma_{23} \end{Bmatrix} = \begin{bmatrix} 1/E & -\nu/E & -\nu/E & 0 & 0 & 0 \\ -\nu/E & 1/E & -\nu/E & 0 & 0 & 0 \\ -\nu/E & -\nu/E & 1/E & 0 & 0 & 0 \\ 0 & 0 & 0 & 1/G & 0 & 0 \\ 0 & 0 & 0 & 0 & 1/G & 0 \\ 0 & 0 & 0 & 0 & 0 & 1/G \end{bmatrix} \begin{Bmatrix} \sigma_{11} \\ \sigma_{22} \\ \sigma_{33} \\ \sigma_{12} \\ \sigma_{13} \\ \sigma_{23} \end{Bmatrix}. \tag{2.23}$$

The elasticity tensor is defined by Young's modulus E, Poisson's ratio ν and shear modulus G, that is defined at the same time by E and ν as

$$G = \frac{E}{2(1+\nu)}. \tag{2.24}$$

Drucker stability conditions must be satisfied, which states that the deformation of a body with time-independent properties under isothermal conditions is stable if the work done in the case of infinitesimal increments in the generalised forces dQ_i for correspondinf infinitesimal increments in the generalised displacements dq_i is positive [53].

$$\sum dQ_i \, dq_i > 0. \tag{2.25}$$

That means that the elastic tensor should be positive defined, directly limiting the elastic material constants. For isotropic case, the elastic constants are bounded based on the stability criteria as follows.

$$\begin{cases} E > 0 \\ G > 0 \\ -1 < \nu < 0.5 \end{cases} \tag{2.26}$$

Nearly an incompressible behaviour is experienced when Poisson's ratio is close to 0.5. Hybrid elements are usually required in that case in ABAQUS/Standard module.

Hyperelastic model

Rubber hyperelastic material property is related to highly non-linear and incompressible material behaviour. There exist two different methods for characterising rubber hyperelastic properties: statistical thermodynamics and phenomenological approach. For tyre rubber modelling, phenomenological approach is normally used based on continuum mechanics and strain energy approach is derived from it [40]. It is defined that the strain energy per unit volume stored in a material is a function of the general components of strain at any point [5].

Material models within FEA present different possibilities to characterise strain energy functions. Normally, functions are defined in terms of strain invariants, which are themselves functions of the stretch ratios. In ABAQUS [4], strain energy U is defined for isotropic compressible materials in function of first and second strain invariant $(\overline{I_1}, \overline{I_2})$ and total volume change at a material point $\boldsymbol{x}$ (J).

$$U = U\left(\overline{I_1}, \overline{I_2}, J\right). \tag{2.27}$$

To define the variables of strain energy it is necessary to go back to the deformation gradient $\boldsymbol{F}$ definition

$$\boldsymbol{F} = \frac{\partial \boldsymbol{x}}{\partial \boldsymbol{X}}, \tag{2.28}$$

where $\partial \boldsymbol{X}$ is the reference position of the material point $\partial \boldsymbol{x}$. Total volume change J can then be defined as the determinant of deformation gradient

$$J = det\left(\boldsymbol{F}\right). \tag{2.29}$$

First and second strain invariants expression is by definition

$$\overline{I_1} = \overline{F}_1^2 + \overline{F}_2^2 + \overline{F}_3^2, \tag{2.30}$$

$$\overline{I_2} = \overline{F}_1^{(-2)} + \overline{F}_2^{(-2)} + \overline{F}_3^{(-2)}, \tag{2.31}$$

where $\overline{F_i}$ is defined for algebraic simplicity as the deformation gradient with the volume change eliminated

$$\overline{\boldsymbol{F}} = J^{-\frac{1}{3}}\boldsymbol{F}. \tag{2.32}$$

Within the several models available for strain energy definition, Mooney-Rivlin formulation is probably the most popular one for tyre rubber material, based on strain energy potential [54, 55]. In contrast, it was found by Ghosh et al. [40] that Mooney-Rivlin formulation is unable to predict large strain behaviour of rubber material. Some limitations are also considered with Neo-Hookean [56] and Ogden [57] models, related to coefficient determination for multi-axial deformation modes.

After mentioned limitations, Yeoh model [58] is suggested by Yang [5] upon tests shown in figure 2.1 and following reasons:

1. Wider deformation range can be covered.
2. Stress-strain behaviour can be predicted in different deformation modes from data gained in one simple deformation mode like uni-axial tension.
3. Varying shear modulus with increasing deformation can be predicted.

Strain energy function is defined by Yeoh model in equation 2.33 based on the first deviatoric strain invariant and total volume change

$$U = C_{10}\left(\overline{I_1} - 3\right) + C_{20}\left(\overline{I_1} - 3\right)^2 + C_{30}\left(\overline{I_1} - 3\right)^3 + \frac{\left(J^{el} - 1\right)^2}{D_1} + \frac{\left(J^{el} - 1\right)^4}{D_2} + \frac{\left(J^{el} - 1\right)^6}{D_3}, \tag{2.33}$$

where C_{i0} and D_i for $i = 1, 2, 3$ are temperature-dependent material parameters defined in following chapter (see table 3.6).

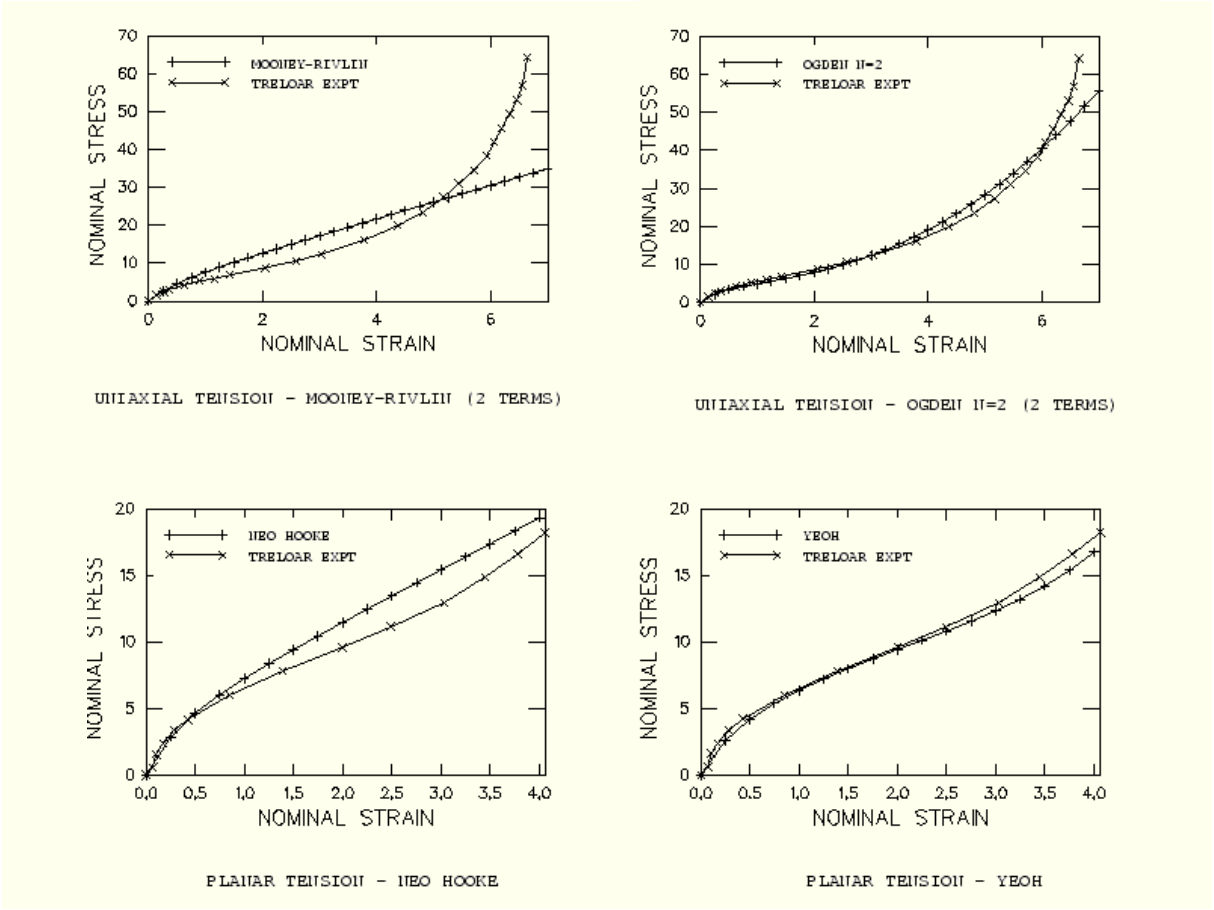

Figure 2.1: Uniaxial tension correlation test for strain energy models in ABAQUS compared to Treloar's experimental data [4].

Finite-sliding interaction formulation

Two main different formulations are available in ABAQUS/Standard when modelling contact interaction between a deformable (slave) and rigid (master) body:

- **Small-sliding**. Slave-master link is established preliminary and it is automatically determined which segment on the master surface will interact with each node/surface on the slave surface. That relationship is maintained during the whole simulation. Surfaces in contact can only undergo relatively small sliding between each other.
- **Finite-sliding**. Slave-master link is tracked continuously, leading to complex calculations if both bodies are deformable. However, it is much simpler for a deformable-rigid body interaction. It is applied when separation and sliding of a given amplitude are expected.

The second approach is suggested for the kind of interaction expected in this study. First, contact elements are automatically generated based on associated surfaces and then overclosure and shear sliding is quantified at every integration point. Overclosure is defined as the penetration of the deforming body into the rigid one. After that, these kinematic measurements plus Lagrange

multiplier techniques are used to apply surface interaction theories available.

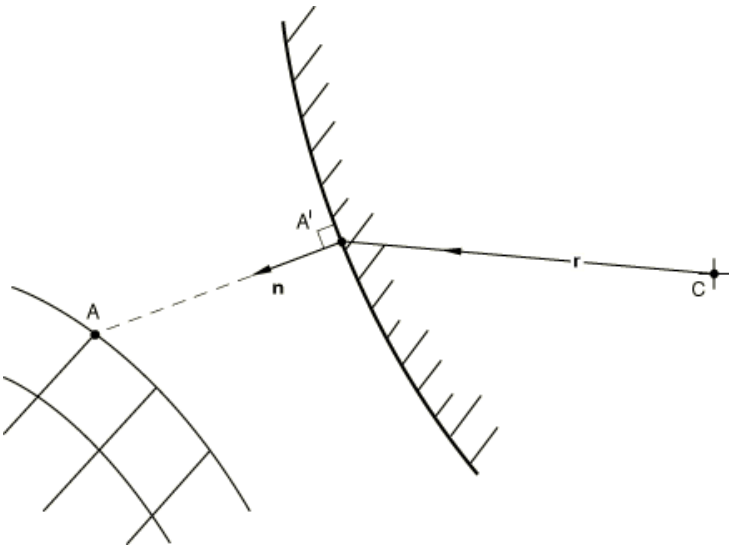

Figure 2.2: Surface contact modelling representation [4]. Reference points and vectors employed in contact formulation are shown.

Let A be a point on the deforming mesh with $\boldsymbol{x}_A$ coordinates while A' is the closest point to it on the rigid body surface with $\boldsymbol{x}_{A'}$ coordinates. The position of the rigid body is defined by it reference node C with coordinates $\boldsymbol{x}_C$. The normal vector linking surface points A and A' is defined as $\boldsymbol{n}$ and $\boldsymbol{r}$ is the vector from C to A' within the rigid body as seen in figure 2.2. Surface contact can be formulated as

$$\boldsymbol{n}h = -\boldsymbol{x}_A + \boldsymbol{x}_C + \boldsymbol{r}, \tag{2.34}$$

where h is the distance from A to A' along $\boldsymbol{n}$. Let define c as the clearance distance below which contact takes place. Then, surfaces are considered or not in contact regarding to eqn. 2.35.

$$\begin{cases} h < -c & \longrightarrow \quad no\ contact, \\ h \geq -c & \longrightarrow \quad contact. \end{cases} \tag{2.35}$$

Clearance value depends on surface definition. If hard surface is defined no clearance is taken into account, thus the value is set to wero. In contrast, soft surface allows non-zero clearance values. When the contact condition is satisfied, the interaction needs to be enforced.

Distance coordinates along the tangents $\boldsymbol{t}_\alpha$ through point A' at rigid surface is defined as $\boldsymbol{S}^\alpha$, where $\alpha = 1,2$ are locally orthogonal directions. Projected point coordinates on rigid surface $\boldsymbol{x}_{A'}$ is translated as point in deformable surface A and rigid body are moved. Its variation is then defined as

$$\delta \boldsymbol{x}_{A'} = \delta \boldsymbol{x}_C + \delta \boldsymbol{r}|_{\gamma_\alpha} + \delta \boldsymbol{r}|_{\phi_C} = \delta \boldsymbol{x}_C + \delta \boldsymbol{\phi}_C \times \boldsymbol{r} + \boldsymbol{t}_\alpha \delta \gamma_\alpha, \tag{2.36}$$

where first term is rigid body translation, second term is rigid body rotation and the third point A' translation. After described motion, normal vector will also vary as described in eqn. 2.37.

$$\delta \boldsymbol{n} = \delta \boldsymbol{n}|_{\gamma_\alpha} + \delta \boldsymbol{n}|_{\phi_C} = \delta \boldsymbol{\phi}_C \times \boldsymbol{n} + \frac{\delta \boldsymbol{n}}{\delta S_\alpha} \delta \gamma_\alpha. \tag{2.37}$$

From eqn. 2.34 and including expressions obtained in eqn. 2.36 and 2.37, the linearised form of the contact equation is

$$\boldsymbol{n}\delta h + h\left(\delta \boldsymbol{\phi}_C \times \boldsymbol{n} + \frac{\delta \boldsymbol{n}}{\delta S_\alpha} \delta \gamma_\alpha\right) = -\delta \boldsymbol{x}_A \delta \boldsymbol{x}_C + \delta \boldsymbol{\phi}_C \times \boldsymbol{r} + \boldsymbol{t}_\alpha \delta \gamma_\alpha. \tag{2.38}$$

As clearance value is zero for hard contact and a very small value also for soft contact, assumption $h = 0$ is made and eqn. 2.38 is simplified in 2.39.

$$\boldsymbol{n}\delta h = -\delta \boldsymbol{x}_A + \delta \boldsymbol{x}_C + \delta \boldsymbol{\phi}_C \times \boldsymbol{r} + \boldsymbol{t}_\alpha \delta \gamma_\alpha. \tag{2.39}$$

Then, linearised equation can be split into normal (contact equation) and tangential (slip equation) components

$$\begin{cases} \delta h = -\boldsymbol{n} \cdot (\delta \boldsymbol{x}_A - \delta \boldsymbol{x}_C) + (\boldsymbol{r} \times \boldsymbol{n}) \cdot \delta \boldsymbol{\phi}_C, \\ \delta \gamma_\alpha = \boldsymbol{t}_\alpha \cdot (\delta \boldsymbol{x}_A - \delta \boldsymbol{x}_C) - (\boldsymbol{r} \times \boldsymbol{t}_\alpha) \cdot \delta \boldsymbol{\phi}_C. \end{cases} \tag{2.40}$$

Following the same procedure, second derivative of contact equation can be obtained as found in ABAQUS Theory Guide [4].

2.2 Overset approach

A higher degree of complexity is faced when simulating moving bodies in CFD. Many improvements and different approaches have been developed over the years to accurately reproduce it. Among other possibilities such as Moving Reference Frame or sliding meshes, the overset approach is considered the most powerful one. Also known as Chimera or overlapping mesh, it was developed by the aerospace industry and later implemented in several CFD solvers. A great effort has been made to enable this tool in complex geometries with different physics solvers. If

successfully implemented, it can improve modelling accuracy with realistic motions and handle small gaps and contacts.

Overset meshes generally enclose a given subregion of interest and are superimposed on a background mesh containing the whole computational domain. Even multiple overset meshes can be set on the same background domain. Then, motion can be defined on the overset domain and the mesh will be reattached to the background grid continuously. This approach is mainly applied to single or multiple moving bodies, parametric studies and optimization analyses due to its facility to change and modify geometries and regions within the domain.

The workflow followed in STAR-CCM+ as suggested in its documentation [59] is summarised in 5 simple steps:

1. Individual regions are defined. One background region containing all the computational domain and as overlapping regions as desired around the bodies of interest.
2. The regions are meshed separately and independently.
3. The interface between the overset and background meshes is defined. The grids are trimmed and linked at the interface.
4. If the overset domain is moving, the overlapping zone at the interface is updated.
5. Data is interpolated and communicated between the regions at the interface.

When the overset interface is defined (step 3) and every time it is updated (step 4), both regions are automatically coupled by a hole-cutting process. Then, the cells in each domain are divided into active, overlapping and inactive cells. Within the overlapping cells, donor and acceptor cells can be differentiated. The governing equations are solved in the active cells and interpolation is carried between the donor and acceptor cells in the overlapping region, while the inactive cells are treated as a hole in the domain. When superposing background and overset domains, the whole domain is defined.

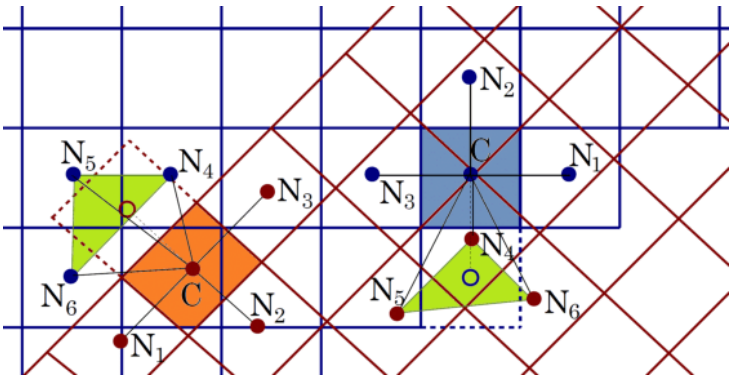

Figure 2.3: Representation of the overset interface interpolation in STAR-CCM+ [59]. Data transfer between overset mesh (red) and background mesh (blue). Acceptor cells (dotted line) provide information for the calculation of active cell center values (orange and blue) [59].

Data transfer representation is shown in figure 2.3 between overset (red) and background mesh (blue). For every active cell (C), information is provided by acceptor cells in the surroundings (dotted line). Likewise, the weight of the acceptor cell is defined by a number of donor cells from the other mesh. Different interpolation schemes are available in STAR-CCM+: distance-weighted defined by default, linearm linear quasi-2D and least-square.

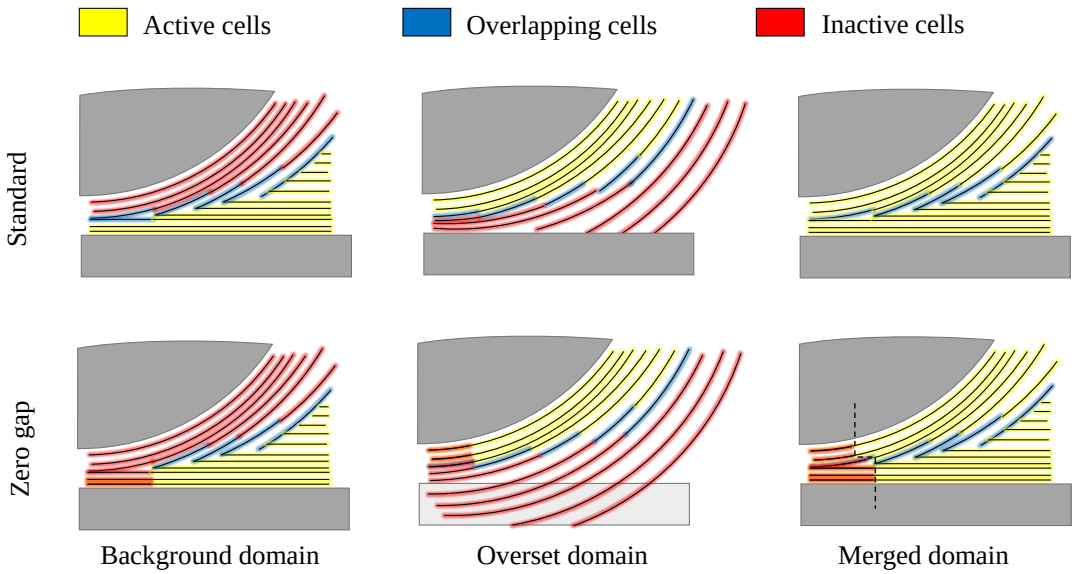

Figure 2.4: Representation of overset zero gap interface and hole cutting procedure. Inactive cells (red) in background and overset domain are removed and active cells (yellow) are merged through overlapping cells (blue). Number of zero gap layers control how far from the contact the hole cutting procedure is carried.

Within the usual features and possibilities from the overset approach, one of the most powerful tools of the overset mesh in STAR-CCM+ compared to other commercial softwares is the ability to handle small gaps and contacts between bodies. Apart from the traditional morphing approach, where bad quality elements with high skewness are generated, small gaps can be physically resolved if a minimum of 2 to 4 cells are found in the gap, depending on the interpolation method. It can be reduced to 2 cells thanks to the Close Proximity option, affecting to local accuracy and stability.

However, if the aim is to model a real contact, no cells will be found between the bodies in the intersection. For that purpose, a very useful and innovative feature is available in STAR-CCM+ known as Zero Gap, key aspect of current study. This alternative overset interface option is based on automatic enclosing of small gaps depending on a given number of zero gap layers. When a minimum number of cell layers is detected between walls, cells within the gap are deactivated and surrounded by a temporary wall, being updated every time step. In addition, it is possible to define an overset domain through a background wall, giving more freedom to

define the region and mesh.

A simplified representation emulating the standard and zero gap overset behaviour between a wheel and the ground is shown in figure 2.4, where yellow lines represent active cell layers, the red ones are inactive cell layers and overlapping cells are represented by th blue lines. In the upper row it can be seen the standard overset interface in the background and overset domain. As a result, in the last column it can be appreciated how the active cells from both domain are adapted to each other and linked by the overlapping cells. However, an undesired gap is solved between the wheel and the ground.

With the zero gap approach in the second row, it can be appreciated how the gap is closed. With the number of zero gap layers, the number of remaining cell layers allowed in the gap before the become inactive is set, controlling the width of zero gap filled with inactive cells. If the number of zero gap layers was set to 3 in both domains, when the number of cells between both bodies goes from 3 to 2 the gap will be surrounded by a temporary wall.

It can be appreciated that it is a really critical modelling point. A very fine grid is desired near the gap in order to reduce the width of the gap as much as possible, although this refinement needs to be done all around the tyre as it will be moving and an unaffordable number of cells is easily reached. A uniform cell distribution is needed as well so that cell layers can be identified and a regular hole cutting process is experienced around the gap. In addition, a smooth transition must be found between overset and background grids, being more difficult to refine at specific zones such as the contact patch and the wake. If these issues are not successfully overcome, the simulation will be unstable and diverge specially with the overset movement.

Chapter 3

Methodology

Procedures followed to create and set up the simulations carried in present thesis project are explained in detail in this chapter, going from CAD design of studied geometry, main features and strategies of mesh generation process, computational set up and data analysis. The chapter is clearly divided into the two main approaches carried: CFD and FEA.

3.1 CFD

3.1.1 Geometry

An isolated rotating F1 wheel in contact with a moving ground is simulated based on Fackrell's work [2]. Six different wheels are studied in mentioned experiment, corresponding to three different wheel widths (A,B,C) combined with two different tyre edge profiles (1,2). Wheel geometry combination A2 is the one studied in this thesis as a continuation of Olmedo [24] and Athanasia [42] previous work. Besides, it is the most widely studied geometry in literature since it presents the most complete set of experimental data.

There is no detailed data about geometry specifications either in Fackrell's work nor the rest of the literature. From overall geometry known lengths such as wheel diameter and width, section representations have been digitised in order to obtain a reliable design. Half section has been reproduced in CATIA V5 software and later revolved to generate the whole wheel, as seen in figure 3.1. Pressure probes along the tyre have been used to define the edge shape and obtain pressure data afterwards.

Computational domain is designed afterwards to discretise the fluid domain, essential for a CFD simulation. A wind tunnel topology is followed as it is desired to achieve the most similar conditions to experimental ones. Several computational domain dimensions are found in literature,

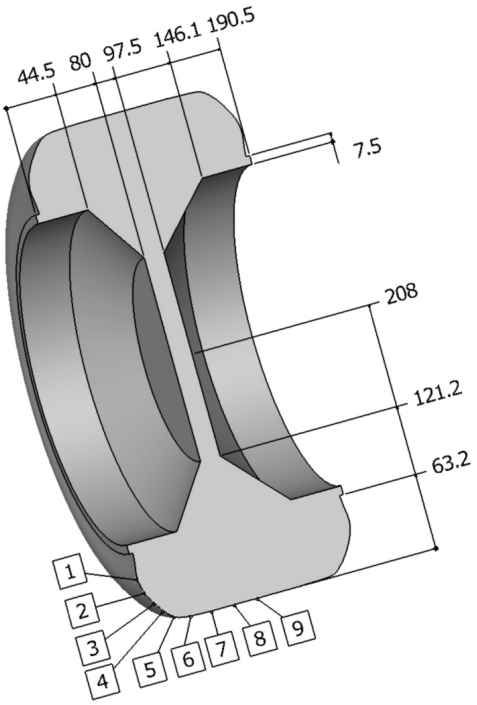

Figure 3.1: Scaled Fackrell's A2 wheel geometry model with dimensions in mm. The labels identify the pressure probes from experimental data that are used for defining tyre prfile.

although the one proposed by McManus [11] is taken. Distance from the wheel to the outer domain is reasonably big not to experience any perturbation and keep a moderate size not to have unnecessary extra elements.

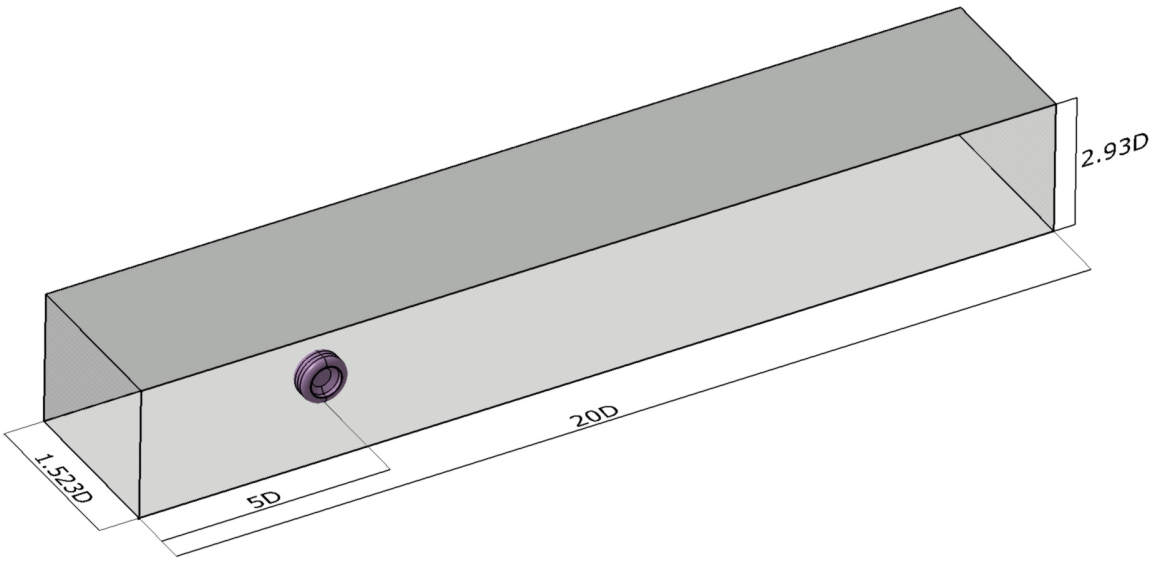

Figure 3.2: Computational domain for CFD simulations based on McManus paper [11]. Measurements as a function of wheel diameter (D=416 mm).

3.1.2 Mesh

Mesh generation is one of the most challenging task when modelling a rotating wheel in contact with the ground. Meshing sharp edges is always a source of bad quality elements in CFD simulations. In addition, contact modelling is very limited in CFD solvers and some strategies need to be followed to obtain a close approach. If a small gap is led between the ground and the wheel, a flow channel is created and the flow is accelerated in an unrealistic way. A common strategy followed in previous studies is based on a smooth step employed as a link between the ground and the wheel. Good quality mesh can be achieved, although an unrealistic obstacle is faced by the flow in that zone and vortex structures captured at the bottom of the wheel are not reliable.

All the difficulties experienced are multiplied when modelling a transient simulation with a rotating body and overset approach. Many of these strategies including smooth transitions to the ground are not fit for a moving body, since that added part would need to rotate with the body. Similar problems are face with the refinement strategy. Special refinement is desired in the zone near the contact patch to obtain a better mesh quality and resolution. However, as the mesh is turning, that refinement box would be translate around the wheel. Then, the strategy should be totally different to tackle all that difficulties with a mesh grid that is uniform all along the wheel surface and not reaching unaffordable number of cells.

Apart from specific problems to be solved within current case, overset meshes bring additional requirements. As suggested in STAR-CCM+ User Guide [29], it is very important to respect a similar cell size at the interface between the background and overlapping grid and that the interface is far enough from the body surface to avoid strong gradients.

First, a background mesh is generated including the whole domain with polyhedral elements. The wheel is merely in contact with the ground, with no step or gap. The main objective when generating the background mesh is to obtain a refine region around the the wheel in a uniform way and along the wake. It can be appreciated in figure 3.3 how the mesh is really fine around the wheel, with a moderate refinement upstream and downstream the wheel and a sharp cell growth to the outer boundaries looking for high dissipation. Intermediate refinement is achieved by means of a refinement box, highlighted in figure 3.3, and two consecutive wake refinements for a smoother transition. Wake refinement option available in STAR-CCM+ is enabled from the tyre surface, indicating the direction, length and spread angle of the wake and the target element size with a given growth ratio.

Mesh refinement around the wheel is controlled by a cylindrical control volume corresponding to the overset interface trying to force the same cell size in that region and more importantly at the interface. Inside that volume, a second control volume is defined around the wheel with a tube shape, coming from two different diameter cylinders subtract operation. This way, the

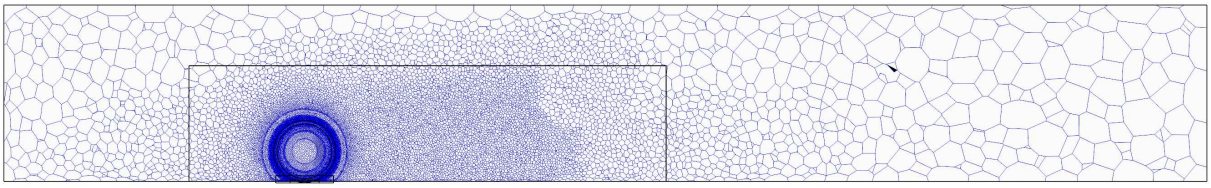

(a) Lateral view of the whole domain.

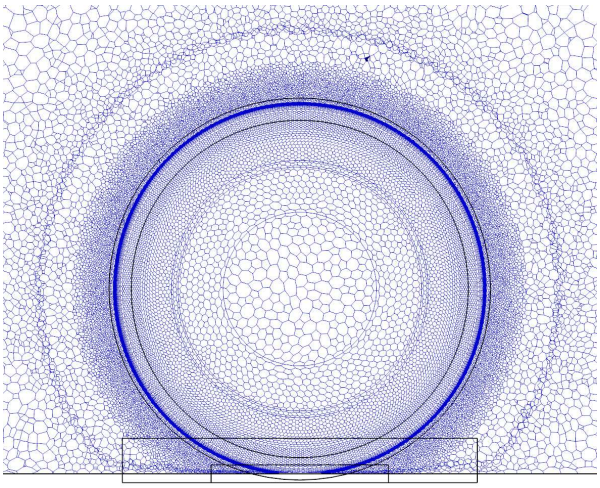

(b) Lateral view focused on the wheel.

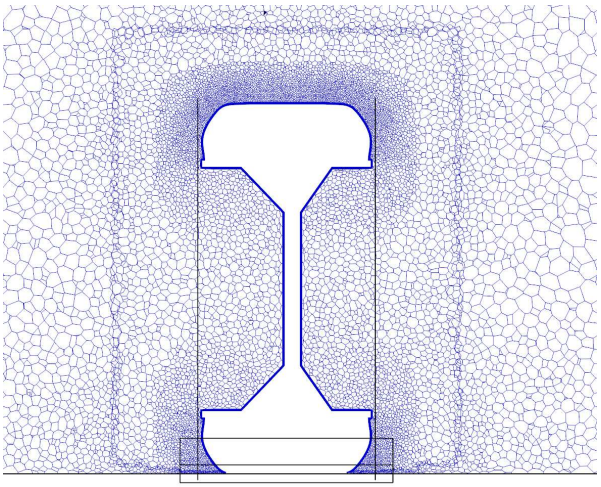

(c) Front view focused on the wheel.

Figure 3.3: Coarse mesh grid representation for CFD simulations. Three different views are shown at central plane section with refinement volumes outlines in black.

finest mesh is found around the tyre in the desired area, avoiding too small elements near the whole wheel. Finally, a refinement box is placed at the base of the wheel that, in addition to surface curvature and close proximity refinement options, helps to maintain a uniform cell size close to the contact zone.

The overset domain, including the wheel, is enclosed by a cylinder with the same axis as the wheel. Overset Zero Gap approach is applied as specified in previous section. Because of that, the overset boundary condition can penetrate the wall boundary condition from the background mesh. Then, the overset domain will rotate and the interface between both domain will be updated every time step, modelling the wheel rotation with high fidelity. Polyhedral elements provide high quality mesh and the possibility of arrange an unstructured mesh with a higher control than a tetrahedral mesh, which present a better adaptation due to its sharper edges.

Overset cell status in both background and overset domain can be appreciated in figure 3.4. As explained in previous section, the red cells represent the inactive cells where the governing equations are not solved. Yellow cells represent the active cells while the blue ones are the overlapping cells, acting as an interface with the other domain and interpolating data from

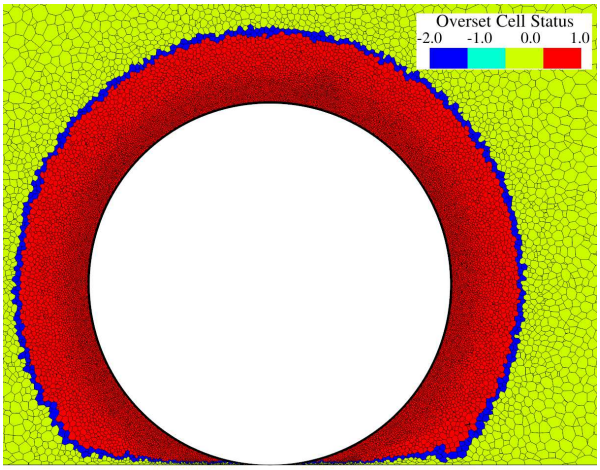

(a) Cutting plane xy at z=0 in background domain.

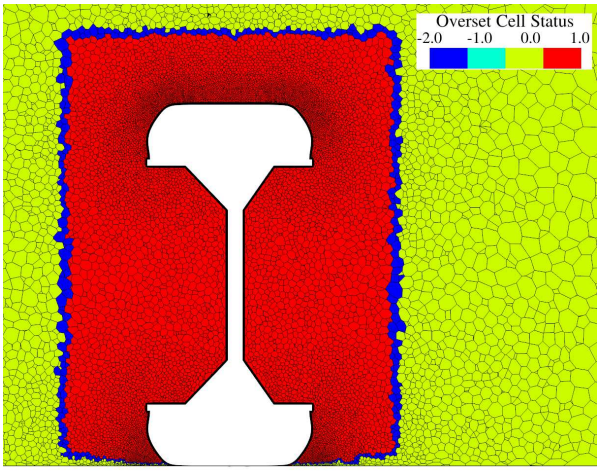

(b) Cutting plane yz at x=0 in background domain.

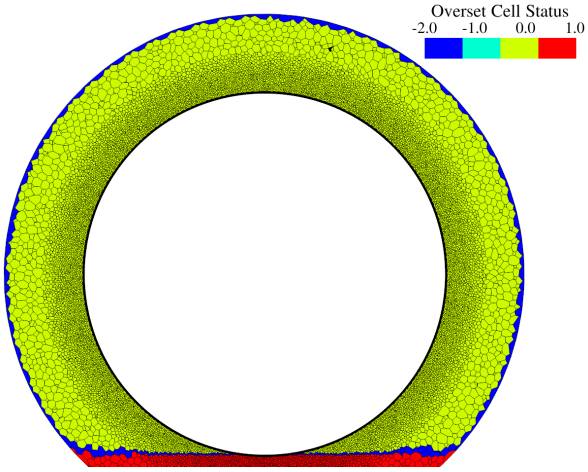

(c) Cutting plane xy at z=0 in overset domain.

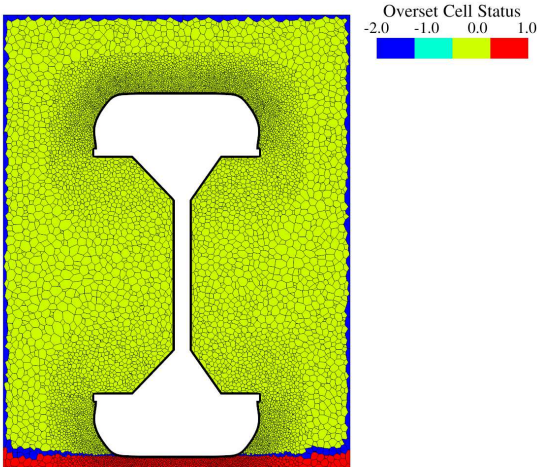

(d) Cutting plane yz at x=0 in overset domain.

Figure 3.4: Overset cell status representation at the interface around the wheel at xy and yz centrals planes in background and overset domain. Inactive cells are highlighted in red (1), active cells in yellow (0) and overlapping in blue (-2).

donor and acceptor cells. Inactive cells are vanished by a hole-cutting algorithm every time step and both active domain are overlapped through the interface. It can be appreciated that both mesh grids present a similar size at the interface as desired for a better continuity conservation and convergence.

Overset Zero Gap interface effect can be observed near the intersection in figure 3.5. Two zero gap layers are set in the background mesh and five in the overset. Polyhedral elements let a more uniform distribution around this area, being easier to control the number of layers and obtaining a more robust interface. As a result, the hole cutting is applied near the gap when the layer condition is satisfied and the gap is then closed by the fly by a virtual wall. Hole cutting is achieved to be acting really close to the intersection, modelling a highly real contact. That

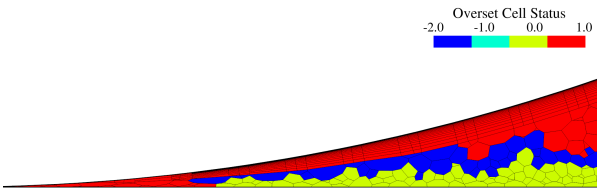

(a) Cutting plane xy at z=0 in background domain.

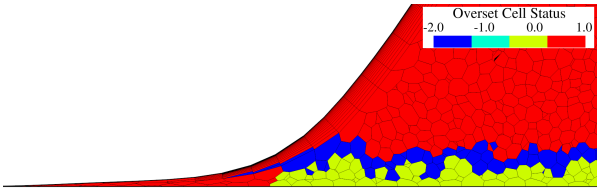

(b) Cutting plane yz at x=0 in background domain.

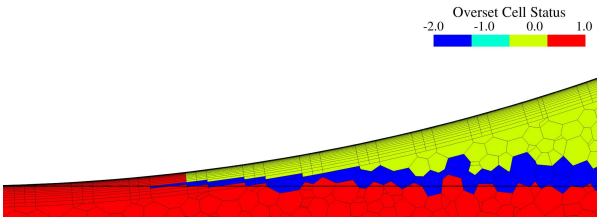

(c) Cutting plane xy at z=0 in overset domain.

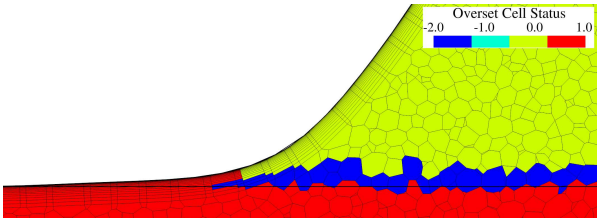

(d) Cutting plane yz at x=0 in overset domain.

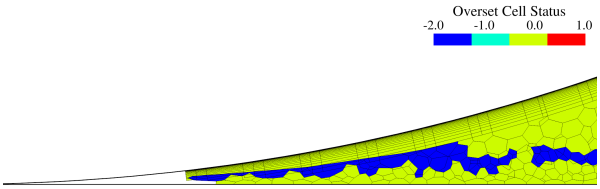

(e) Cutting plane xy at z=0 in merged domain.

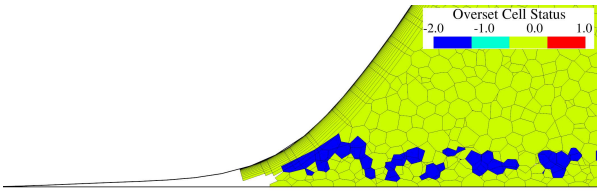

(f) Cutting plane yz at x=0 in merged domain.

Figure 3.5: Overset cell status representation at the interface close to the contact with the ground at xy and yz centrals planes in background and overset domain. Hole cutting results is shown in final merged domains representation. Inactive cells are highlighted in red (1), active cells in yellow (0) and overlapping in blue (-2).

is possible due to the precision and uniformity of both meshes in that area, leading to a robust interface updating process.

	Background	Overset	Merged
Coarse	4,072,941	3,237,789	3,581,226
Medium	11,027,533	8,988,838	9,602,130
Fine	21,905,617	15,819,439	16,512,187

Table 3.1: Number of cells in background and overset domain and final merged grid after hole cutting for coarse medium and fine mesh.

An inflation layer is defined around the tyre and rim surfaces aiming a resolution of $y^+ = 1$ and avoiding wall function treatment. Prism layer mesher is applied with a first element height of $17\mu m$ and 18 layers with a growth ratio of 1.2. This way, a total inflation layer thickness of 2.26 mm is achieved, enclosing the boundary layer thickness of 2 mm inferred from Fackrell's experiment. The number of layers is supposed to be satisfactory for capturing the boundary

layer, plus it is chosen thoroughly to obtain a smooth transition with the unstructured mesh. Due to the similar cell size and the boundary layer collapse control near the contact, a successful overlap interface is achieved in that problematic zone. Unfortunately, inflation layer cannot be defined on the ground. It is complicated to achieve a valid interface since it is impossible to have similar cell size in the overset domain when interacting with the ground, thus wall treatment is activated.

3.1.3 Setup

Boundary conditions

Wind tunnel domain is replicated for CFD simulations as previously shown, trying to set up all the conditions as similar as possible to the experimental scenario. Side and top boundaries are set as symmetry walls, assuming a zero flux of all quantities through it as a zero-shear slip wall. Hence, no refinement is needed near those walls with no interest and the mesh can be enlarged to the outer edges to obtain a high dissipation for undesired disturbances.

Inlet and outlet faces are set as velocity inlet and pressure outlet respectively, with initial and reference data collected on table 3.2. Pressure outlet is defined with zero relative pressure, reproducing atmospheric conditions. Turbulent parameter for both inlet and outlet are based on previous studies [11]. The ground in contact with the wheel is a moving no-slip wall, with the same velocity as the fluid flow at the intake. Finally, the wheel is set as a simple no-slip wall, as this region will be deactivated and computed at the overset domain.

Relative pressure	0 Pa
Intake velocity	18.6 m/s
Angular velocity	89.44 rad/s
Turbulence intensity	0.2%
Turbulent length scale	0.04 m

Table 3.2: Initial and reference values for boundary conditions in CFD simulations.

The overset domain is formed by the wheel (split in rim and tyre no-slip wall boundaries to track the forces separately) and the overset interface at the cylinder volume part shown in figure 3.4. A local coordinate system is created at the wheel axis and a rotating motion is imposed at the overset domain around that axis with the equivalent angular velocity from the intake velocity and wheel radius (see table 3.2). Distance weight interpolation option and close proximity option is enabled at the overset zero gap interface as it is recommended for overset regions overlapping physical boundaries of background region.

Solver

Air fluid flow is modelled in STAR-CCM+ with adapted properties to adjust to experimental wind tunnel conditions. Reynolds number in Fackrell's experiment [2] is 0.53 million based on wheel diameter characteristic length. Thus, considering atmospheric conditions, air dynamic viscosity is determined based on Reynolds number formula.

Equation of state	Constant density
Flow model	Coupled
Discretisation order	3rd-order MUSCL
Gradients	Hybrid Gauss-Least Square
Turbulence model	Realizable $k-\varepsilon$ two-layer all y^+ treatment

Table 3.3: CFD solver models within STAR-CCM+.

Main model specifications assigned for solving current case are collected in table 3.3. Incompressible flow is consider as specified in Governing Equations section due to low Mach number (around 0.55), although density variations could be expected in the vicinity of the contact patch. Segregated flow model is preferred when simulating incompressible flows as it is less computationally expensive than coupled model, however coupled approach is more robust and needs to be applied due to the rotating overset interface to obtain a stable simulation. High order discretisation order can be achieved with no extra oscillation at the force tracking so a higher accuracy can be achieved specially at the wake. Standard hybrid Gauss and Least Square model is applied for gradient computation and realizable $k-\varepsilon$ turbulence model as preciously explained in Governing Equations section.

Time step and convergence

Steady state simulation with tangential velocity from local rotation rate imposed on the wheel surface is run as a first stage to obtain a good initialisation for further transient computation. Due to the cutting domain at the overset interface and contact treatment plus a highly transient conditions, residuals from continuity, momentum and turbulence equations are not able to reach low values (around 1e-2, 1e-3). Convergence is considered based on drag and lift forces on rim and tyre surface tracked every iteration. When forces oscillation becomes smooth and periodic along a constant value, the simulation is considered converged.

Relaxation values are decreased to a value of 0.5 to help convergence. Courant–Friedrichs–Lewy (CFL) number is also manipulated to obtain a reasonable trade-off between stability and convergence speed. Local pseudo time step $\Delta\tau$ is computed with eqn. 3.1 considering CFL and Von Neumann stability conditions ($\sigma \approx 1$).

$$\Delta\tau = min\left(\frac{CFL\,V(\boldsymbol{x})}{\lambda_{max}(\boldsymbol{x})},\ \frac{\sigma\,\Delta x^2(\boldsymbol{x})}{\nu(\boldsymbol{x})}\right), \tag{3.1}$$

where V is the cell volume, Δx is a characteristic cell length, ν is kinematic viscosity and λ_{max} is the maximum eigenvalue of the system. As implicit solver is employed, higher CFL numbers can be used compared to explicit solvers, normally requiring CFL$<$1. A non-dimensional value of 10 is assumed based on trial and error.

Time step is a sensitive decision for a stable and accurate simulation. The most important aspect is about ensuring solver and overset interface updating stability. Moreover, a sufficiently low time step is desired for physically capturing the characteristic frequency of main transient effects. First-order time discretisation is chosen as stability problems are found with second-order at the rear part of the tyre-ground contact interface.

Finally a time step of 0.25 ms is assumed as it is the highest time step producing a satisfactory force evolution along simulated time. Bigger steps led to an undesired high amount of limited turbulent viscosity cells. In addition, it is by far a low time step to capture the main transient features [60]. It is found in DES simulations that main shedding vortex frequency is 180 Hz, corresponding to 5.5 ms. 20 time steps are simulated for every main vortex periodic fluctuation. In addition, a low frequency peak at 9 Hz is found corresponding to transient movement of separation point in the top of the tyre.

Computational cost is really high due to the large amount of cells within the computational domain and the overset approach, thus time-dependent steps must be pushed to the limit. In the same direction, 10 inner iterations are run every time step as it has been observed to be enough to reach a stable force value and smooth transition between each time step.

Hence, a total of 281 time steps with 2810 iteration are taken for every wheel turn. Two wheel turns are run for obtaining an established transient flow field and then five more turns are run for data averaging.

Data averaging

One of the several problems encountered during the thesis is related to transient data averaging in STAR-CCM+. Monitors have to be manually created for every field function that wants to be averaged. While no problem is faced when averaging aerodynamic forces or fluid field function within the background domain, averaging fluid variables in the overset domain is not straightforward.

It is possible to average every field function at every cell but the problem comes when dealing with moving mesh. The average will be still performed at every cell in the domain as it is

translating and cell position is changed. There is no way to take into account the moving reference frame, thus the averaged values in the moving domain will be performed through all the locations every cell have been at.

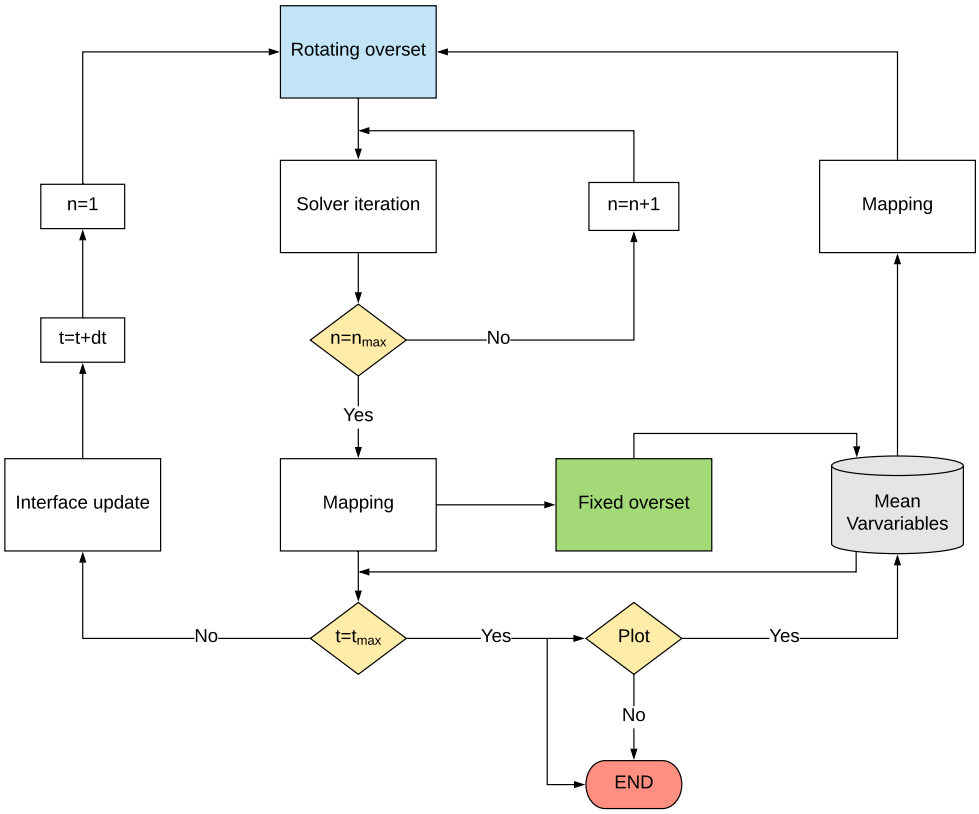

Figure 3.6: Data averaging flow chart for rotating transient CFD simulation. Every time step, variables are mapped from rotating to fixed overset domain where averaging takes place. When required, accumulated averaged vairables can be mapped back to original overset mesh and plotted next to background average values.

A smart solution is developed to achieve averaging in the overset domain. Identical mesh domain is generated where no governing equations are solved nor rotation movement is applied. Then, a volume mapping is carried from the moving overset to the fixed overset domain with the desired flow variables. Data can be mapped every time step and then successfully averaged at the fixed domain. Finally, when averaged results want to be plotted, the reverse procedure is carried and the averaged data is mapped from the fixed domain to the moving overset domain. This way, averaged data can be represented in the real overset domain with a smooth transition to the background domain. This procedure can be easily followed with the flow chart in figure 3.6.

3.2 FEA

Finite Element Analysis is carried to obtain the resultant wheel deformation after applying body load on it and modelling the wheel contact patch with the ground. A first attempt was made within STAR-CCM+ with solid stress module, looking for preliminary results to be tested in a CFD simulation. Unfortunately, it was found that structural modules in STAR-CCM+ were limited and unable to model non-linear contacts as it is the case. Alternative solutions were sought within the available contact interfaces, but all of them turned out to be either too restrictive and leading to unrealistic deformations or too loose and tyre penetration into the ground was experienced.

Hence, the only remaining option to obtain a deformed rotating wheel in contact with the ground that may be employed in a further FSI simulation is carrying a FEA simulation in ABAQUS CAE. A wide range of contact, elasticity and materials models is available to obtain high fidelity results, plus the already implemented co-simulation feature to perform FSI simulations with STAR-CCM+.

Two different tyre models are tested in ABAQUS. First, a uniform simplified linear elastic material is tested. Then, a multi-layer hyperelastic model is implemented based on data found in literature for more realistic FEA analysis.

3.2.1 Geometry

First step for setting up the FEA simulation is creating the volumetric body. CAD profile designed in CATIA V5 for CFD simulations is filled and revolved to create needed body. Cross section of the different tyre models can be seen in figure 3.7. First, simple uniform material section is shown. As there is no information about the tyre in Fackrell's experiment, tyre body is designed based on topology found at different studies focused on deformation and internal loads. Based on Yang's model [5] in subfigure (c), similar thickness and distribution is followed. A thicker section is obtained at the union with the rim and the tread that will be in contact with the ground, while the thinnest section is found in the middle of lateral face. Despite the differences in external profile and union zone, it can be considered that the section is analogous.

Then, a more realistic model similar to Yang's one is developed in subfigure (b). Special attention is brought to replicate accurately sidewall, undertread and tread sections as there are the more sensitive ones for tyre deformation. Small difference may lead to great changes in final deformation and an iterative procedure is followed until a satisfactory solution is found.

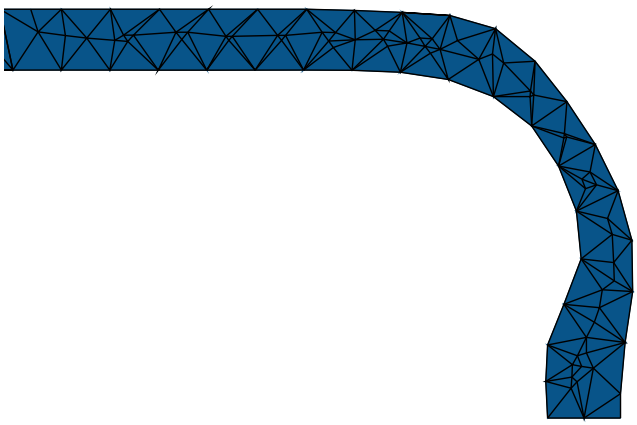

(a) Tyre section with uniform material.

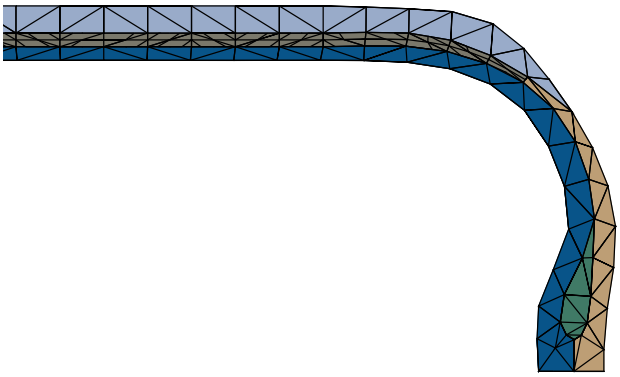

(b) Tyre section with multilayer materials.

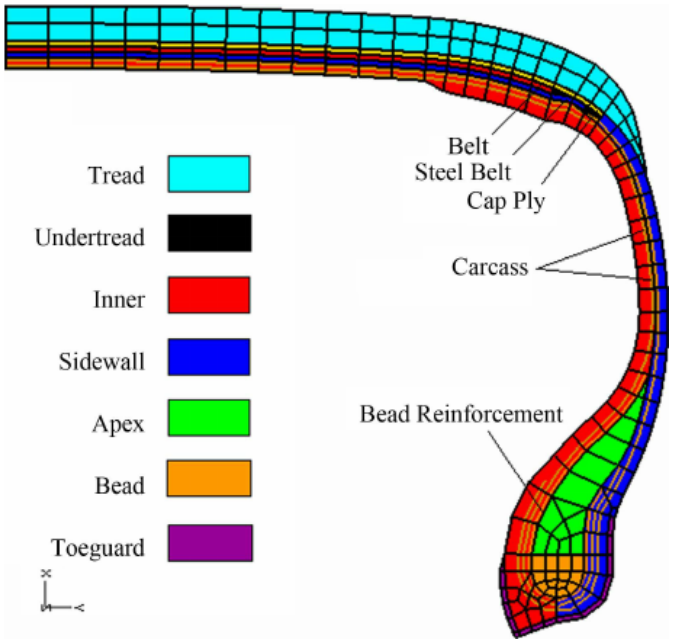

(c) Tyre section with multilayer materials from Yang [5].

Figure 3.7: Linear elastic model with uniform material (a), hyperelastic multilayer material (b) and reference tyre section from Yang [5] (c) for FEA simulations.

Then the profile is revolved at the wheel's central axis for each element and generated solids are exported into ABAQUS. For the linear elastic model, the wheel is split into rim and tyre as seen in figure 3.8. On the other hand, five different elements are separately generated for the hyperelastic tyre model as seen in figure 3.7 (tread, undertread, inner, sidewall and apex/bead).

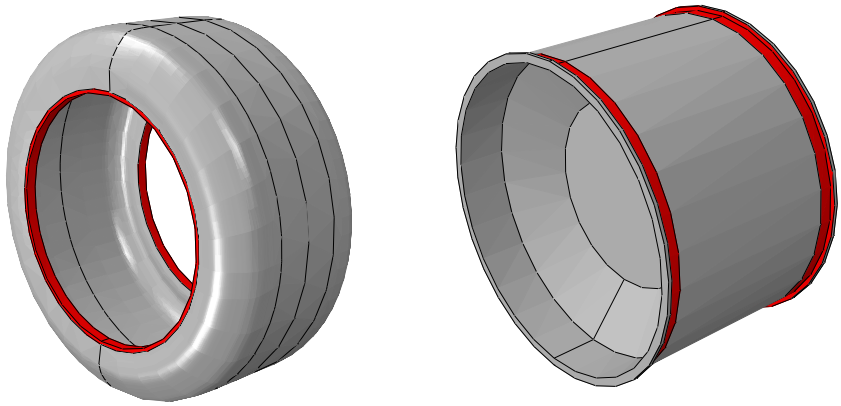

Figure 3.8: Rim and tyre solid volumes imported into ABAQUS for linear elastic FEA simulation.

Next step is assembling the tyre and rim plus a solid plate simulating the ground. For linear elastic case, a simple tie restriction is imposed in the union between the tyre and the rim, highlighted in red in figure 3.8. It is the simplest and more restrictive kind of union, not modelling any kind of stress or separation at that point. Compared to the realistic model, the shape is flat and not detailed as it is not an area of interest and just a simple link is desired.

More complex configuration is faced with multi-layer model. Contact between each part should be preconditioned and manually set a total of eleven constraints between all elements. Despite extra elements that need to be managed, the procedure is homologous to the one applied in linear elastic.

3.2.2 Mesh

The assembly is meshed with standard tetrahedral element C3D4, a 4-node linear type of element from 3D stress family. The number of elements is collected in table 3.4 and a representation of the mesh grid can be appreciated in figure 3.9.

No mesh independence study is carried as no force or deformation is studied quantitatively. The steps followed to consider a valid mesh are to have a fine region in the contact patch, with same element size in the tyre and the ground to have a better cohesion. Moreover, the same element size is also desired in the rim-tyre union to reach a conformal mesh, as appreciated in figure

3.9. Then, a coarser grid is created at the rim since it is considered as a solid body and no deformation is calculated, hence no special accuracy is required.

	Ground	Rim	Tyre	Total
Linear elastic	15,024	15,195	84,806	115,025
Hyperelastic	15,024	26,396	139,264	180,684

Table 3.4: Number of cells in linear elastic and hyperelastic model split in ground, rim and tyre. A higher number of elements is required for hyperelastic model due to higher number of interactions.

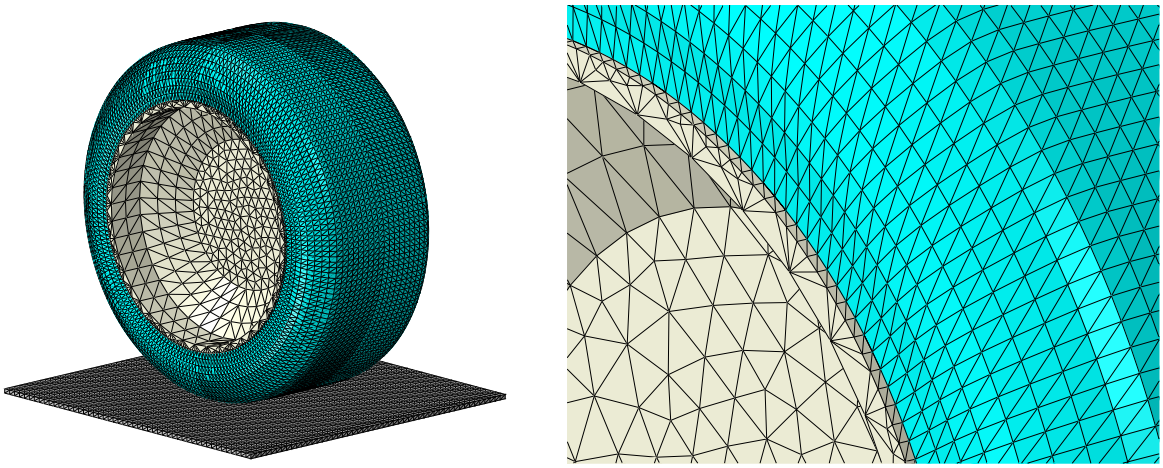

(a) Linear elastic mesh.

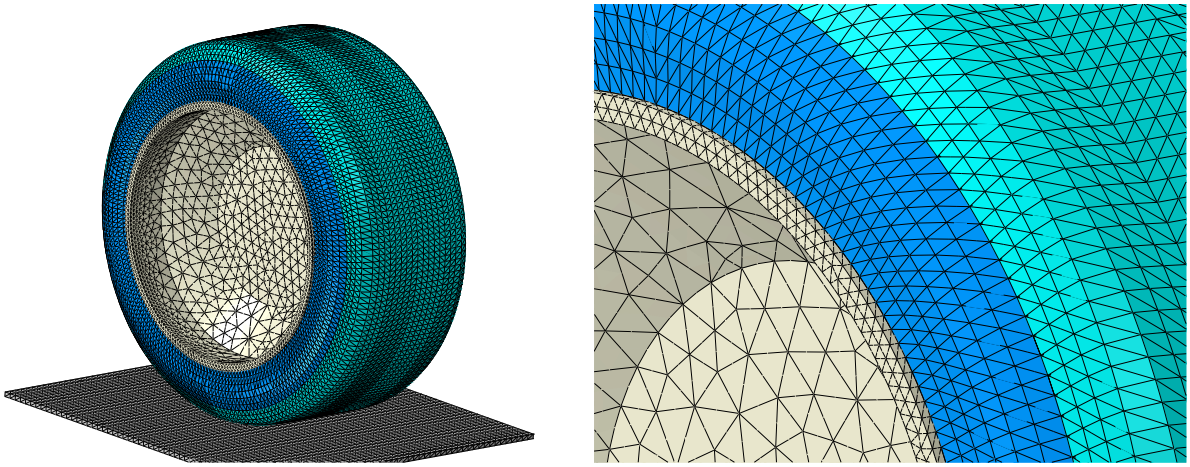

(b) Hyperelastic mesh.

Figure 3.9: Linear elastic and hyperelastic mesh representation. Coarser elements can be appreciated at the rim where no solution is calculated and finer grid at the interfaces where contacts take place. Conformal mesh is achieved at every contact.

3.2.3 Setup

Material modelling

The setup is mainly based on Yang's PhD thesis [5] as it is the reference found in literature with the most extensive numerical and experimental data about open-wheel deformation. Standard pavement and aluminium materials are applied to the ground and rim respectively. Nevertheless, as these parts are constrained and considered as rigid solids, no deformation is obtained and material properties are irrelevant. It is a reasonable assumption as rim and ground deformation is negligible compared to tyre deformation.

On the contrary, tyre material and elastic definition is a key aspect in its deformation. A uniform tyre section is modelled with linear isotropic elastic behaviour and equivalent rubber material properties from Yang's experiments [5] (see table 3.5).

Component	Density (kg/m^3)	Young Modulus (MPa)	Poisson's Ratio
Tyre rubber	$12,000$	40	0.49

Table 3.5: Linear elastic rubber material properties.

Hyperelastic material properties are obtained after experimental uni-axial tests and evaluation through ABAQUS is performed [5]. As a result, coefficients of Yeoh model are collected in table 3.6.

Component	C_{10} (N/mm^2)	C_{20} (N/mm^2)	C_{30} (N/mm^2)
Tread	0.1714	$-4.4041e-2$	$1.7382e-2$
Sidewall	0.2933	$-8.6149e-2$	$3.7144e-2$
Apex	1.7245	-2.2922	5.054
Inner-liner	0.3223	$-8.6751e-2$	$2.4762e-2$

Table 3.6: Hyperelastic rubber material properties for Yeoh strain model [5].

Reinforcement component in the undertread is essential for the overall performance of tyre deformation. It is made of anisotropic cord-rubber composite, where the cords present a high modulus and low elongation and rubber forms the support where more external loads are absorbed. In ABAQUS, rebar element model can be implemented embedded intro rubber matrix. However, it is a high precision modelling that is out of the scope of present study. Instead, it is usually employed high rigidity linear elasticity as the strains in the cords vary slightly as collected in a summary table by Yang [5]. Same strategy is followed and undertread linear elastic properties are foun in table 3.7 based on previous studies and tuned until a satisfying deformation is obtained.

Component	Density (kg/m^3)	Young Modulus (MPa)	Poisson's Ratio
Undertread	12,000	300	0.3

Table 3.7: Linear elastic material properties for undertread component.

Loads and Boundary conditions

Once the model is set, deformation simulation is analogous for both cases. Two steps are defined for the FEA simulation. At the initial stage, wheel and ground are separated. Then, inner pressure is applied on the wheel and the ground is moved towards the wheel, starting a compression process until final deformation is reached.

A surface to surface contact interaction is created at the initial step and propagated to the main step with a Lagrange formulation. The ground upper surface is set as master surface (it is suggested in User's Manual [4] that master surface should be assigned to the stiffest body) and the external tyre surface is set as slave. Different methods are found in ABAQUS to treat overlap of contact surfaces. The main reasons that could lead to overclosure or penetration problems are a poor quality CAD model and discretisation error due to different element size [61]. A strain-free adjustment is applied to avoid undesired overlaps. Nodes on the slave surface are moved to remove the penetration without stress or strain occurring.

Inspired in Wang et al. procedure [62], the contact properties between the ground and the tyre are defined within a tangential and normal behaviour. Normal contact condition is necessary in order enforce impermeability in the normal direction. A penalty friction formulation is applied for normal and tangential formulation with a friction coefficient of 0.2. Penalty method carries a reduced computational cost when many nodes are involved in contact and is quite robust for complicated contact situations. Moreover, a hard contact approach for pressure-overclosure is defined as the penetration of the slave surface intro the master surface at the constraint locations is minimised and no transfer of tensile stress across the interface is allowed.

Loads and boundary conditions are based on Yang's PhD thesis [5] and carefully varied to obtain a stable and more realistic simulation. The rim is fully constrained and the pavement is led a single degree of freedom to be able to move in vertical direction to simulate the compression. Hence, the tyre is just constrained to the rim at the contact surface and free to be deformed. Inflation pressure of 80 kPa is applied in the inner surface of the tyre and a displacement of 9 mm is imposed at the pavement towards the tyre to get acompression equivalent to 1kN downforce. This is the usual procedure for wheel contact modelling as seen in related literature [63, 64, 62, 65].

Wheel rotation

One of the aims of the project is to create a valid methodology to further implement a two-way coupled FSI simulation. Then, wheel rotation in ABAQUS is implemented just to be tested. A reference point coordinate system is created on wheel axis and the rim is constrained to this point. This way, if any motion is applied to the reference point, it will be directly transferred to all nodes in the rim and consequently to the tyre through the tie constraint previously defined.

Direct rotation over the ground leads to overclosure problems, thus an alternative strategy is planned:

1. Static wheel deformation is calculated.
2. The ground is again separated from the tyre.
3. Wheel rotation is carried freely corresponding to the desired time step.
4. Static wheel deformation is repeated after wheel rotation.

This way, meshing nodes in CFD simulation will be able to be updated and adapted to the expected wheel deformation every time step.

Chapter 4

Results and discussion

The most relevant and concluding results are shown and discussed bellow with a representative structure that resemble the work flow followed (see figure 4.1).

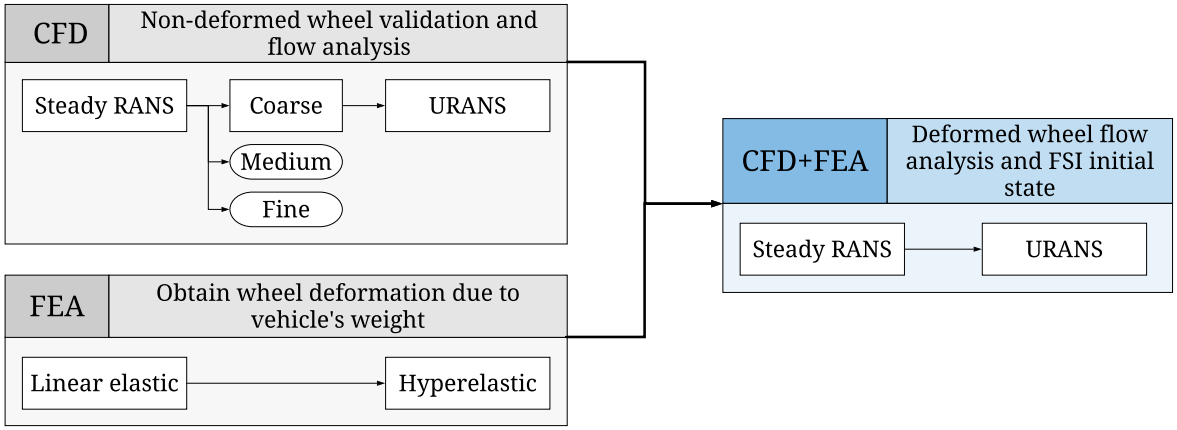

Figure 4.1: Chart showing the work flow and structure of the results chapter. CFD and FEA simulations are carried independetly at first stage for solid wheel to finally perform steady and unsteady RANS simulation with the deformed wheel.

First, steady RANS simulations are carried with three meshes at different refinement levels for the standard wheel geometry. After results are validated, URANS simulation is set up with rotating overset interface to model the real motion and the contact with the ground. In a parallel way, wheel deformation and contact due to vehicle's weight is modelled with linear elastic and hyperelastic materials.

Finally, CFD and FEA results are merged in order to study the flow features and aerodynamic behaviour of a deformed wheel. Deformed wheel geometry is exported and CFD case for non-deformed wheel is adapted to run steady and unsteady RANS simulation. As FSI coupling is

not set, wheel rotation cannot be model. Instead, URANS simulation is carried with a rotating boundary condition over the fixed wheel.

4.1 CFD for solid wheel

Steady and unsteady RANS simulations are carried with the model exposed in previous chapter. The aim of steady simulations is to ensure that the setup is correct and compare the differences between the mesh grids generated. Based on that comparison, the mesh offering the best trade off between accuracy and computational cost is established for further simulations. Moreover, steady solution is useful to ensure a good initialisation for transient simulations. Time averaged and instantaneous solution is deeply analysed and compared to steady results and experimental data.

4.1.1 Steady RANS

Three meshes are tested with experimental data to validate the simulation and ensure that the domain discretisation is correct and is not the source of any error. With a coarse mesh of around 3.6 million cells as starting point, two additional grids are generated with consecutive and equivalent base size reduction, leading to 9.6 and 16.5 million elements respectively. Further details can be checked in previous chapter.

Aerodynamic forces

Aerodynamic forces are normally employed for preliminary validation. Experimental lift and drag is provided separately for the rim and the tyre by Fackrell [2]. Pressure probes are distributed along the surface and the signal is lately processed and integrated to obtain the aerodynamic forces.

Experimental and numerical values for the aerodynamic coefficients, based on frontal wheel area and freestream conditions, are arranged in table 4.2 for the tyre. Relative error is added next to every numerical value to quantify the uncertainty in the results with respect to experimental data.

Great agreement is achieved for drag coefficient. Identical values (taking into account experimental data precision) are reached with both coarse and medium mesh, while it is slightly underpredicted although still inside an acceptable range by fine mesh. Lift results are oppositely far from experimental data, being increasingly underpredicted as the mesh is refined. It is

	CD Tyre	Relative error	CL Tyre	Relative error
Fackrell	**0.51**	-	**0.28**	-
Coarse	0.51	0%	0.19	32.1%
Medium	0.51	0%	0.18	35.7%
Fine	0.48	5.9%	0.09	67.9%

Table 4.1: Drag and lift coefficient based on frontal area obtained from steady RANS simulation for solid wheel with coarse, medium and fine mesh. Relative error is shown upon experimental reference data from Fackrell [2]. Drag coefficient is perfectly predicted by coarse and medium mesh while a great uncertainty is obtained from lift coefficient. The lowest uncertainty is achieved with coarse mesh.

definitely not an acceptable value and a deeper analysis is required to understand the source of this uncertainty.

Results from experimental data should never be unconditionally trusted as errors may be committed during the experimental setup and data acquisition, plus the inherent uncertainty linked to every measuring tool. Actually, it is stated in Fackrell's thesis [2] that results obtained for lift and drag coefficients should be within 5% of the true value. Nevertheless, observed uncertainty on lift results are too large to be due to discrepancies between numerical simulation and experiment.

Pressure coefficient distribution

Static pressure signal is then analysed in order to validate obtained results with higher fidelity. It is a direct measurement where the simplification of integrating a few discrete measurement along the surface is avoided. Moreover, a distributed value is analysed and discrepancies can be identified locally. Data from central pressure probe on tyre tread is represented in figure 4.2, as it is the most representative one and a good insight into different flow features is provided.

Pressure coefficient distribution from coarse, medium and fine mesh are compared to experimental data. Firstly, stagnation point can be identified with pressure coefficient values equal to unity. If referred to pressure coefficient definition in equation 4.1, stagnation and freestream static pressure difference ($p - p_\infty$) is equal to freestream dynamic pressure (q_∞) at stagnation point. Every simulation predicts a slightly higher pressure peak and later stagnation point as experienced by McManus [11].

$$c_p = \frac{p - p_\infty}{q_\infty} = \frac{2\,(p - p_\infty)}{\rho u_\infty^2}. \tag{4.1}$$

The flow is accelerated up to a suction point at $\theta = 50^{\text{o}}$ and then pressure is increased aggressively until the contact patch is reached and maximum pressure peak is found. Sudden

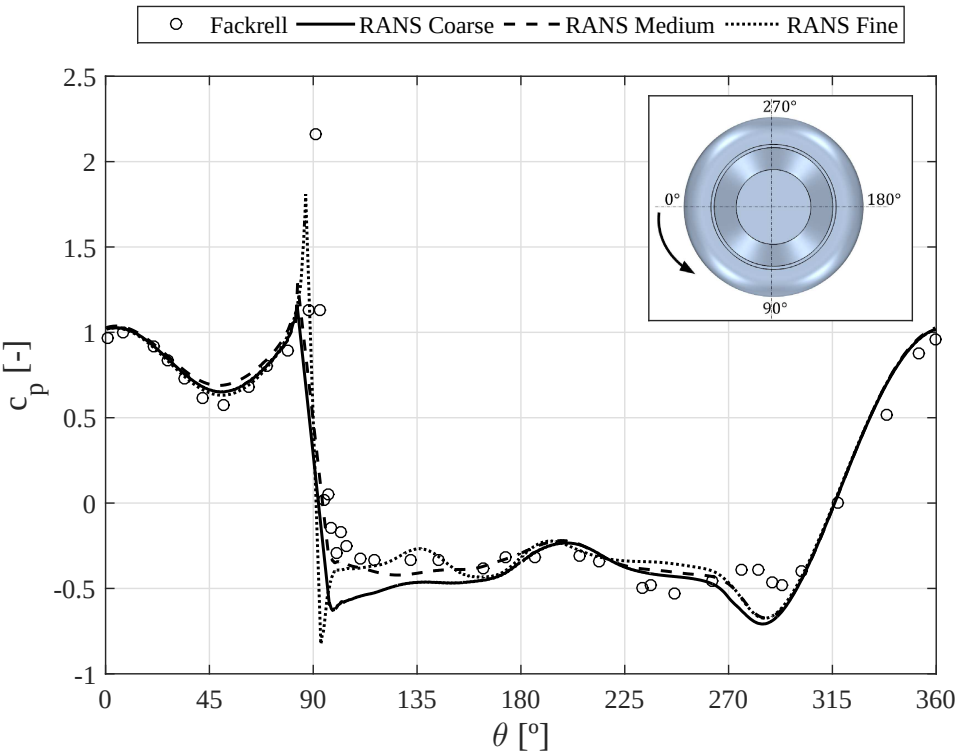

Figure 4.2: Static pressure coefficient distribution over the central line of the solid wheel from steady RANS simulations with coarse, medium and fine mesh. Experimental data from Fackrell's experiment [2] is also included for reference. Good agreement is observed overall but on the separation point at the top part of the wheel ($\theta = 270^{o}$ instead of $\theta = 280^{o}$). Discrepancies are also observed on the tubulent region at the rear part of the contact patch ($\theta = 90^{o} - 140^{o}$), where the best results are obtained by medium mesh.

pressure increase is due to viscous effects created by the intersection shear-layers at the frontal contact patch area. That effect is defined in Fackrell's work as jetting phenomenon and lately corroborated in several publications [11, 8].

Suction peak is underestimated with medium mesh by 21% and around 11% with both coarse and fine mesh grids, thus the flow is not as accelerated as expected before reaching the contact patch.

Since the contact is not fully modelled, there exists a gap that is decreased as the mesh is refined (from 14^{o} in coarse mesh to 6.6^{o} in fine mesh) where no solution is obtained. Thus, the maximum pressure peak cannot be evaluated. Nevertheless, it can be observed that the trend of pressure distribution is reaching a sharp edge similar to the one captured from experiment.

After the contact patch, the reverse effect is experienced. The increasing separation between the wheel and the ground surface draws the air out of the contact patch and a low pressure region is generated [8]. Some little fluctuations are noticed in the experiment, which are meant to be provoked by signal oscillations due to the proximity of the sensor to the ground. Pressure value right after the contact patch is from both coarse and fine mesh is not in agreement to experimental data, while medium mesh is able to reproduce a similar distribution.

Fackrell [2] theoretically predicted the reverse jetting phenomena although it was unable to predict consistently the suction peak after the contact patch. Mears [8] was able to predict this effect with both experimental and computational studies, capturing a pressure peak $c_p = 1.95$ and a suction peak afterwards of $c_p = -1.5$. It is an effect widely supported by several computational an experimental results performed lately [11, 12, 60, 31]. Hence, experimental pressure values near the contact of a rotating wheel are not reliable and a suction peak after the contact patch is indeed expected.

From $\theta = 100^o$ to $\theta = 220^o$ a more uniform region with some fluctuations due to little recirculation zones is overcome. That region is successfully predicted by simulations with some little differences. Then, a sudden pressure drop related to recirculating flow is noticed at $\theta = 247^o$, that is better captured by coarse mesh.

Finally, one of the most important and difficult features to be captured is found at $\theta = 280^o$. The increasing pressure coefficient distribution meets a point where a sudden suction peak is experienced. The point where the pressure starts decreasing is related to the separation point on the top of the wheel. Unfortunately, a sooner separation is predicted by CFD simulations, all of them exactly on the top of the wheel. Again, separation point is complicated to be captured either with experimental methods or numerical simulations. While an even earlier separation point is expected by Mears at $\theta = 290^o$, several experimental [12, 66] and numerical [12, 60, 11] studies for homologous rotating wheels predict separation closer to $\theta = 270^o$.

All the simulations equally predict the suction peak location at $\theta = 286^o$, closer to the suction peak obtained from experimental data at $\theta = 293^o$. Then, pressure is increased rapidly until the stagnation point is reached again, due to the flow acceleration experienced from the stagnation point to the top of the wheel.

Mesh independence

Indeed, a more reliable analysis of different mesh grids performance can be made with the pressure coefficient distribution rather than aerodynamic coefficients. It is demonstrated that, despite the big uncertainty on lift coefficient, overall flow is well captured by CFD simulations.

Similar aerodynamic forces results are obtained by McManus [11], where it is demonstrated that the discrepancies with lift prediction are due to the error in the experimental surface pressure measurements around the contact patch, specially because of the exaggerated width of the pressure peak and the lack of suction peak on the rear contact patch. At the same time, it is stated that the effect of separation point misprediction on lift is smaller compared to the source of error from the contact patch. Drag is quite insensitive to the pressure near the contact line and hence the obtained results are in better agreement.

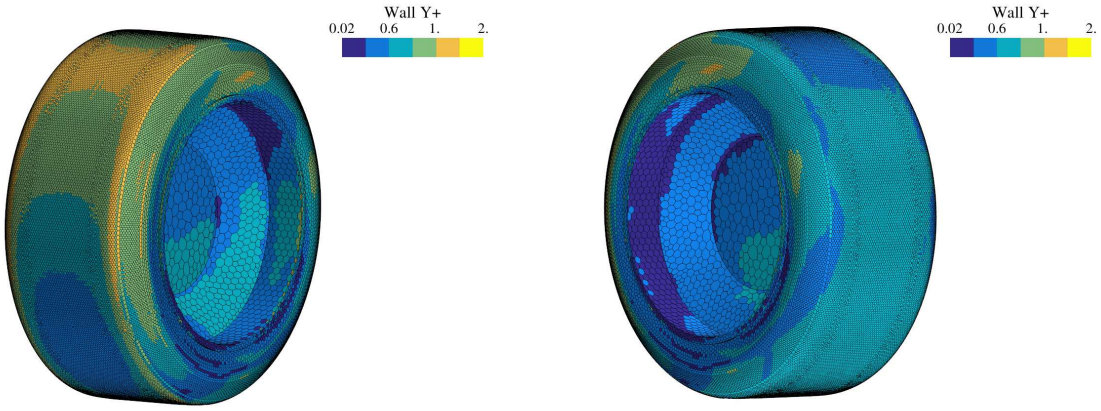

(a) Front view. **(b)** Rear view.

Figure 4.3: Wall Y^+ representation of the solid wheel from steady RANS simulation with coarse mesh (Front (a) and rear view (b)). $Y^+ \leq 1$ around most of the wheel, maximum values $Y^+ < 2$ on therear contact patch and front-top part and shoulders of the tyre, low values $Y^+ < 0.6$ found on the rim and rear part of the tyre.

Differences between the three grids are not remarkable in most of the pressure distribution and no special improvement is found with finer grids. Discrepancies are found at regions where it is demonstrated that experimental results are not reliable. Based on these statements and the satisfying pressure coefficient distribution and aerodynamic forces results, the coarse mesh is considered valid and suitable for further simulations and results analysis.

Mesh resolution at boundary layer is a key aspect to ensure that the flow is properly resolved. Even though a $y^+ = 1$ is imposed beforehand, it needs to be checked that it is actually accomplished. Moreover, initial calculations are made based on freestream velocity and viscosity, thus y^+ is not uniform along the surface. Wall y^+ around the wheel can be appreciated in figure 4.3 from upstream (a) and downstream (b) point of view. Most of the surface is indeed showing a value equal or lower than unity with maximum values lower than two found near the rear contact patch and in the front-top part of the tyre and the borders where high velocities are experienced. In contrast, low values are found in the rim and in the rear part of the tyre.

Wake analysis

Total pressure coefficient is represented in figure 4.5 at different transversal slices at the rear wheel and near wake defined in Fackrell's experiment [2] (see figgure 4.4). The contour is plotted up to a value of 0.9 as it is supposed to capture the vortex edges regarding to Fackrell's experiment. In addition, velocity line integral convolution vectors are printed at the slice to offer a better flow visualisation.

Unfortunately, experimental results are just available for B2 wheel (32.6% wider) and comparison cannot be made for case validation. As the rim is deeper, vortices generated are strongly af-

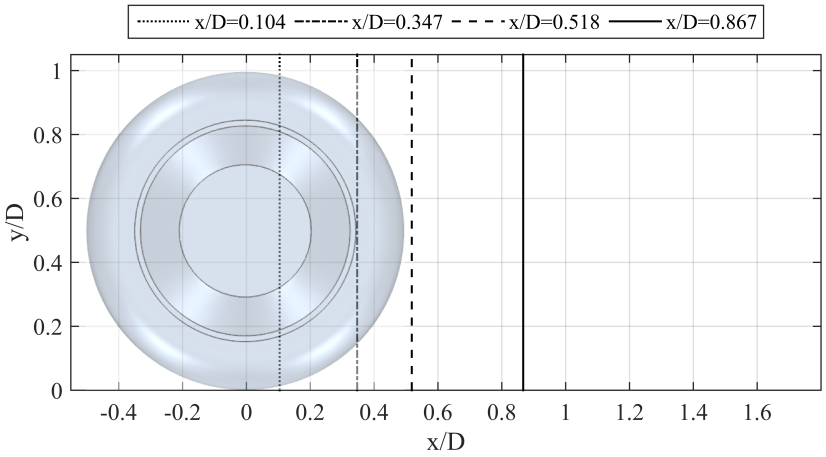

Figure 4.4: Cross section planes location from Fackrell experimental measurements.

fected and experimental results are not worth it to be quantitatively compared. Then, Fackrell's data plus results from other similar studies [12, 8, 3] are referred for qualitative comparison.

Many features can be inferred from the first section downstream the symmetry plane (a). The recirculation bubble can be appreciated on the top of the wheel, followed by a wider structure coming from the two strong counterrotating vortices located at both sides of the rim in a highly turbulent area. Asymmetry in the flow is experienced due to the rim geometry. Vortex structure gets narrower downwards, experiencing as well little vortices and recirculation zones, until the bottom part of the tyre is reached and a big vortex is found. The flow upstream the contact patch is accelerated when approaching the decreasing space between the tyre and the ground. When the contact patch is encountered, the flow is pushed outwards at both sides of the contact patch with high velocity generating the jetting phenomena.

Next cutting plane (b) is right after the rim and two clear regions can be differentiated at this point. Recirculation bubble is increased and merged with the dominant vortices generated at the rim. At the bottom region, the jet wake from the contact patch in enlarged as well.

Near wake structure can be studied at sections (c) and (d). Still two regions can be appreciated at the top and bottom parts plus a smaller vortex structure at both sides of the middle part. As the flow goes downstream, the lower region is energised and become even more predominant due to the vortices at the middle part that are merged to it. Two clear and strong counterrotating vortices can be observed at the latest section while the upper wake starts dissipating.

Complementary information of flow field around the wheel is obtained from longitudinal cutting plane at center line. Non-dimensional velocity magnitude is represented in addition to velocity streamlines constrained at given plane to offer a clear flow visualisation in figure 4.6. No experimental data is available for comparison although a good agreement with previous studies is found [11, 9, 3, 18]. It can be checked how, even though it is a steady simulation, a

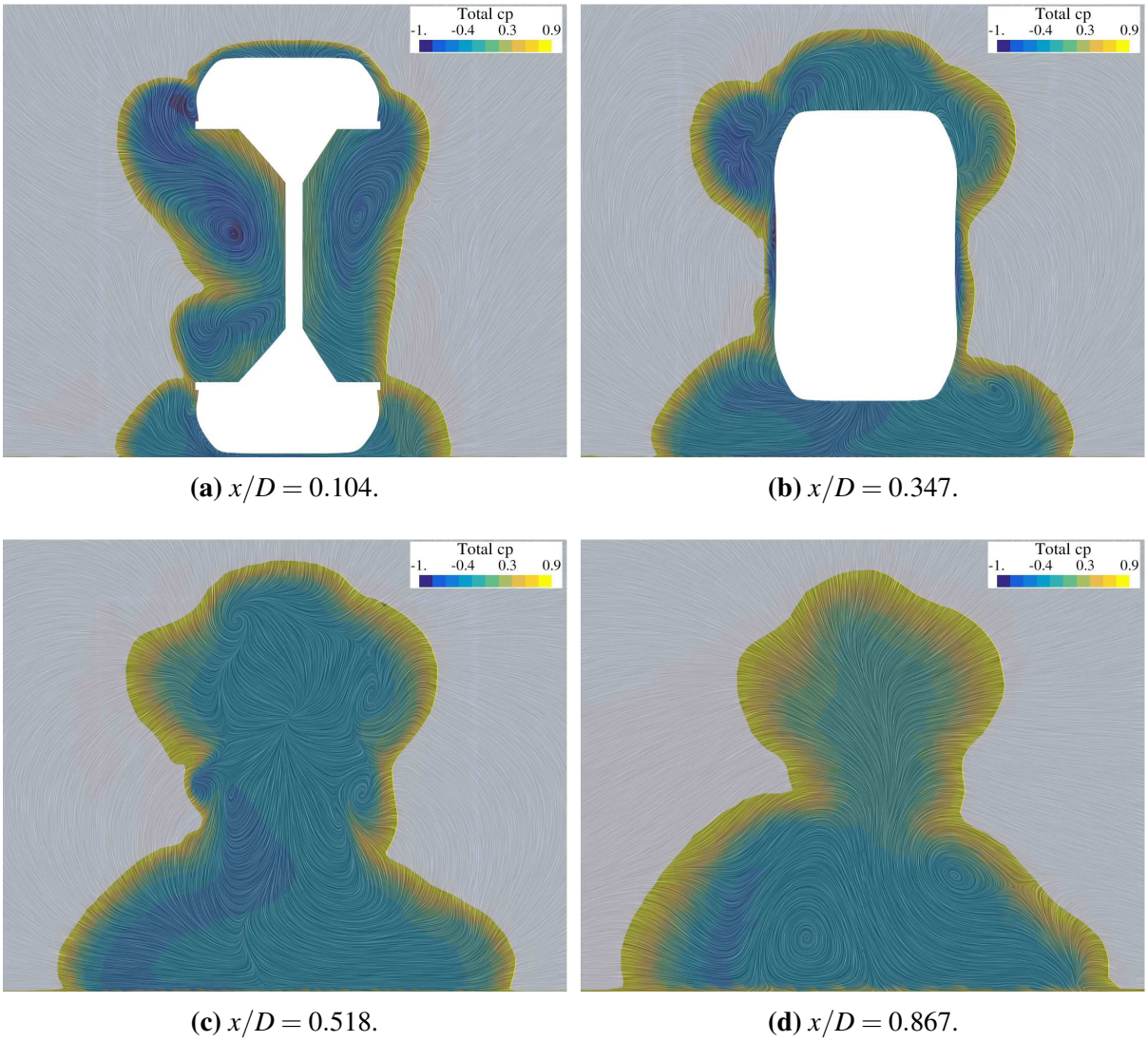

(a) $x/D = 0.104$.

(b) $x/D = 0.347$.

(c) $x/D = 0.518$.

(d) $x/D = 0.867$.

Figure 4.5: Total pressure coefficient contour with velocity line integral convolution vectors at different transversal slices (see figure 4.4) on the rear part and near wake of the solid wheel from steady RANS simulation. Bubble recirculation on the top tread, vortices generated at the hub and jetting phenomena can be identified, evolving into three differentiated vortex structures in the near wake that tend to be merged in two strong counterrotating vortices on the lower area.

rotating wheel with moving ground is modelled with corresponding tangential velocity imposed at boundary conditions. It is important to highlight that steady simulation performed in current study cannot be compared to steady simulations found in literature, referred to zero tangential velocity for both the ground and the wheel.

Analysis from pressure coefficient along the central line in figure 4.2 can be reinforced and better understood with figure 4.6. The front wheel is reached by the air flow and it is split at the stagnation point going downwards and upwards. Air travelling downwards is accelerated due to wheel curvature and rotating motion and ground velocity until a high pressure area near the contact is met. Flow travelling upwards is accelerated and maximum velocity is reached at

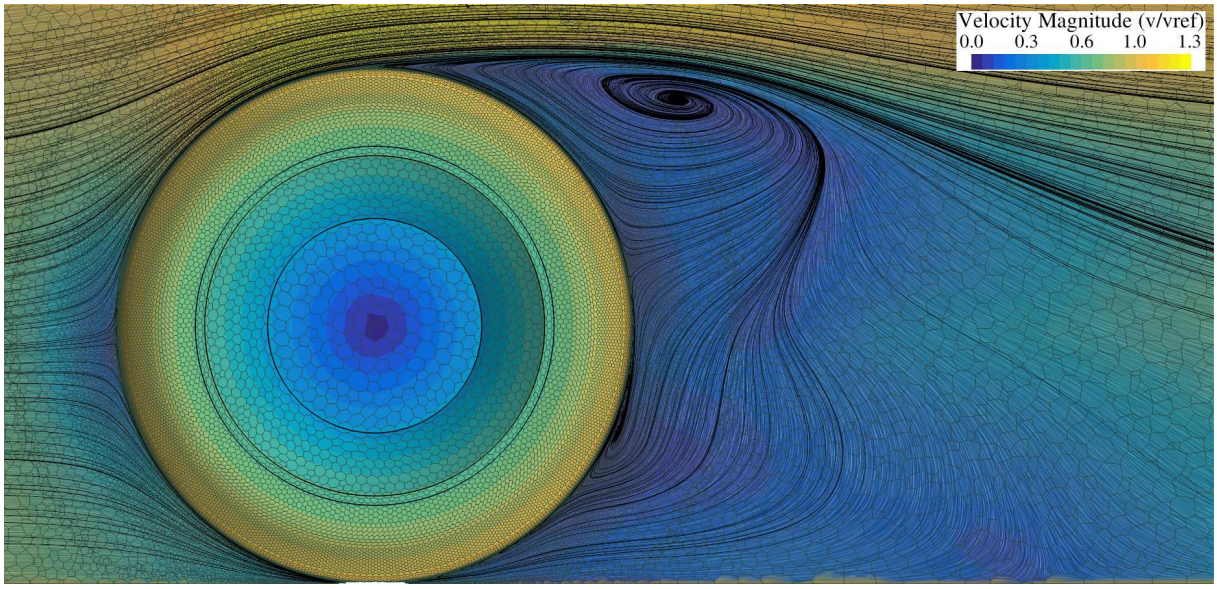

Figure 4.6: Non-dimensional velocity magnitude contour at central longitudinal plane with velocity line integral convolution vectors and constrained streamlines of the solid wheel from steady RANS simulation. The flow going downwards is accelerated until high pressure area is reached at the contact. The flow going upwards is highly accelerated and separation point is found on the top of the wheel. Recirculation bubble is observed on upper rear part and smaller vortex generated on the lower rear part of the wheel. The flow is suctioned at the rear contact patch and redirected to the wheel and the ground following their motion.

this point, 30% greater than freestream velocity. Although the flow is travelling in an opposite direction than wheel rotation, the flow is freely accelerated due to wheel curvature and the absence of any obstacle. Pressure difference between the top and bottom part of the wheel is responsible for lift force generation.

Flow separation is appreciated at the top part as shown more accurately by pressure coefficient distribution. As predicted by Fackrell [2] and shown in introduction chapter, a thin layer next to tyre surface is travelling in the rotating direction while flow is travelling streamwise. When adverse pressure gradient is faced and viscous effects become dominant, energy loss in laminar flow provoke separation over the thin shear layer.

After separations point, a recirculation bubble is clearly captured at high pressure area. The vortex is influenced by high velocity freestream flow following the wake after separation and flow coming upwards from the rear part of the rotating wheel. It is one of the most consistent flow features experienced, thus it is easily captured by steady RANS. Part of the flow coming out of the vortex is ejected to the wheel at a point identified in figure 4.2 as a pressure peak in $\theta = 200^{o}$. Part of the flow then redirected to the top part of the tyre and is in constant interaction with flow separation.

The rest of the flow coming out from the vortex is pushed downwards to lower pressure area at the rear part. Due to the flow tendency to follow wheel movement, a second vortex is appreciated at the rear bottom part weaker than the previous one. It is a low velocity area with

high recirculation and several separation and reattachment points. The effect on the rear contact patch can also be observed, where the flow is suctioned and further expelled following ground and wheel motion.

A bigger picture is also inferred from figure 4.6. Near wake can be clearly identified up to approximately a wheel radius ($x/D \approx 0.5$) with wider profile on the upper and lower part. Then, a transition to far wake is observed, where the near wake is overcome by freestream flow and the wake becomes narrower and located on the lower region.

Near wake behaviour previously analysed is represented in a three dimensional way by means of Q criterion isosurfaces and velocity line integral convolution vectors in figure 4.7. Isosurface is flooded by turbulent charge field function available in STAR-CCM+, defined in equation 4.2 as the divergence of lamb vector $\boldsymbol{L}$.

$$n = \nabla \cdot \boldsymbol{L}. \tag{4.2}$$

Lamb vector is defined in equation 4.3 as the cross product of velocity and vorticity.

$$\boldsymbol{L} \equiv \boldsymbol{v} \times \nabla \times \boldsymbol{v}. \tag{4.3}$$

The main reason of applying mentioned variable is related to visualisation rather than physical meaning. Opposite sides of vortex structures are flooded by high contrast colours and vortex identification is clarified.

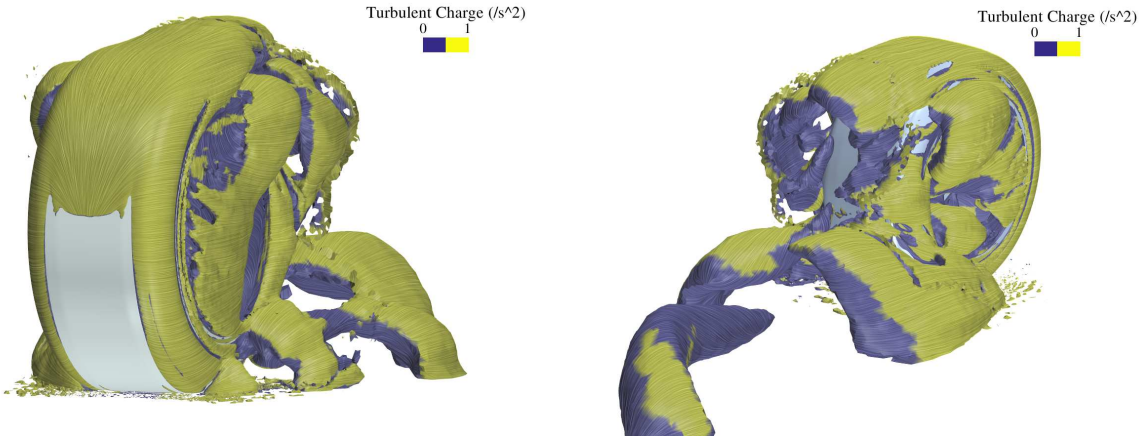

(a) Front view. **(b)** Rear view.

Figure 4.7: Isosurface of Q criterion (4000 s^{-2}) with velocity line integral convolution vectors and turbulent charge contour of the solid wheel from steady RANS simulation. Jetting phenomena and arch-shaped vortex in the lower rear part arebarely captured. Recirculation bubble and arch-shaped vortex generated afterwards are fairly captured. Exagerated vortex is predicted coming from the upper rim cavity.

Vortex structures observed in figure 4.6 can be identified in figure 4.7. Comparison regarding

vortex structures can be madre with McManus work [11], which is one of the most detailed and referenced analysis about wheel wake features.

Jetting phenomena can be specially identified from front view. It is observed how the flow is expelled from the contact patch but not a defined jet is captured. High turbulence is observed in the hub from where a vortex is generated on the upper part and further extended. From the front wheel, the stagnation line can clearly seen, from where the flow is extended upwards to the recirculation bubble and sidewards to tyre shoulder, where small vorticity can be observed at the transition with the rim edges.

A clearer picture of the near wake is observed from the rear view. On the upper rear area, the flow is detached and an arch-shaped vortex is formed with recirculating flow. As observed in experimental studies with rotating wheels [2], a similar height and width is maintained in the separation region. Low velocity flow on the hub cavity and main flow stream surrounding the wheel sidewards interact and shear layers form another arc shape vortex. It is then extended from the upper rim cavity around the shoulders into the upper wake, interacting with the arch-shaped vortex from the tyre tread. Vortices coming from the hub cavity are not completely in agreement neither with experimental data nor most CFD studies. The vortex generation itself is expected indeed, but an exaggerated vortex width is observed. Similar behaviour is experienced with URANS simulations from Dassanayake et al. [31] and the effect is corrected with DES and LES simulations.

Moreover, a more clear jet coming from front contact patch is observed from the left side of the wheel. It is slightly interacting with the vortex coming from the opposite side in the rear bottom area with an arch shape. Far wake is not clearly captured due to RANS limitations.

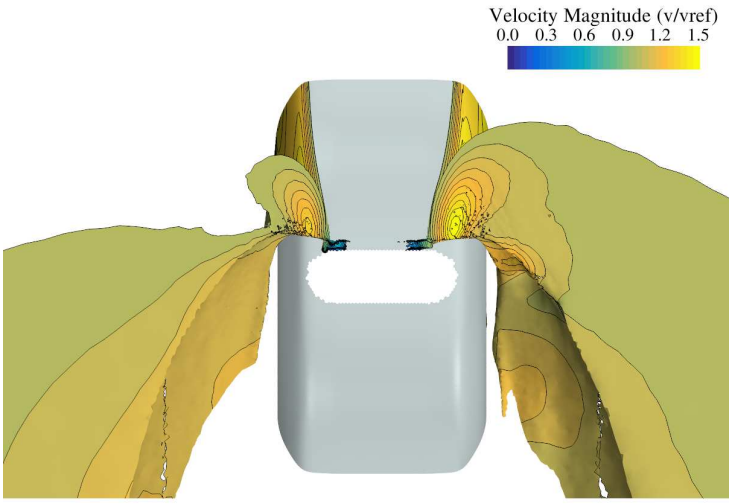

Figure 4.8: Isosurface of total pressure coefficient (0.9) at the contact patch with non-dimmensional velocity magnitude contour of the solid wheel from steady RANS simulation. Flow encounters a high pressure area at the frontal contact patch and it is expelled sidewards creating the jetting phenomena.

Information from the contact patch and how the flow is behaved is observed in figure 4.8. Isosurface of total pressure coefficient of 0.9 is shown to capture the jet shape. It can be observed how the flow is concentrated on the frontal contact patch in a high pressure area. After sudden stagnation, the flow is highly accelerated (up to 50% higher velocity than freestream) and expelled sidewards with a lower velocity than freestream. Asymmetry found in figure 4.7 is clearly seen in figure 4.8. While the flow is clearly directed on the left side, on the right side the expelled flow is recirculated and not a clear jet is predicted.

4.1.2 URANS

Next step is taken for the non-deformed wheel CFD simulation from steady RANS results obtained with the coarse mesh. Unsteady RANS simulation is run from previous solution and solution is time-averaged when the flow is settled after three turns of the wheel for five more turns.

Aerodynamic forces

Aerodynamic forces compared to steady RANS and experimental data despite the uncertainty commented above. Both aerodynamic coefficients are decreased compared to coefficients obtained from previous simulation, being the uncertainty increased noticeably. This effect is observed in higher degree in literature when comparing steady fixed wheel simulations to unsteady rotating ones [11, 60]. Here, the difference is smaller since a rotating condition is imposed on the steady simulations and just the difference in solver time discretisation is assessed.

	CD Tyre	Relative error	CL Tyre	Relative error
Fackrell	**0.51**	-	**0.28**	-
RANS	0.51	0%	0.19	32.1%
URANS	0.45	11.76%	0.16	42.9%

Table 4.2: Drag and lift coefficient based on frontal area obtained from steady and unsteady RANS simulation for solid wheel. Relative error is shown upon experimental reference data from Fackrell [2]. Forces are decreased with unsteady solver.

Results obtained from URANS simulations by McManus [11] are the ones in greater agreement with results obtained in this work. For the finest mesh, a drag coefficient of 0.475 and lift coefficient of 0.152 is obtained with Spalart-Allmaras and 0.434 and 0.156 respectively with Realizable $\kappa - \varepsilon$ turbulent model.

Aerodynamic coefficients are not enough for validating the results and further analysis has to be carried as previously done with steady case.

Pressure coefficient distribution

A more detailed analysis can be inferred from static pressure coefficient distribution in figure 4.9. Experimental and steady RANS simulation with coarse mesh from figure 4.2 is remained and time-averaged solution from URANS is added to be compared.

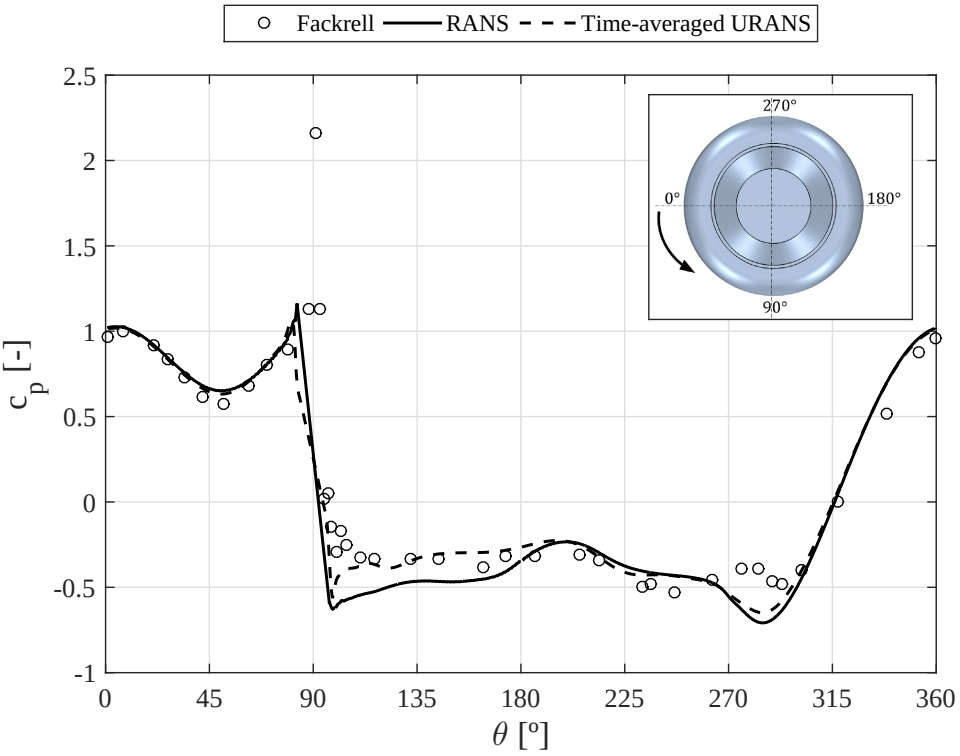

Figure 4.9: Static pressure coefficient distribution over the central line of the solid wheel from steady and time-averaged unsteady RANS simulations. Experimental data from Fackrell's experiment [2] is also included for reference. Difference is observed on rear wheel region, obtaining a better agreement with experimental data.

Main differences with respect to steady results are found at the rear region of the wheel, where highly unsteady and turbulent effect are expected. Suction peak is captured again after the contact path but a more realistic behaviour is captured by URANS. Pressure increase is more aggressive after the suction peak and the pressure signal is rapidly adapted to the pressure distribution captured by experiment procedures. The surface region up to the middle plane in $\theta = 180^{o}$ is although still captured too smoothly.

Region from the pressure peak at $\theta = 220^{o}$ up to the separation point at $\theta = 270^{o}$ is quite similar although a slightly better adapted distribution can be seen with URANS. Then, the separation point is predicted at the same point, being insensitive to any grid or solver modification tested. Finally, the minimum pressure after the separation point is predicted to be a 7% lower with respect to RANS result, getting closer to experimental data but still far to predict this region in a similar way.

Wake analysis

Flow features are studied in depth in a consistent way with the same variables and representations seen in steady simulation section. First, total pressure coefficient up to 0.9 is represented in figure 4.10 at standard transversal slices established at Fackrell's experiment and replicated in present study.

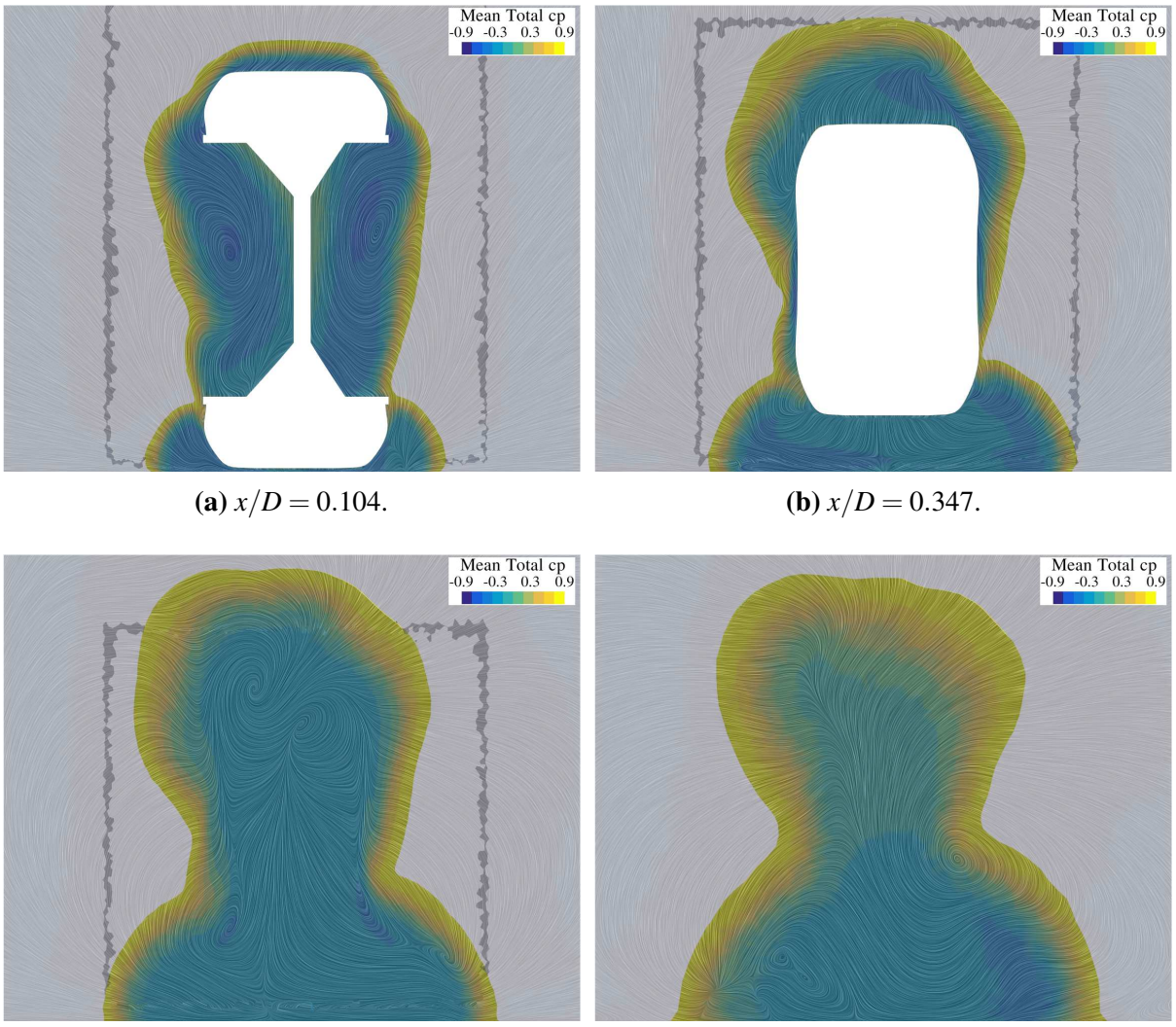

(a) $x/D = 0.104$. **(b)** $x/D = 0.347$.

(c) $x/D = 0.518$. **(d)** $x/D = 0.867$.

Figure 4.10: Total pressure coefficient contour with velocity line integral convolution vectors at different transversal slices (see figure 4.4) on the rear part and near wake of the solid wheel from time-averaged URANS simulation. Jetting phenomena, recirculation bubble and vortices at the hub cavity are oberseved at first stage. Then, recirculation bubble is enlarged and merged with hub vortices to finally dissapear while a pair of counter-rotating vortices remain in the lower region at the far wake.

Results obtained from URANS simulation show a great improvement from steady simulation and a close agreement to experimental data and previously mentioned related literature.

At first slice (a), a more uniform flow can be observed with two more stable vortices located

at both sides of the hub. Recirculation bubble on the top tyre reaches a slightly higher position and the transition and interaction with vortex structure at the hub is smoother and really similar to the one obtained by Fackrell. Jetting phenomena is narrower at this point, effect also discovered and analysed by McManus among steady and unsteady simulations [11]. Fackrell also observed this efffect and was unable to find a justified reason. Possitive pressure peak on the rotating wheel was expected to increase the velocity of the flow expelled from the frontal contact patch and hence obtain a larger separation region. It was supposed but not observed that the boundary layer in front of the stationary wheel was separating and rolling up to form a horseshoe vortex around the wheel. McManus did not observe such a feature and propose and alternative reasoning based on the difference of the oncoming flow conditions. The flow is deflected by low velocity boundary layer found at stationary wheel while in the rotating case the flow is deflected with the freestream velocity in absence of mentioned thick boundary layer. Thus, the separation region is less deflected in stationary case and is greater enlarged compared to rotating case.

At second slice (b) an even higher recirculation bubble can be noticed. As a result, transition with the vortex coming from the hub is still smooth and in great agreement with Fackrell experimental data. Then, the flow structured is gradually minimised towards the lower region. Jetting phenomena is still observed and enlarged compared to previous section. It can be seen how the flow is energised by expanding flow coming from the rear contact patch.

Two similar views are obtained from the furthest slices. A counter-rotating vortex pair is observed at slice (c) that is vanished at slice (d). The wake is still in transition from near wake to far wake where just two counter-rotating vortices remain on lower region.

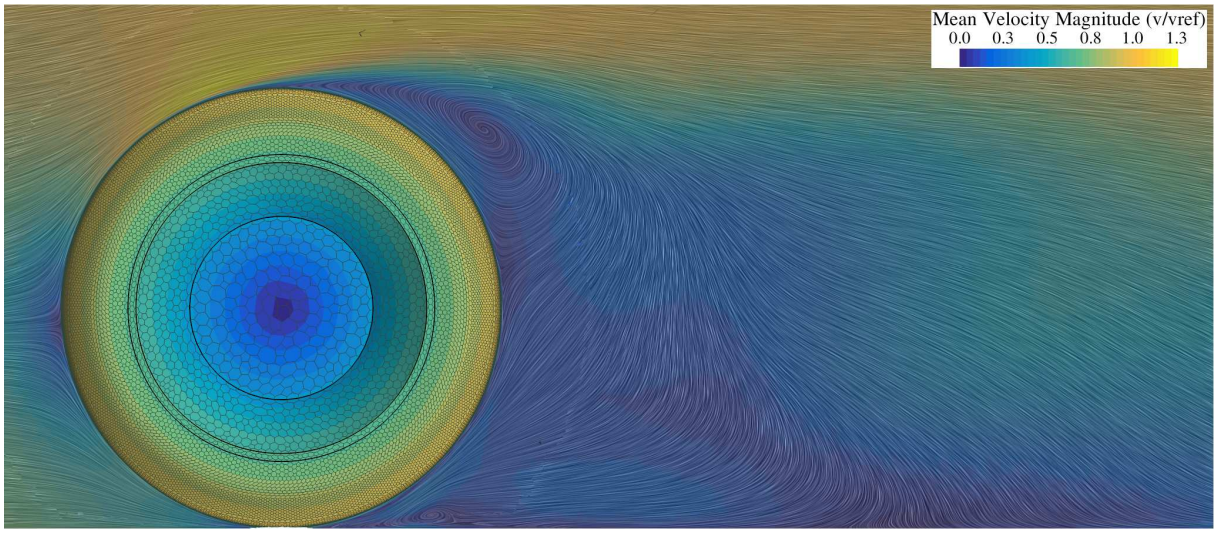

Figure 4.11: Non-dimensional velocity magnitude contour at central longitudinal plane with velocity line integral convolution vectors of the solid wheel from time-averaged URANS simulation. Recirculation vortex on the top wheel is attached to the surface and smaller vortex is found over the ground next to the rear contact patch.

In order to complement the information from transversal slices, time-averaged non-dimensional

velocity magnitude is shown in figure 4.11 for longitudinal central plane. Slightly different figure is obtained compared to 4.6 due to software limitations. Due to mapping procedure carried for averaging the solution on a rotating reference frame as explained in detail in previous chapter, two different variables are obtained for the mean velocity at both domains. Hence, two different sets of streamlines should be added and it is not possible to be connected. Then, line integral convolution vectors are highlighted in this figure to observed flow behaviour of the velocity profile and mesh grid is hidden no to disturb the image. Plus, it can be seen how the mapping procedure is successful and transition between the domains is quite smooth regarding mentioned limitation.

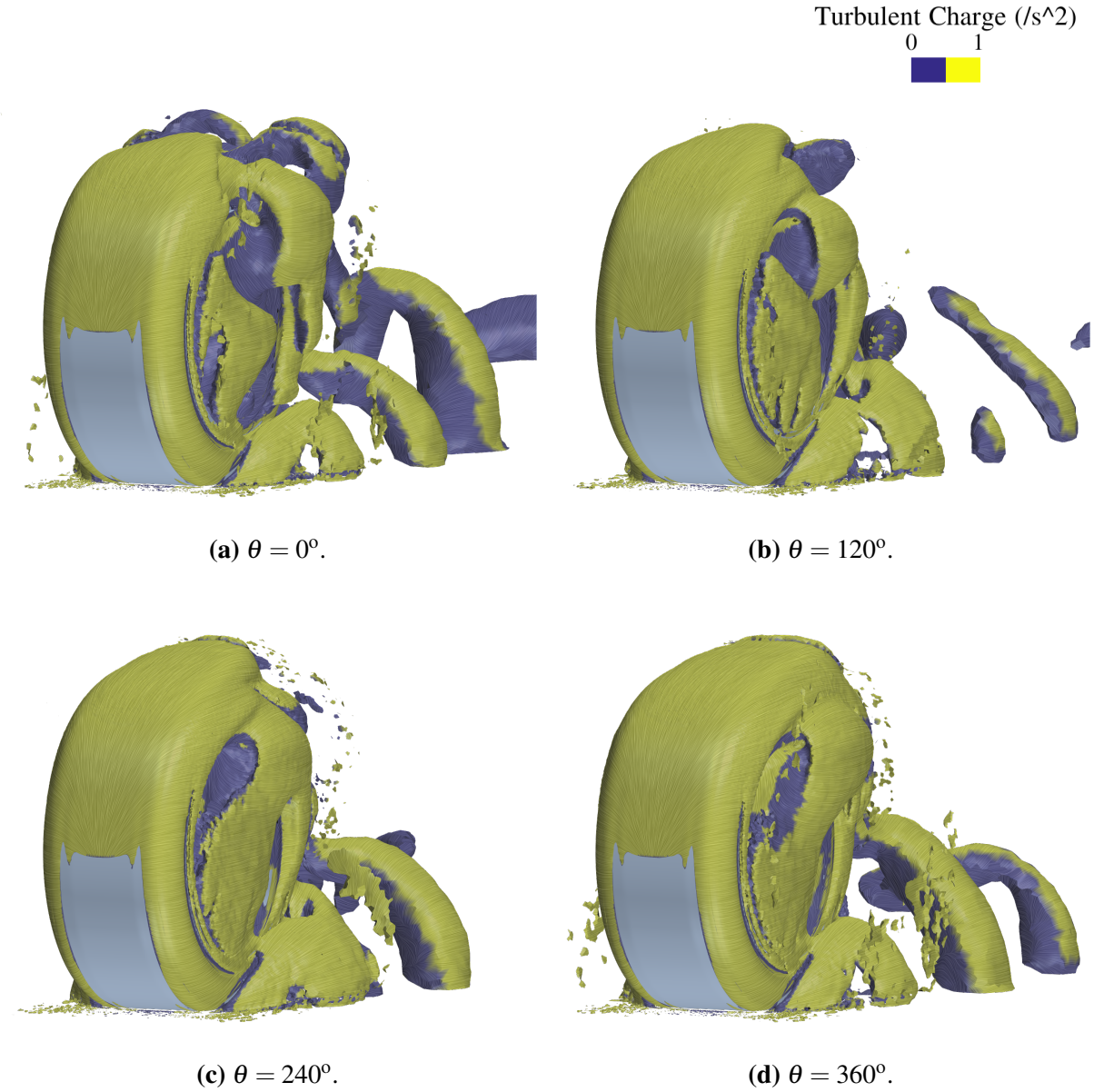

(a) $\theta = 0^{o}$.

(b) $\theta = 120^{o}$.

(c) $\theta = 240^{o}$.

(d) $\theta = 360^{o}$.

Figure 4.12: Front view of isosurface of Q criterion (4000 s^{-2}) with velocity line integral convolution vectors and turbulent charge contour of the solid wheel from time-averaged URANS simulation. Jetting phenomena and rim vortices evolution in time is captured.

Main features to be mentioned are vortex generation and location. The separation point is remained in the same position on the top of the tyre but the recirculation zone is varied. The vortex on the top region is closer to the wheel and the recirculation is completely attached as opposed to steady state. It can be observed how the flow separation is produced the way Fackrell expected. The flow coming out the vortex follows the wheel motion over the surface and separation is produced over a thin layer that keeps attached to the surface.

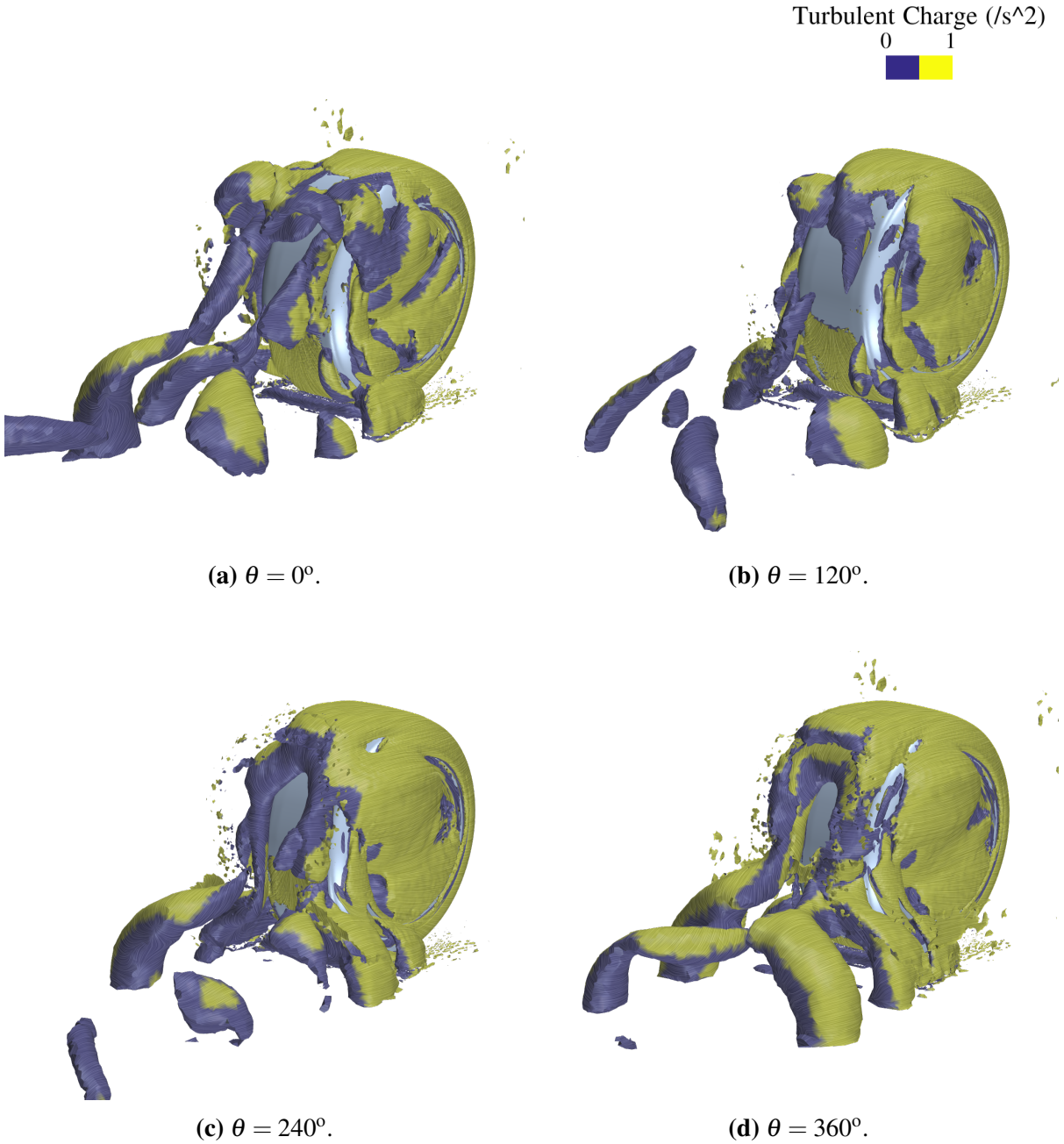

(a) $\theta = 0^{o}$.

(b) $\theta = 120^{o}$.

(c) $\theta = 240^{o}$.

(d) $\theta = 360^{o}$.

Figure 4.13: Rear view of isosurface of Q criterion (4000 s^{-2}) with velocity line integral convolution vectors and turbulent charge contour of the solid wheel from time-averaged URANS simulation. Recirculation bubble and near wake plus jetting phenomena and rim vortices evolution in time is captured. Surprising transversal vortex on the rear contacth is found.

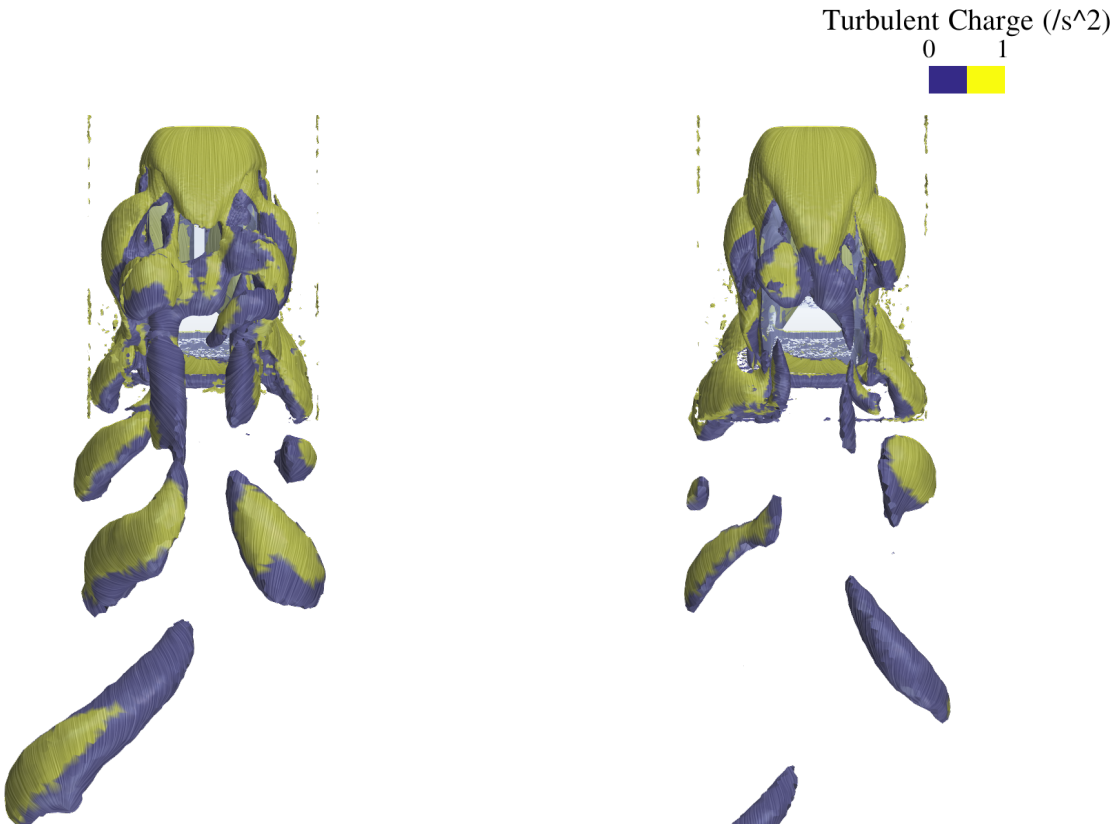

(a) $\theta = 0^{o}$.

(b) $\theta = 120^{o}$.

(c) $\theta = 240^{o}$.

(d) $\theta = 360^{o}$.

Figure 4.14: Top view of isosurface of Q criterion (4000 s^{-2}) with velocity line integral convolution vectors and turbulent charge contour of the solid wheel from time-averaged URANS simulation. Far wake evolution in time is captured.

On the lower rear part an important variation is noticed. No vortex is located on the wheel surface but near the contact patch over the ground. The flow is clearly suctioned and directed outwards following ground and wheel motion. In the scenario, the flow redirected towards the ground experiences a small vortex due to strong variations on velocity direction.

High unsteadiness is expected in the wake of a rotating wheel and it can be better captured by URANS than steady RANS. Still, LES or DES kind of solver would be preferable for a better prediction and flow features capturing. Isosurfaces are again shown to study the vortices captured by the simulation. However, different time steps are represented instead of a time-averaged solution already shown in previous figures 4.10 and 4.11 to understand the unsteady behaviour. Established the first frame as initial rotation stage ($\theta = 0^o$), three following solutions distanced by a turn of 120^o are shown.

Flow visualisation from front view in figure 4.12 shows a good picture of jetting phenomena and rim vortices. Jetting phenomena is clearly captured. Deflection of the flow expelled from frontal contact patch is quite stable, while the jet is periodically interrupted and arch-shaped vortex are propagated downstream. Unsteadiness at upper rim vortex is also noticed, however it can be appreciated how the flow is more attached to the wheel comparing to steady state.

Rear view in figure 4.13 shows a better scope of recirculation bubble and near wake and another point of view for jetting phenomena and rim vortices. Analysing the representation from top to bottom, unsteadiness of recirculation bubble can be clearly seen. It is energised and enlarged as time is advanced and it is collapsed at some point to start over again. It is closely related to the vortices coming out the top rim. The flow coming from the top and both sides is merged periodically right after the wheel and an arch-shaped vortex is found attached to the tyre surface. Width and height of given feature is maintained compared to wheel dimensions. High vorticity region is observed inside the rim cavity but it is stuck due to forces related to wheel rotation.

Arch-shaped vortex on top is extended downwards with a periodic deflection, switching between a vertical vortex extension attached to the wheel and 45^o deflection streamwise. It is also coupled with the flow coming from the frontal contact patch jet. It can be observed how arch-shaped vortex is created on the lower part between both projected flows. Then, the flow is extended downstream on the lower region.

Special attention is brought to the vortex generated next to the rear contact patch. It can be observed how it is developed uniformly and constantly along the tyre width at the location inferred from velocity contour in figure 4.11. It is an interesting feature not captured before in consulted literature. It is one of the main differences with McManus [11] results, that expect a vortex in a higher position as the one captured in steady simulation in figure 4.6. It is reasonable that overset approach and near contact modelling enables capturing this feature. The expected but not usually captured suction peak on the rear contact patch attracts vortex generation closer

to contact. It is a difficult area to be accessed for experimental studies and impossible to be properly captured if a step or a gap is modelled as usually found in literature. In addition, real rotation generated with the overset approach reinforces this effect.

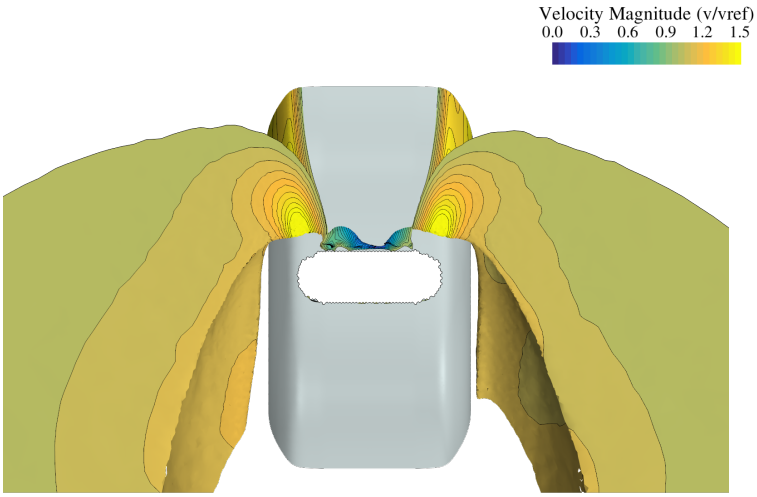

Figure 4.15: Time-averaged isosurface of total pressure coefficient (0.9) at the contact patch with non-dimmensional velocity magnitude contour of the solid wheel from time-averaged URANS simulation. Uniform jet is captured, narrower than the one obtained with steady RANS.

Finally, far wake is studied with figure 4.14. Further wake is captured with URANS compared to steady RANS as it could be expected. Intercalated half arch-shaped vortices are extended downstream from jetting flow and the flow directed downwards from the recirculation bubble. The width of the wake is maintained until great distance is achieved around 3-4 wheels behind.

Time-averaged isosurface of 0.9 total pressure coefficient is shown in figure 4.15 at the contact patch from a bottom view. It is notices that this feature is quite steady on time, thus an averaged representation is shown. A clear stagnation area is observed at frontal contact patch, where high pressure peak is experienced due to sudden obstacle faced by the flow. Then, a sudden expansion is experienced at both sides of the contact patch and the flow is directed downstream with a lower velocity than freestream jet as observed in previous figures. A narrower jet is observed compared to steady RANS results regarding the reasoning explained above.

4.2 FEA

Solution from Finite Element Analysis (FEA) simulations with ABAQUS are presented bellow for both linear elastic and hyperelastic models explained in previous chapter. As no experimental or numerical data is available for employed wheel geometry regarding to tyre deformation, a rigorous validation process as the one carried with CFD simulations is not feasible. Instead, qualitative comparison is made with other studies in different conditions to ensure a configuration and solution as realistic as possible. Hence, main scope of this section is to prove that a valid deformation and contact patch is achieved in order to perform CFD simulations over it.

4.2.1 Linear elastic

First, a simplified case with a unique and uniform material with linear elastic behaviour for tyre modelling is computed. From initial undeformed shape with no existing contact with the ground to final converged solution with fully deformed tyre by ground compression, six increment states are taken with another six iterations within each step.

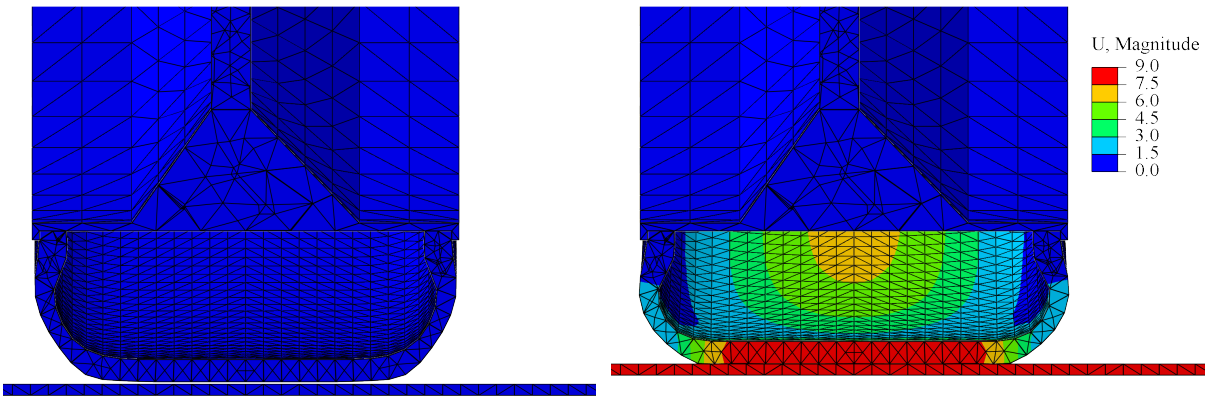

(a) Initial step. **(b)** Final step.

Figure 4.16: Initial and final deformation step at central yz plane for linear elastic model. The rim is fixed while the tyre is compressed by the moving ground. Gradually incremented displacement magnitude in the tyre between the tread and the consntraint with the rim.

Nodal displacement magnitude at central cross section cutting plane is shown in figure 4.16. The rim is totally fixed while the ground is displaced 9 mm upwards to model the compression between the tyre and the ground due to the vehicle's weight. The tyre is in contact with the ground and deformed uniformly. It can be appreciated how the displacement value, maximum and equal to the ground displacement at the tread, is reduced gradually until the contact with the rim. Uniform displacement is seen as well far from the contact patch, where most of the deformation is concentrated in the central tread and smoothly dispersed to the side tyre.

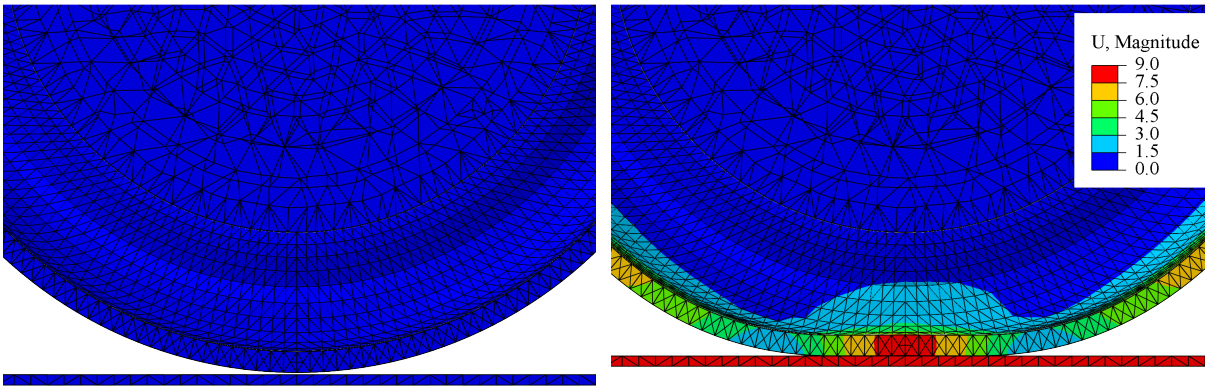

(a) Initial step. **(b)** Final step.

Figure 4.17: Initial and final deformation step at central xy plane for linear elastic model. The rim is fixed while the tyre is compressed by the moving ground. Longitudinal tyre contact with the ground is checked.

From longitudinal central cutting in figure 4.17, a good picture of how the tyre is deformed and adapted to the ground is shown. As it will be further discussed, contact area looks reasonable for a usual tyre deformation and element faces from the tyre and the ground are successfully aligned.

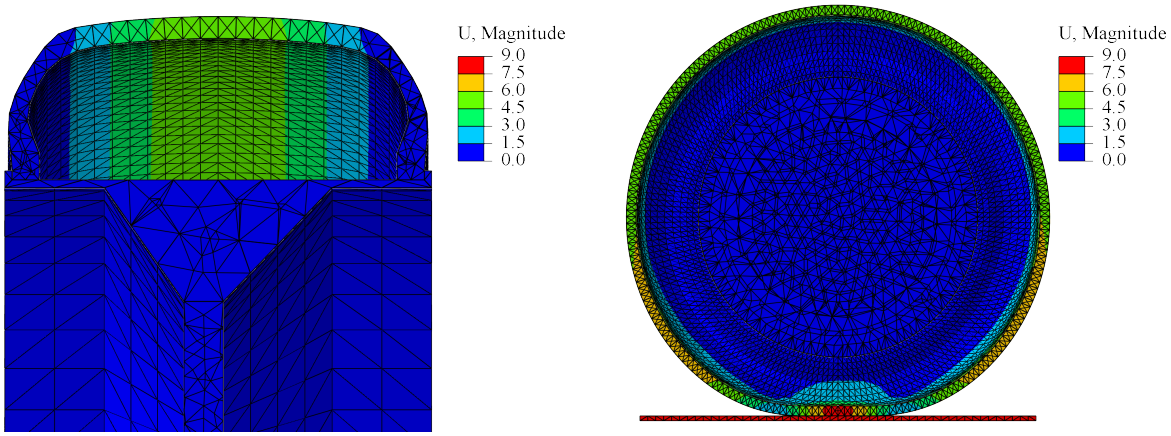

Figure 4.18: Deformation at top and overall wheel central yz and xy plane for linear elastic model. Excessive reactive deformation is observed on the top of the wheel.

In addition to previous figures, another cross section view of the top part of the tyre and an overall picture of longitudinal section are shown in figure 4.18 to better understand the deformation distribution along the tyre. After the maximum displacement point at the contact patch, a progressive decreasing displacement is experienced in the surroundings. Then, due to the inner pressure and the compression at the contact patch, the rest of the central tread area experiences a reactive displacement around the wheel. A strong displacement is still suffered on the lower tyre section while half of the maximum displacement is found along the upper part. As it can be checked in the cross section, far from the contact patch the displacement is zero on the lateral

part of the tyre and all the deformation is concentrated on the central tread.

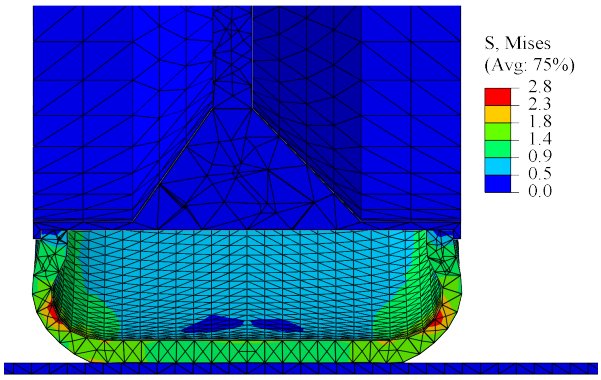

Figure 4.19: Von Mises stress at final deformed step at central yz plane for linear elastic model. Maximum stress located at narrower tyre section on sidewalls.

It is not a realistic behaviour as a wheel is designed to be resistant on the tread side and more flexible on the lateral part. If a higher load is transferred to the wheel through the ground compression or inner pressure, the deformation on the central tread is highly increased and non-realistic shape is obtained.

Apart from displacement study over the wheel, a brief stress analysis can be inferred from figure 4.19. As it could be expected, maximum Von Mises stress is located at the point where the smaller section is found and stress concentration is experienced. Still, the values are quite low and equally distributed along the rest of the section.

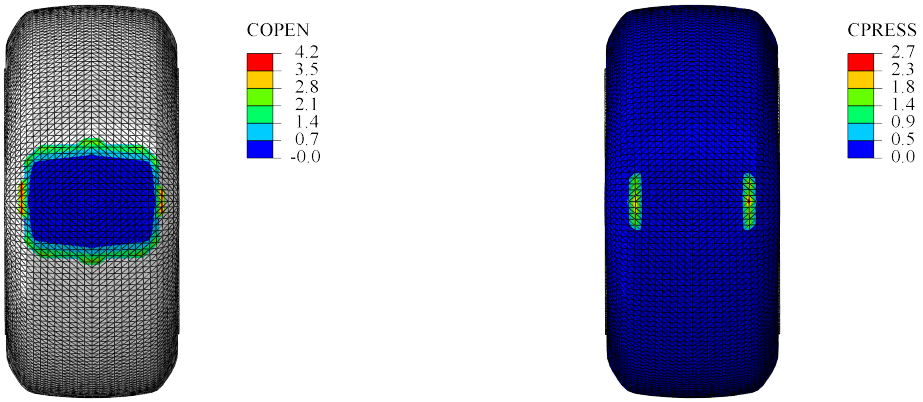

Figure 4.20: COPEN and CPRESS representation at contact patch for linear elastic model. Realistic contact patch area is obtained although unrealistic contact pressure distribution is achieved.

Finally, special attention is paid to the contact patch. On the left hand side of figure 4.20, contact opening (*COPEN*) value is represented. It represents the distance between the slave (tyre) and master (ground) surfaces predefined to be in contact. Then, contact area can be clearly highlighted and overclosure can also be identified where negative values are found. A

similar area is obtained to the one in Yang's PhD thesis [5] from where reference data is taken. Little overclosure may have been committed but it is not significant as observed in the results.

On the right hand side, contact pressure (*CPRESS*) value is represented. In contrast to *COPEN* contour results, *CPRESS* is in disagreement with what was expected. The load is not uniformly transferred from the ground to the tyre and it is concentrated on the lateral contact parts.

4.2.2 Hyperelastic

More realistic multi-material tyre with hyperelastic behaviour is then simulated in pursuit of higher reliability on results. Simulation is run in homologous conditions as linear elastic case, being needed six increment states as well with five to six iterations within each step to reach a converged solution.

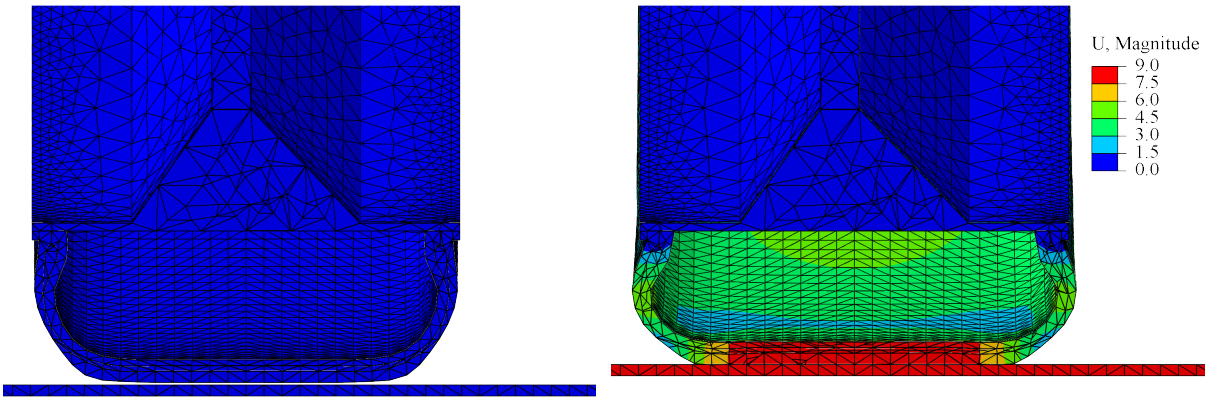

(a) Initial step. **(b)** Final step.

Figure 4.21: Initial and final deformation step at central yz plane for hyperelastic model. The rim is fixed while the tyre is compressed by the moving ground. Well distribiuted intermediate displacement magnitude in the tyre between the tread and the consntraint with the rim.

Same results are shown for hyperelastic solution in order to carry a consistent analysis and further comparison between the models. Displacement magnitude is represented at central cross section at initial and final step in figure 4.21. Maximum and minimum displacement are clearly differentiated. On on side, the rim and the joint with the rim are completely constrained, while the maximum displacement is found at the moving ground and the central tread in contact with it. Then, the rest of the tread, sidewalls and other tyre parts experience an intermediate displacement quite well distributed with sudden transitions.

Longitudinal section is shown in figure 4.22 at initial and final step. Contact is successfully achieved although a shorter interval is interacting. As observed in previous figure, displacement is adapted quickly with sharp transitions and a balanced distribution.

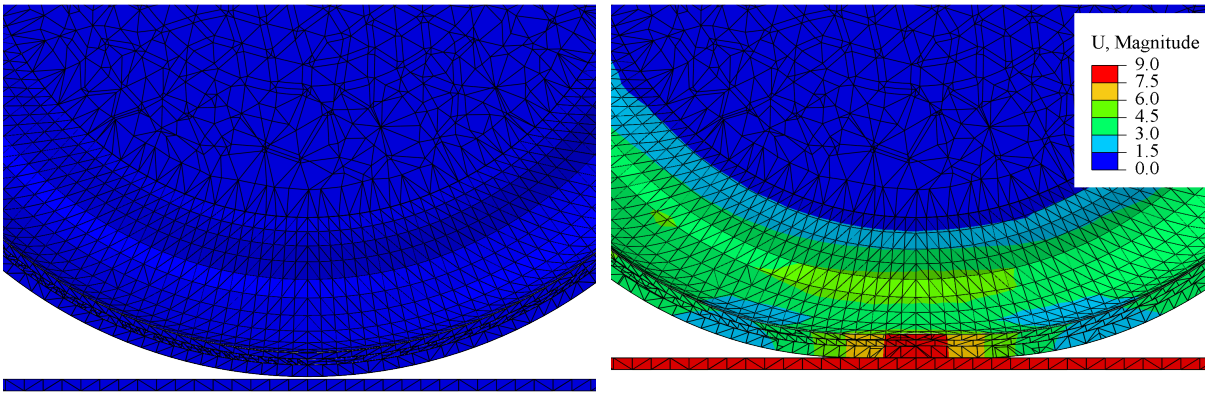

(a) Initial step. **(b)** Final step.

Figure 4.22: Initial and final deformation step at central xy plane for hyperelastic model. The rim is fixed while the tyre is compressed by the moving ground. Longitudinal tyre contact with the ground is checked.

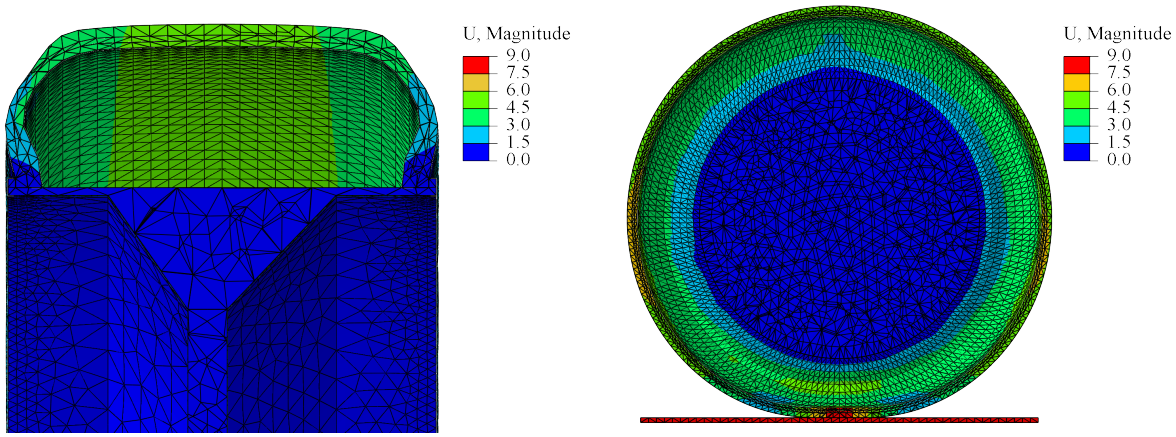

Figure 4.23: Deformation at top and overall wheel central yz and xy plane for hyperelastic model. Well distribiuted deformation observed overall leading to a more realistic shape.

Previous analysis is supported by figure 4.23. Displacement on the upper tyre and overall longitudinal section are shown. Reactions due to the loads applied on the wheel are better absorbed and distributed along the wheel, with an intermediate value for most of the wheel. No high displacement concentration is found and consequently a more realistic shape is maintained.

One of the greatest differences between studied models can be found in figure 4.24. Von Mises stress is represented in cross section cut and satisfying results are obtained. Instead of a low distributed stress field as previously observed, higher stress is observed concentrated all at the undertread. It is demonstrated that the aim of this functional part is fulfilled and it is acting as a reinforcement to support the stress and add a necessary rigidity to the wheel structure. That is the reason why the obtained tyre deformation is more homogeneous and a more realistic shape is achieved.

Finally, contact opening and pressure are shown in figure 4.25. Again, a uniform contact area

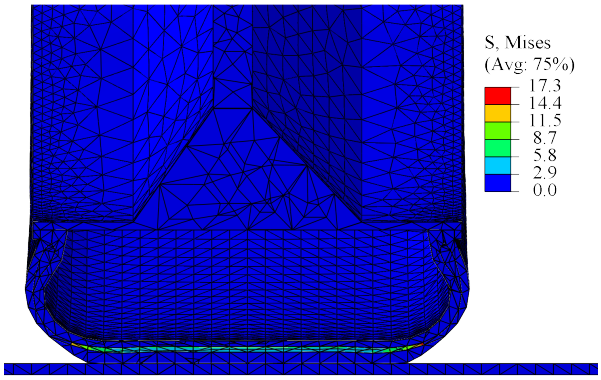

Figure 4.24: Von Mises stress at final deformed step at central yz plane for hyperelastic model. Maximum stress located at the undertread, bearing most of tyre stress and maintaining a realistic shape.

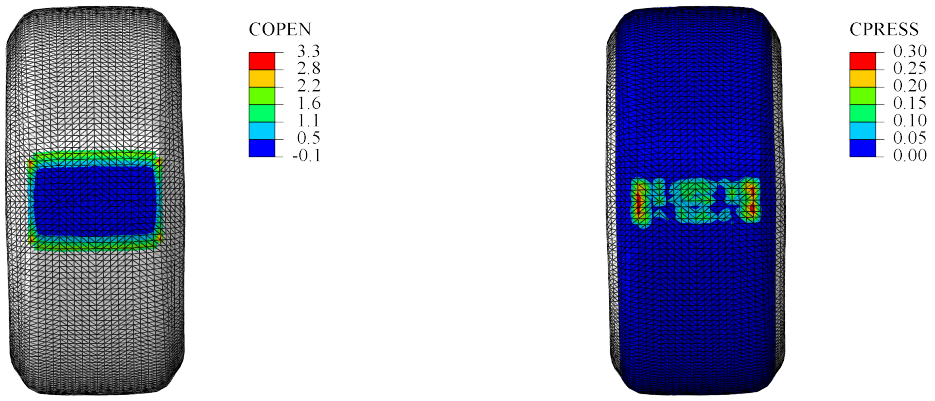

Figure 4.25: COPEN and CPRESS representation at contact patch for hyperelastic model. Realistic contact patch area is obtained with fair contact pressure distribution with high concentration at both lateral sides.

is displayed at *COPEN* representation, suggesting that the contact is achieved with a slightly smaller surface than the one obtained with linear elastic but still valid compared to previous studies. Small overclosure is inferred because of negative values detected in *COPEN* representation, although it can be considered negligible for thesis purpose as final deformed geometry is satisfactory. Indeed, it can be observed on the right hand side how contact pressure results are in good agreement with the ones observed in Yang's thesis [5]. Maximum contact pressure is found at the lateral sides of the contact patch while intermediate pressure is found around the central contact zone. It is still not ideal due to overclosure uncertainty but results are overall quite similar to the ones obtained in reference studies.

4.2.3 Comparison and discussion

Both linear elastic and hyperelastic models are simulated with successful results and remarkable differences between them. It is demonstrated that hyperelastic and specially multi-material model for the tyre is advantageous upon linear elastic. Undertread region modelled as a high rigidity material in order to emulate the effect of a composite reinforcement leads to high fidelity results. Despite the lack of reference data and the aim of reproduce a simplified model capable to generate realistic deformations for CFD simulations, results are quite promising. Hypothesis and simplifications assumed are verified and the model is considered valid.

Expected limitations from linear elastic model are observed when experiencing high deformations. Still, differences with hyperelastic model are not that big. Simplified representation of external boundaries at both cross and longitudinal sections is shown in figure 4.26 for non deformed, linear elastic and hyperelastic models. The ground is fixed at zero in contrast to the simulation in order to offer a more intuitive representation.

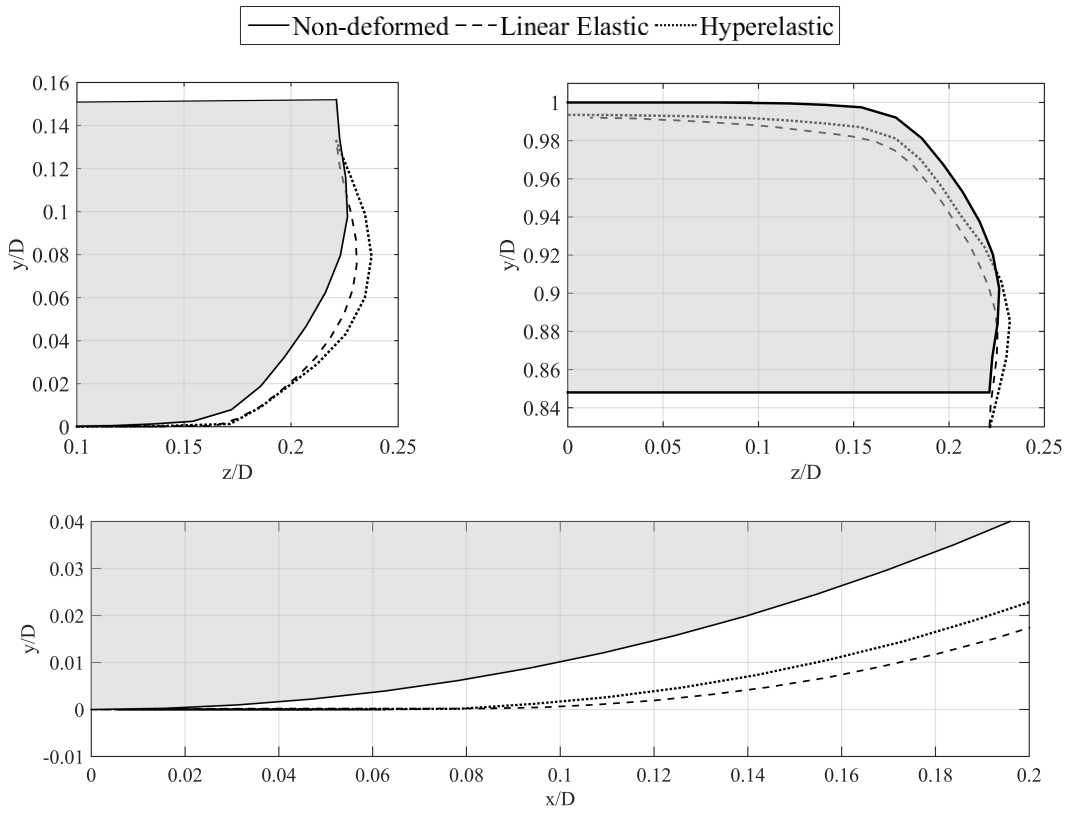

Figure 4.26: Deformation comparison between solid, and deformed wheel with linear elastic and hyperelastic models. A greater contact patch is achieved with linear elastic model although an exagerated deformation is obtained as a reaction on the rest of the tyre. Overall shape is better maintained with hyperelastic model.

Cross section is shown in the upper part of the figure for bottom and top tyre zones. Both models show a similar deformation at the contact patch. It is on the sidewall where main differences

are found. Due to different material properties and higher elasticity, bigger expansion can be noticed on the sidewall of hyperelastic model. Moreover, on the top part of the tyre it can be observed how a more similar shape is maintained with hyperelastic model. Linear elastic model tends to be overexpanded at the central line but still keeps a fair geometry. Even though the tyre is expanded due to the compression at the contact patch, the displacement committed at the contact patch is higher and the total height of the wheel is decreased after the weight load is applied.

In agreement with the behaviour experienced on the cross section, overexpansion at the central line is observed at the linear elastic model in comparison to hyperelastic. Contact patch is also observed to be slightly more extended on the linear elastic model.

All in all, hyperelastic model is proved to provide higher fidelity results although linear elastic could also be employed under some limitations and uncertainties. However, it is also important to bear in mind the computational cost linked to each simulation (see table 4.3). While linear elastic simulation is carried in a personal computer within 3 minutes, 30 minutes are required for running hyperelastic case.

Model	CPUs	Elapsed time (min)
Linear elastic	4	3
Hyperelastic	4	30

Table 4.3: Computational cost of FEA simulation for linear elastic and hyperelastic tyre models.

There is no doubt that it is an affordable computational budget for a single simulation. That is the reason why the hyperelastic model is the one chosen to carry the CFD simulation over a deformed wheel. However, if coupled FSI simulation is carried in the future and wheel deformation needs to be updated every time step, computational cost in such an expensive simulation would be ten times higher compared to linear elastic. Hence, a more efficient model should be employed in order to achieve a feasible configuration.

4.3 CFD for deformed wheel

Once CFD and FEA simulations are run and results are validated, the aim of setting a coupled FSI simulation can be overcome. Both cases have been successfully set with steady and unsteady rotating conditions, thus the following issue is how to set the connection between the two different solvers and achieve a robust data interaction and mesh update.

As a preliminary step, decoupled CFD simulation is set with the deformed wheel obtained from ABAQUS being exported into STAR-CCM+.

4.3.1 Steady RANS and URANS

Steady RANS is set at first place with the deformed wheel. Mesh generation procedure is thoroughly adapted from previous mesh with non-deformed wheel to the new geometry, being respected all size and distribution parameters. After the surface is cleaned and good connectivity is ensured at the contact patch, the new case is ready for being run.

Afterwards, URANS simulation is carried from converged steady solution and data is time-averaged following the same strategy as with solid wheel. In order to be concise since the results may look repetitive and comparison is tougher to be done, both steady and unsteady results are exposed together and compared to solid wheel to show a better analysis of the differences among them.

Aerodynamic forces

First magnitude to be analysed is again the aerodynamic forces. Drag and lift coefficients are shown in table 4.4 for RANS ans URANS results. Fackrell experimental results are also included for reference purpose although the test conditions are not equivalent anymore.

	CD Tyre	Relative error	CL Tyre	Relative error
Fackrell	**0.51**	-	**0.28**	-
RANS	0.48	5.9%	0.28	0%
URANS	0.51	0%	0.33	17.9%

Table 4.4: Drag and lift coefficient based on frontal area obtained from steady and unsteady RANS simulation for deformed wheel. Relative error is shown upon experimental reference data from Fackrell [2]. Good agreement in lift is obtained with deformed wheel and similar drag force.

Drag coefficient is still quite insensitive upon any variation in geometry or solver tested. However, a surprising lift variation is experienced after deformation is applied. The same value as

the one obtained by Fackrell is obtained with RANS and 17.9% higher with URANS, meaning a great difference with respect to solid wheel study.

Still a further analysis needs to be done with more descriptive variables, it clearly shows the influence of the contact patch modelling on lift prediction.

Pressure coefficient distribution

Pressure coefficient distribution along the centre line is shown in figure 4.27. Overall behaviour is similar to the one observed with solid wheel, indicating that the results are consistent and re-meshing procedure is overcome with no major incidence.

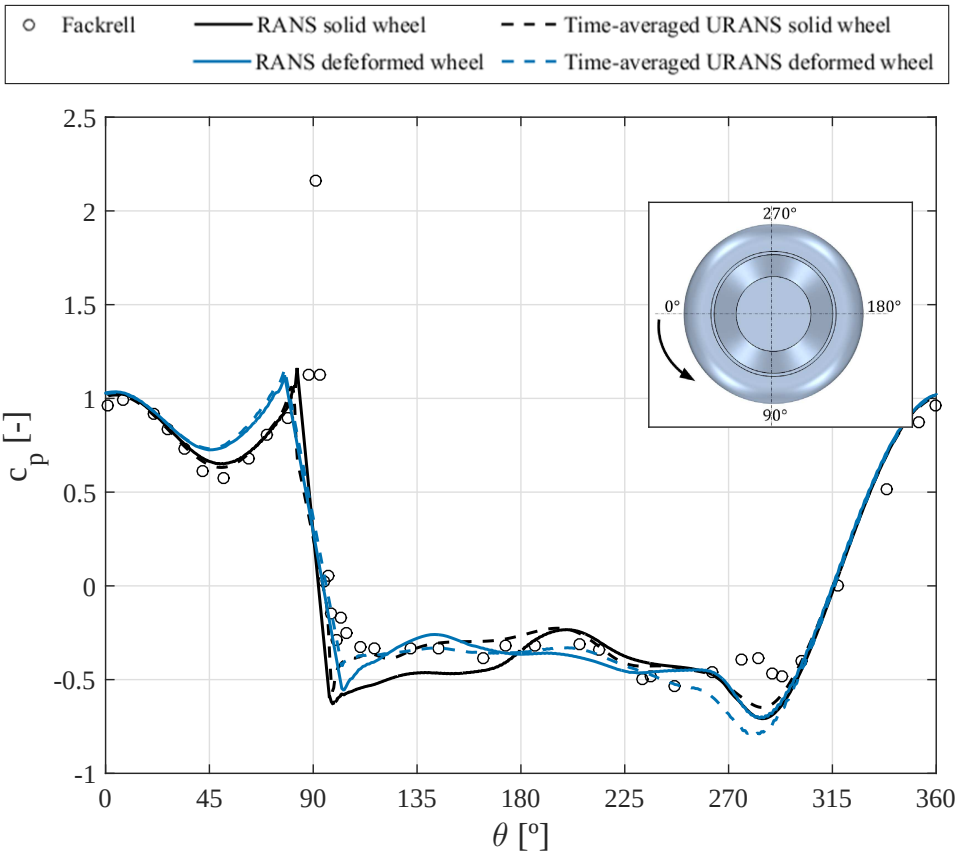

Figure 4.27: Static pressure coefficient distribution over the central line of the solid and deformed wheel with hyperelastic and multi-material model from steady RANS and time-averaged URANS. Experimental data from Fackrell's experiment [2] for solid wheel is also included. Suction peak at $\theta = 45^o$ is weaker and the separation point on the top part is predicted downstream compared to solid wheel. Difference between steady RANS and time-averaged URANS is minimum, mainly on the rear part of the wheel where a high turbulent flow is found. The minimum pressure point near the top part is predicted stronger with mean URANS over deformed wheel.

Between the central front position and contact patch ($\theta = 0^o - 90^o$) a weaker and sooner suction peak is observed with respect to solid geometry for both steady and unsteady simulations. Wheel deformation clearly provokes an earlier flow acceleration due to change in surface cur-

vature. At the same time, less surface is available to keep accelerating and the suction peak is not that strong. Afterwards, all distributions experience a similar tendency to a pressure peak at the contact patch.

As mentioned before, the mesh around the contact patch is cut by zero gap overset interface and no data is obtained from the closest cells to the contact. From figure 4.27, a gap of 24.8^{o} with no data is obtained around the contact. It should be highlighted that, due to tyre deformation, the contact between the tyre and the ground is not a line any more but a tiny surface with elliptical shape as observed in figure 4.25. The new contact patch encloses an area corresponding to 18.8^{o} in the center line, thus just a region corresponding to 3^{o} is not being captured at each side.

A similar reverse behaviour is experienced right after the contact patch. Suction peak is again weaker than the one predicted for the solid wheel. The fact that the edge at the intersection is not as sharp provokes a smoother transition that is clearly affecting the aerodynamic forces. Actually, pressure distribution obtained from URANS fairly fits experimental data at the rear contact zone.

Transition zone from contact patch up to the top of the while is quite confusing and varying among the different simulations. Comparing steady state solid and deformed wheel simulations, a wider pressure range is observed with more noticeable suction and pressure peaks. Distribution is similar but the pressure peak is found closer to the contact patch in the deformed wheel case. Regarding to unsteady simulations, both present a smoother distribution closer to the one expected from experimental data. A lower pressure level is maintained in the deformed wheel, meaning that the flow is more accelerated over the surface.

Then, the separation point is found near the top part of the tread. In this case, the sudden pressure decrease indicating the separation point is found even slightly earlier than the top part, at around $\theta = 265^{o}$. While both steady simulations present an identical distribution in the last quadrant ($\theta = 270^{o} - 360^{o}$), a greater suction peak is found for unsteady deformed wheel case. Difference here may be due to the different boundary conditions imposed at both unsteady simulations. However, as both geometry and boundary conditions are vary, it is difficult to reach a solid conclusion.

Wake analysis

Maintaining the comparative scope of present section, previously studied variables for wake analysis are presented in a more representative way to be easily compared. In figure 4.28, 0.9 total pressure coefficient isoline is represented at standard transversal slices over the rear part of the wheel and the near wake. Differences between steady and unsteady simulations within deformed wheel are firstly analised at each section to later identify the difference with solid wheel simulations.

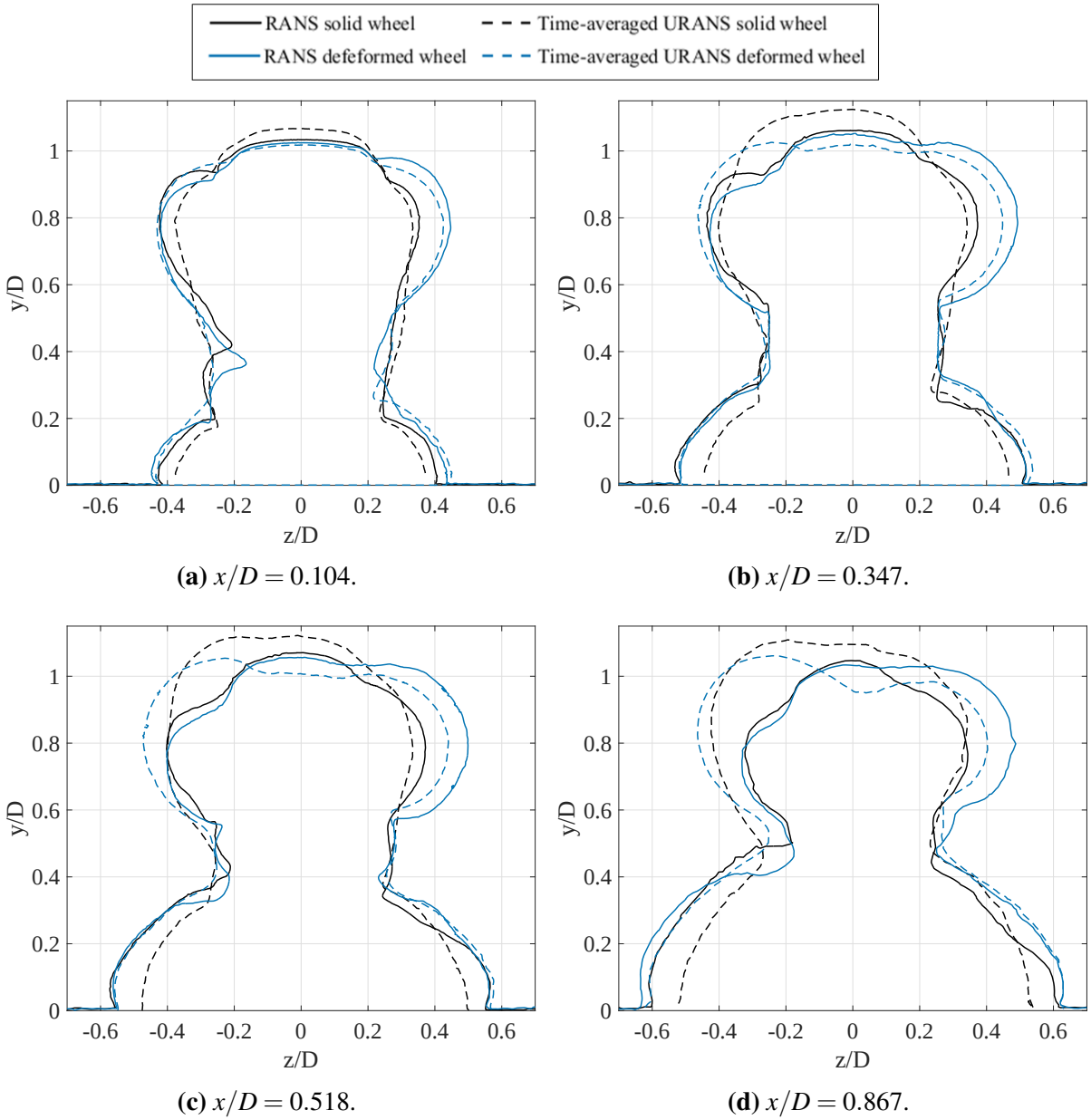

(a) $x/D = 0.104$. **(b)** $x/D = 0.347$.

(c) $x/D = 0.518$. **(d)** $x/D = 0.867$.

Figure 4.28: Total pressure coefficient isoline (0.9) at different transversal slices of the solid and deformed wheel from RANS and time-averaged URANS simulations. Wider jetting phenomena and upper vortices are observed in deformed wheel while taller recirculation bubble is observed in solid wheel.

At first slice (a), main discrepancies between steady and unsteady simulations are found at intermediate vortex structures. Overall, time averaged-transient simulation sows a more uniform distribution, with a smoother transition between jetting phenomena and upper vortices. Jetting phenomena and recirculation bubble are similarly captured at this point. Compared to solid wheel, more variations are found. Jetting phenomena and upper vortices are wider in the deformed case, leading to a shorter recirculation bubble.

At second slice (b), remarkable variations are found on the upper wake. Again, mean URANS is

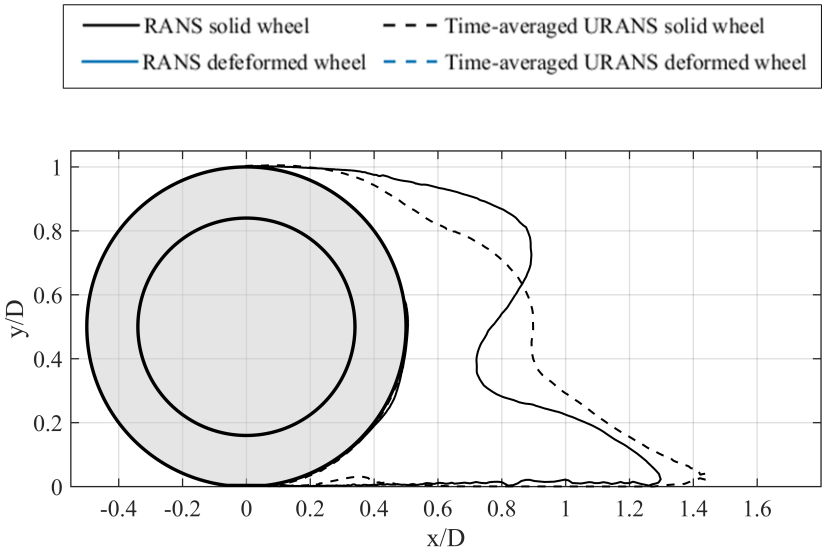

(a) Solid wheel.

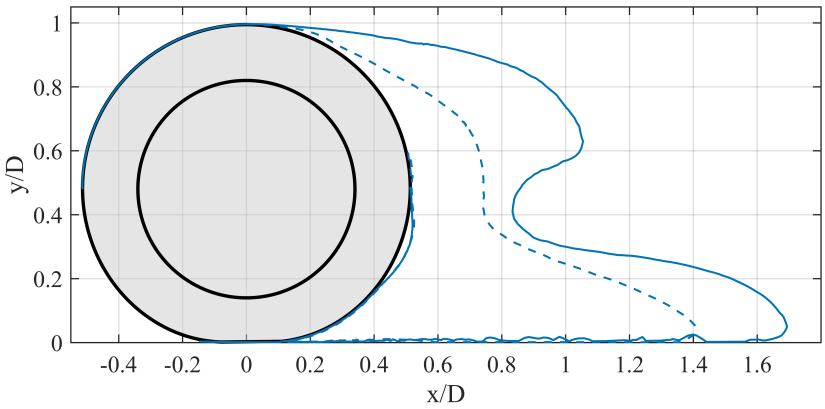

(b) Deformed wheel.

Figure 4.29: Velocity profile with zero longitudinal velocity isoline at central plane of the solid and deformed wheel from RANS and time-averaged URANS simulations. Longer wake is observed for steady deformed case while a more attached flow is observed for time-averaged URANS deformed case.

more uniform than steady simulation where a great asymmetry is found. While steady state simulations are more similar to each other and present more diffusive solutions. Greater difference is found between unsteady simulations. Jetting phenomena is clearly narrower in unsteady solid case. Therefore, smoother transition is experienced up to the top of the wheel and a narrower upper vortex pair is predicted, finishing with a taller recirculation bubble. Strongest suction peak predicted by URANS deformed case right before the separation point on the top surface is leading to a more attached wake.

At slices (c) and (d) the effects and differences previously explained are extended downstream.

In order to compare the velocity profile streamwise, zero longitudinal velocity isoline is shown at central plane in figure 4.29 for both RANS and URANS solution with solid and deformed

wheel. Near wake shape can be seen and compared between obtained solutions.

Velocity profile analysis over solid wheel has been previously made. Regarding deformed wheel, it can be identified the upper wake after the separation point and a longer lower wake above the ground. Recirculation is captured by both solver configurations at the same location on the rear tyre surface. Difference between steady and time-averaged unsteady solution is observed in the wake profile. The flow remains more attached to the tyre surface with URANS and the whole wake is affected downstream, closer to the wheel.

When comparing both wheel models, slightly later separation can be seen. Near wake captured with steady state is longer for deformed case as observed by Pruvis [23]. However, that difference is not observed in time-averaged unsteady state.

Finally, vortex structure analysis is supported by isosurface representations as previously shown, comparing steady and averaged unsteady solutions.

From a frontal point of view in figure 4.30, jetting phenomena can be observed from both solutions. A continuous and further expanded jet is captured with URANS compared to RANS. However, previous pressure results show a similar distribution at this point for both configurations. Therefore, it seems that it is more related to averaging and visualising limitations of RANS model rather than flow miss prediction. Both upper vortices are indeed as wide as previously predicted.

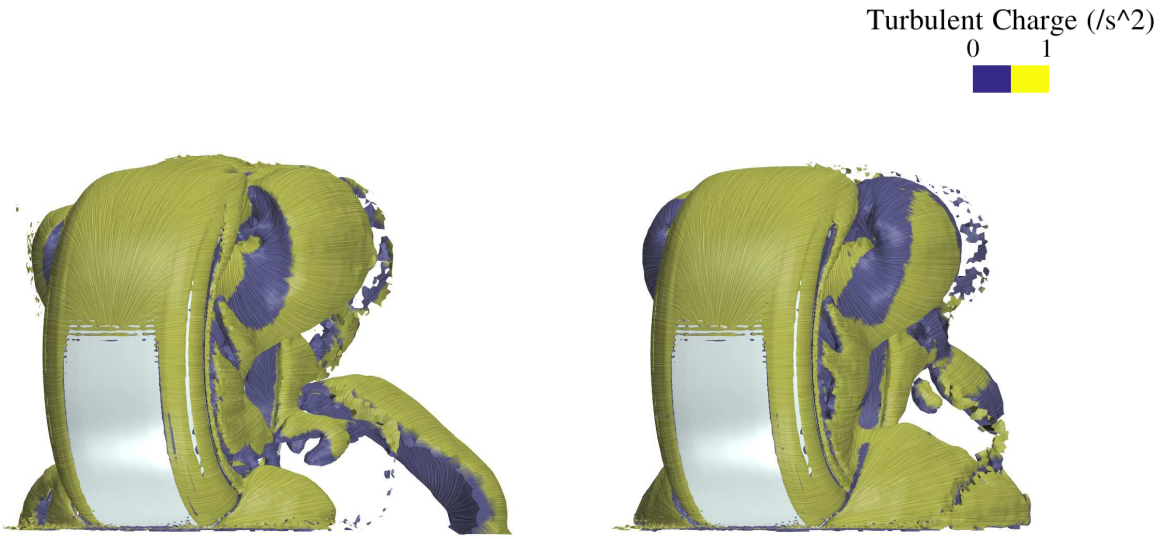

(a) RANS. **(b)** Time-averaged URANS.

Figure 4.30: Front view of isosurface of Q criterion (4000 s^{-2}) with velocity line integral convolution vectors and turbulent charge contour of the deformed wheel from RANS and time-averaged URANS simulation. Jetting phenomena is better captured by URANS while both methods overpredict upper vortex pair.

Near wake can be studied in figure 4.31. Flow behaviour analysed from the velocity profile

in figure 4.29 is confirmed. The wake is extended downstream maintaining the longitudinal axis in steady case, with a clearly defined recirculation after early separation. When URANS is implemented, the flow is highly accelerated over the wheel and presents a downwards direction when separating. Hence, less turbulent wake is found after the wheel. This behaviour plus pressure difference in the upper and lower part lead to the great lift value obtained.

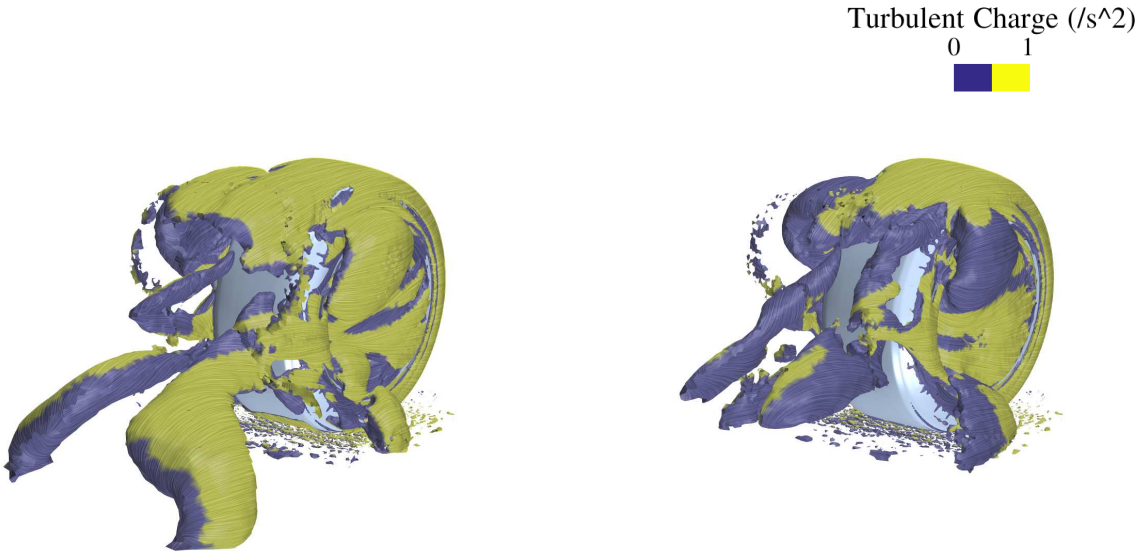

(a) RANS. **(b)** Time-averaged URANS.

Figure 4.31: Rear view of isosurface of Q criterion (4000 s^{-2}) with velocity line integral convolution vectors and turbulent charge contour of the deformed wheel from RANS and time-averaged URANS simulation. Difference in wake direction is observed: longitudinal with RANS and downwards directed with URANS.

Chapter 5

Conclusions and Future work

A computational study of an isolated rotating wheel was performed with both steady and unsteady Reynolds Averaged Navier-Stokes solver in STAR-CCM+. Contact modelling and rotating motion was overcome with an innovative Zero Gap overset approach. In parallel, tyre deformation under vertical load and inflation pressure was solved for linear elastic and multilayer hyperelastic material in ABAQUS. Eventually, fluid dynamics and structural deformation were merged and CFD simulations were reproduced over obtained deformed geometry.

One of the most challenging aspects faced during the thesis was mesh generation around the wheel. A great resolution is required for discretising the wheel-ground contact while uniform radial distribution is a must in order to maintain a similar cell size in the overlapping interface when rotating motion is activated. Therefore, wake and contact refinement was needed to be performed cautiously as total number of cells was extremely sensitive. Obtained mesh has finally shown good quality elements, consistent parametrisation in order to be replicated and refined and a satisfying coupling with Zero Gap overset approach. Polyhedral elements showed high performance and enabled layer manipulation near the contact thanks to its adaptive behaviour. Zero Gap is a powerful tool that has shown promising capabilities that could lead to a great progress in wheel contact modelling and be extrapolated to similar cases in different fields. Nevertheless, this tool is not designed for accurately solve the flow around sharp intersections and further development would be needed to implement such complex cases more robustly and closer to the contact.

Data averaging for transient moving domain was successfully overcome with a two-way volume mapping procedure that permitted conserving flow variables in a fixed reference frame to be correctly averaged. Results has shown a smooth transition between different domains. Expected limitations are found with streamlines as the variables are computed separately and is not possible to obtain a uniform solution. A unique mean variable should be obtained for the whole domain to solve mentioned problem.

Initial expectations about finite element model have been exceeded, bearing in mind it was a secondary objective. After it was found that STAR-CCM+ was unable to model this contact type, achieving a correct contact modelling with ABAQUS was a great success. Tyre deformation and contact modelling is a complex field and challenging problem for FEA, hence the quality of obtained results was quite satisfying for the scope of the study. In addition, a preliminary strategy for rotating wheel deformation was developed for further FSI study.

Steady RANS simulations and comparison with Fackrell's experimental data proved the validation of the case while URANS solution showed a better agreement with expected flow features. Drag coefficient was accurately predicted but remarkable discrepancies were found with lift coefficient. After studying pressure distribution in the wheel central plane, two areas were identified as the source of mention uncertainty. First, a suction peak was observed right after the contact that was not seen in experimental data. However, it has been found in several numerical and experimental studies the existence of such peak and even Fackrell was expecting this feature but was unable to capture it. Second, separation point on the top wheel was capture 10^{o} downstream the one predicted by Fackrell while linked suction peak upstream was also overpredicted. This aspect is not as clear in literature and no solid conclusion can be stated as many possible sources were found (turbulence model, incoming flow conditions, contact effect). Despite that, flow features and wake prediction has shown a good agreement with related literature, with a great jetting phenomena, vortex interaction and wake expansion prediction. Unexpected transversal vortex was predicted after the contact, located in an area of restricted visual accessibility for experimental data. It is concluded that innovative rotating boundary conditions and contact modelling approach applied are provoking a greater suction and vorticity in that area and this vortex is generated with a realistic physical behaviour.

Both linear elastic and hyperelastic material models have shown a correct deformation and contact adaptivity. However, when comparing both models and analysing the whole wheel response, expected limitations from linear elasticity and uniform material came out. Hyperelastic model performed more accurately with a more realistic loads distribution and overall tyre deformation. Therefore, hyperelastic multi-layer material model was chosen for further CFD simulations although a computational budget limitation for future dynamic simulations was identified.

Finally, deformed geometry obtained from ABAQUS was exported to STAR-CCM+ and adapted to previous CFD configuration. Surface was needed to be cleaned to fix gaps generated after importing procedure. Main objective of this simulation is to set a valid case for further FSI inisialitation. The same overset rotating boundary condition was unable to be implemented as the wheel deformation cannot be updated, hence not a consistent comparison could be carried as too many variables were taking into account and the source of discrepancies in the solution was difficult to be analysed. Still some conclusions can be drawn after effects experienced both

in steady and unsteady state. Higher lift and weaker and sooner suction point before the contact patch was predicted due to tyre surface variation. Wider jetting phenomena has also been observed as expected based on related studies. On the lower rear part, a recirculation bubble was also found for both steady and unsteady solutions. It is concluded that tyre deformation has an impact on flow physics in the lower wheel region and a higher lift in agreement with experimental data for solid wheel is predicted.

STAR-CCM+ has shown great possibilities for CFD simulations with complex overset configurations and a good contact approach. It is also a user friendly environment where configurations can be easily copied and modified between different cases. Plus, it is a great advantage being able to modify the geometry, mesh and visualise the solution within the same software. Unfortunately, several software limitations and instabilities were found (still reasonable due to the case complexity). The lack of an averaging algorithm fore moving reference frames is a drawback for overset simulations as it is an essential tool for transient simulations. Excessive memory usage, parallel allocation and rendering problems have provoked numerous problems and been responsible for many crashed simulations that needed to be solved varying the number of processors and averaging procedures. It has been a great problem for exporting time-dependent data and post-processing demanding cases.

Future work After the work performed in current thesis, a great improvement in modelling rotating wheels in contact with the ground is achieved and several future possibilities are proposed to enhance and push forward the limits of this model.

- An alternative mesh software could be used to improve the grid near the contact and have more control to adjust the mesh manually at that area, as grid generation in STAR-CCM+ is fully parametric. No inflation layer was achieved to be created on the ground and it could be having some impact on the solution. Hence, mesh generation process could still be improved and the effect in the solution be checked.
- Due to changes in the model and the lack of information from previous year work, no comparison has been made with different turbulence model and boundary conditions. It would be interesting to test different cases and specially study the influence at the prediction of flow separation point.
- The scope of the thesis has been focused on the flow behaviour over the tyre but not special attention has been paid to the rim. Further analysis could be performed looking for some features that may have been omitted in present work.
- A more efficient FE model can be achieved as it would be desired to have the best tyre deformation possible with the lowest computational cost as it would be updated every time step and has a great impact. The mesh refinement strategy can be clearly improved

to reduced the number of cells noticeably. Moreover, an hybrid elastic-hyperelastic model is proposed, trying to reproduce a realistic tyre deformation with a great difference in computational time. Furthemore, having access to experimental data from an homologous tyre would increase the fidelity of the study.

Apart from all previous minor issues, this work is clear focused on reaching a dynamic coupled FSI simulation between ABAQUS and STAR-CCM+. It was an ambitious objective that has not been able to be accomplished, although a great basis and background is led for future work. Co-simulation feature offers a unique opportunity to connect both powerful solvers and obtain a demanding simulation with a minimised coupling time. Not many works have been found in literature so it is still a promising feature that needs to be thoroughly verified and tested. Main problems expected are related to a prohibitive computational budget and morphing mesh update at contact area between ABAQUS and STAR-CCM+ nodes.

References

[1] Alexander Wäschle. The Influence of Rotating Wheels on Vehicle Aerodynamics - Numerical and Experimental Investigations. *SAE International*, (2007-01-0107), 2007.

[2] J E Fackrell. *The aerodynamics of an isolated wheel rotating in contact with the ground*. University of London, 1974.

[3] A J Sprot, D B Sims-Williams, and R G Dominy. The aerodynamic characteristics of a fully deformable Formula One wind tunnel tyre. *SAE International journal of passenger cars. Mechanical systems.*, 5(2):1026–1041, 2012.

[4] Dassault Systemes. Abaqus User's Manual, 2017.

[5] Xiaoguang Yang. Finite element analysis and experimental investigation of tyre characteristics for developing strain-based intelligent tyre system. 2011.

[6] Lee Axon, Kevin Garry, and Jeff Howell. The Influence of Ground Condition on the Flow Around a Wheel Located Within a Wheelhouse Cavity. In *International Congress & Exposition*. SAE International, mar 1999.

[7] Sachin Desai, C.-M.B. Lo, and Albert George. A Computational Study of Idealized Bluff Bodies, Wheels, and Vortex Structures in Ground Effect. *SAE Technical Papers*, 2008.

[8] A P. Mears and Robert Dominy. Racing Car Wheel Aerodynamics – Comparisons between Experimental and CFD Derived Flow-Field Data, 2004.

[9] Sammy Diasinos, Tracie J Barber, and Graham Doig. The effects of simplifications on isolated wheel aerodynamics. *Journal of Wind Engineering and Industrial Aerodynamics*, 146:90–101, 2015.

[10] Andrew D'Hooge, Robert B. Palin, S Johnson, Vincent Johnston, Bradley Duncan, and Joaquin Ivan Gargoloff. The Aerodynamic Development of the Tesla Model S - Part 2: Wheel Design Optimization. 2012.

[11] James McManus and Xin Zhang. A Computational Study of the Flow Around an Isolated Wheel in Contact With the Ground. *Journal of Fluids Engineering-transactions of The Asme - J FLUID ENG*, 128, 2006.

[12] Robin David Knowles. *Monoposto racecar wheel aerodynamics: investigation of Near-wake structure and support-sting interference*. PhD thesis, Cranfield University, 2005.

[13] A J Saddington, R D Knowles, and K Knowles. Laser Doppler anemometry measurements in the near-wake of an isolated Formula One wheel. *Experiments in Fluids*, 42(5), mar 2007.

[14] Richard Wood. Reynolds Number Impact on Commercial Vehicle Aerodynamics and Performance. *SAE International Journal of Commercial Vehicles*, 8:590–667, 2015.

[15] P Leśniewicz, M Kulak, and M Karczewski. Vehicle wheel drag coefficient in relation to travelling velocity - CFD analysis. *Journal of Physics: Conference Series*, 760:012014, oct 2016.

[16] Mark E Gleason, Bradley Duncan, Joel Walter, Arturo Guzman, and Young-Chang Cho. Comparison of Computational Simulation of Automotive Spinning Wheel Flow Field with Full Width Moving Belt Wind Tunnel Results. *SAE International Journal of Passenger Cars - Mechanical Systems*, 8(1):275–293, 2015.

[17] B. Schnepf, G. Tesch, and T. Indinger. Investigations on the Flow Around Wheels using Different Road Simulation Tools. *FKFS - 9th Aerodynamic Conference*, 2013.

[18] A. J. Sprot. *Open-Wheel Aerodynamics: Effects of Tyre Deformation and Internal Flow*. PhD thesis, Durham University, 2013.

[19] Alexander Wäschle, Stephane Cyr, Timo Kuthada, and Jochen Wiedemann. Flow around an Isolated Wheel - Experimental and Numerical Comparison of Two CFD Codes. In *SAE 2004 World Congress & Exhibition*. SAE International, mar 2004.

[20] John Axerio, Gianluca Iaccarino, Emin Issakhanian, Chris Elkins, and John Eaton. Computational and experimental investigation of the flow structure and vortex dynamics in the wake of a Formula 1 tire. *SAE Technical Paper 2009-01-0775*, jan 2009.

[21] G. Wickern, K. Zwicker, and M. Pfadenhauer. Rotating Wheels - Their Impact on Wind Tunnel Test Techniques and on Vehicle Drag Results. *SAE TRANSACTIONS*, 106(6):17, 1997.

[22] Per Elofsson and Mark Bannister. Drag Reduction Mechanisms Due to Moving Ground and Wheel Rotation in Passenger Cars. 2002.

[23] A. R. Purvis. *The Wake Behind a Deformable Racing Tyre*. Msc thesis, Cranfield University, 2003.

[24] Carolina Olmedo Egea. *Wheel Rim Tyre CFD Modelling*. Msc thesis, Cranfield University, 2017.

[25] Massimo Guiggiani. *Mechanics of the Wheel with Tire*, pages 7–45. Springer Netherlands, Dordrecht, 2014.

[26] W.F. Milliken and D.L. Milliken. *Race Car Vehicle Dynamics*. SAE International, 1995.

[27] T D. Gillespie. *Fundamentals of vehicle dynamics*. Warrendale: Society of Automotive Engineers, Inc., 2000.

[28] M Abe and W Manning. Chapter 2 - Tire Mechanics. In M Abe and W Manning, editors, *Vehicle Handling Dynamics*, pages 5–46. Butterworth-Heinemann, Oxford, 2009.

[29] CD-Adapco. Star-CCM+ 12.02 Theory Guide, 2017.

[30] Sofie Koitrand and Sven Rehnberg. A Computational Investigation of Wheel and Underbody Flow Interaction. Master's thesis, 2013.

[31] P.R.K. Dassanayake, D. Ramachandran, L. Salati, T.J. Barber, and G.C. Doig. Unsteady computational simulation of the flow structure of an isolated wheel in contact with the ground. School of Mechanical and Manufacturing Engineering, University of New South Wales; Department of Mechanics, Politecnico di Milano.

[32] J.-E. Lombard, H Xu, D Moxey, and S Sherwin. Rotating Wheel Wake. In *APS Division of Fluid Dynamics Meeting Abstracts*, page L3.006, 2016.

[33] Siniša Krajnović. Exploration and Improvement of Road Vehicle Aerodynamics using LES. *SAE Technical Papers*, 2011.

[34] Siniša Krajnović, Sasan Sarmast, and B Basara. LES of the Flow Around a Generic Wheel in a Wheelhouse. 1:2681–2692, 2010.

[35] Satheesh Kandasamy, Bradley Duncan, Holger Gau, Fabien Maroy, Alain Belanger, Norbert Gruen, and Sebastian Schäufele. Aerodynamic Performance Assessment of BMW Validation Models using Computational Fluid Dynamics. In *SAE 2012 World Congress & Exhibition*. SAE International, 2012.

[36] Emmanuel Olanrewaju Bolarinwa. *Investigation of the Dynamic Characteristics of Radial Tyre Using the Finite Element Method*. PhD thesis, Department of Manufacturing and Mechanical Engineering, School of Engineering, University of Birmingham, 2004.

[37] K T Danielson, A K Noor, and J S Green. Computational strategies for tire modeling and analysis. *Computers & Structures*, 61(4):673–693, 1996.

[38] SIMULIA. An Integrated Approach for Transient Rolling of Tires, 2007.

[39] Yeong-Jyh Lin and Sheng-Jye Hwang. Temperature prediction of rolling tires by computer simulation. *Mathematics and Computers in Simulation*, 67(3):235–249, 2004.

[40] Prasenjit Ghosh, A Saha, P C Bohara, and R Mukhopadhyay. Material property characterization for finite element analysis of tires. *Rubber World*, 233:22–26+31, 2006.

[41] A M Burke. *Finite Element Simulation and Experimental Analysis of Stationary and Rotating Tyre Behaviour*. University of Birmingham, 1998.

[42] Athanasia Nianioura-Karamousalidou. *Wheel Rim Tyre CFD Modelling*. Msc thesis, Cranfield University, 2017.

[43] P. K. Kundu and I. R. Cohen. *Fluid Mechanics*. Academic Press, New York, second edi edition, 2002.

[44] Glenn Research Center. Mach Number Role in Compressible Flows, 2015.

[45] J. J. Keogh, S. Diasinos, and G.C. Doig. Flow compressibility effects around an open-wheel racing car. 2015.

[46] G. Stokes. On the Effect of the Internal Friction of Fluids on the Motion of Pendulums. *Transactions of the Cambridge Philosophical Society*, 9:8, 1851.

[47] Inc. FLUENT. Modeling Turbulent Flows. *ANSYS.Inc.*, pages 6–2, 6–49, 2006.

[48] J. Boussinesq. *Essai sur la théorie des eaux courantes*. Imprimerie Nationale, 1877.

[49] W. P. Jones and B. E. Launder. The prediction of laminarization with a two-equation model of turbulence. *International Journal of Heat and Mass Transfer*, 15(2):301–314, 1972.

[50] T. Shih, W. Liou, A. Shabbir, Z. Yang, and J. Zhu. A new k-e eddy viscosity model for high reynolds number turbulent flows. *Computers & Fluids*, 24(3):227–238, 1995.

[51] P. R. Spalart and C. L. Rumsey. Effective Inflow Conditions for Turbulence Models in Aerodynamic Calculations. *AIAA Journal*, 45(10):2544–2553, 2007.

[52] T. Jongen. *Simulation and Modeling of Turbulent Incompressible Flows*. Ph.d. thesis, Lausanne EPFL, 1998.

[53] D. C. Drucker. On the postulate of stability of material in the mechanics of continua. *Mekhanica. Period. Sbornik Perevodov Invstr. Statei*, 3:115–128, 1964.

[54] M. Mooney. A Theory of Large Elastic Deformation. *Journal of Applied Physics*, 11(9):582–592, sep 1940.

[55] R. S. Rivlin. Large elastic deformations of isotropic materials IV. further developments of the general theory. *Philosophical Transactions of the Royal Society of London A: Mathematical, Physical and Engineering Sciences*, 241(835):379–397, 1948.

[56] R W Ogden. Non-Linear Elastic Deformations. *ZAMM - Journal of Applied Mathematics and Mechanics / Zeitschrift für Angewandte Mathematik und Mechanik*, 65(9):404.

[57] R W Ogden. Large deformation isotropic elasticity {\textendash} on the correlation of theory and experiment for incompressible rubberlike solids. *Proceedings of the Royal Society of London A: Mathematical, Physical and Engineering Sciences*, 326(1567):565–584, 1972.

[58] O H Yeoh. Some Forms of the Strain Energy Function for Rubber. *Rubber Chemistry and Technology*, 66(5):754–771, 1993.

[59] Siemens PLM Software. STAR-CCM+ Overset Mesh.

[60] Jacques Heyder-Bruckner. *The aerodynamics of an inverted wing and a rotating wheel in ground effect*. Phd thesis, University of Southampton, 2011.

[61] Christine Obbink-Huizer. How Abaqus treats initial overclosures of contacting surfaces, 2017.

[62] Hao Wang, Imad L Al-Qadi, and Ilinca Stanciulescu. Simulation of tyre–pavement interaction for predicting contact stresses at static and various rolling conditions. *International Journal of Pavement Engineering*, 13(4):310–321, 2012.

[63] Nikola Korunovic, Milos Stojkovic, and Miroslav Trajanovic. FEA of tyres subjected to static loading. *Journal of the Serbian Society for Computational Mechanics*, 2007.

[64] Mengyan Zang and Yujian Chen. Experiments and finite element simulations of a tyre blow-out process. *Proceedings of the Institution of Mechanical Engineers Part D Journal of Automobile Engineering*, 2014.

[65] Wei Wang, Shan Yan, and Zhao Shugao. Experimental verification and finite element modeling of radial truck tire under static loading. *Journal of Reinforced Plastics and Composites*, 2013.

[66] M. Hinson. *Measurement of the lift produced by an isolated, rotating Formula One wheel using a new pressure measurement system*. Msc thesis, Cranfield University, 1999.